

Electronic Thesis and Dissertation Repository

---

11-21-2017 3:00 PM

## A 3D US Guidance System for Permanent Breast Seed Implantation: Development and Validation

Justin Michael  
*The University of Western Ontario*

Supervisor  
Fenster, Aaron  
*The University of Western Ontario*

Graduate Program in Biomedical Engineering  
A thesis submitted in partial fulfillment of the requirements for the degree in Master of  
Engineering Science  
© Justin Michael 2017

Follow this and additional works at: <https://ir.lib.uwo.ca/etd>



Part of the [Biomedical Devices and Instrumentation Commons](#)

---

### Recommended Citation

Michael, Justin, "A 3D US Guidance System for Permanent Breast Seed Implantation: Development and Validation" (2017). *Electronic Thesis and Dissertation Repository*. 5052.  
<https://ir.lib.uwo.ca/etd/5052>

This Dissertation/Thesis is brought to you for free and open access by Scholarship@Western. It has been accepted for inclusion in Electronic Thesis and Dissertation Repository by an authorized administrator of Scholarship@Western. For more information, please contact [wlsadmin@uwo.ca](mailto:wlsadmin@uwo.ca).

# Abstract

Permanent breast seed implantation (PBSI) is a promising breast radiotherapy technique that suffers from operator dependence. We propose and have developed an intraoperative 3D ultrasound (US) guidance system for PBSI.

A tracking arm mounted to a 3D US scanner registers a needle template to the image. Images were validated for linear and volumetric accuracy, and image quality in a volunteer. The tracking arm was calibrated, and the 3D image registered to the scanner. Tracked and imaged needle positions were compared to assess accuracy and a patient-specific phantom procedure guided with the system.

Median/mean linear and volumetric error was  $\pm 1.1\%$  and  $\pm 4.1\%$ , respectively, with clinically suitable volunteer scans. Mean tracking arm error was 0.43 mm and 3D US target registration error  $\leq 0.87$  mm. Mean needle tip/trajectory error was 2.46 mm/1.55°. Modelled mean phantom procedure seed displacement was 2.50 mm. To our knowledge, this is the first reported PBSI phantom procedure with intraoperative 3D image guidance.

Keywords: Ultrasound, 3D Ultrasound, Image Guidance, Brachytherapy, Radiation Therapy, Breast Cancer

## Co-Authorship Statement

A version of chapter 2 has been submitted for publication in Medical Physics as an article titled, “Development of a 3D Ultrasound Guidance System for Permanent Breast Seed Implantation” by Justin Michael, Daniel Morton, Deidre Batchelar, Michelle Hiltz, Juanita Crook and Aaron Fenster. I designed and performed all experiments, and analyzed all results, and worked with hardware and software developers in the design of the system. Daniel Morton provided assistance in collecting the data for volumetric validation of the 3D US scanner. Deidre Batchelar, Michelle Hiltz, and Juanita Crook were involved in the initial conception of a 3D US guidance system for PBSI and were instrumental in translating clinical requirements into technical specifications and features. The guidance system hardware was designed and constructed by Kevin Barker, Jacques Montreuil and Christopher Blake and the software for operation of the guidance system written by Lori Gardi.

Appendix A is a letter-to-the-editor published online in Clinical Oncology on March 31st, 2017 entitled “Reply to: Who Should Bear the Cost of Convenience? A Cost-effectiveness Analysis Comparing External Beam and Brachytherapy Radiotherapy Techniques for Early Stage Breast Cancer.” The manuscript was co-authored by Justin Michael, Juanita Crook, Daniel Morton, Deidre Batchelar, Michelle Hiltz and Aaron Fenster. I was responsible for conceiving of and drafting the first text of the letter, for conducting the analysis contained within and for submitting the letter to the journal, all under the supervision of Dr Aaron Fenster. Juanita Crook was responsible for obtaining data regarding travel distance amongst patients at the Centre for the Southern Interior, in Kelowna, Canada. Juanita Crook, Daniel Morton, Deidre Batchelar and Michelle Hiltz each provided editorial input on the final draft.

## Acknowledgements

I would like to thank my supervisor Dr. Aaron Fenster, for his unrelenting support and for giving me the opportunity to grow while wrestling with a challenging and meaningful research project. That opportunity would not have been what it was if it were not for the positive and supporting environment created by all of the members of the Fenster lab, past and present, including Lori Gardi, Kevin Barker, David Tessier, Jacques Montreuil, Igor Gyasckov, Chandima Edirisinghe, Jeff Bax, Jessica Kishimoto, and Tom Hrinivich. Particular thanks goes to Jessica Rodgers and Derek Gillies who's constant willingness to act as advisors, sounding-boards, and friends has been indispensable in guiding me through my time in graduate school.

Thanks is also due to the many contributors to my research work outside of the Fenster lab, including my advisory committee, Drs. Kathleen Surry and Aaron Ward, for their exceptional tutelage and guidance. Also to our collaborators at the Sindi Ahluwalia Hawkins Centre for the Southern Interior in Kelowna, British Columbia, Juanita Crook, Deidre Batchelar, Michelle Hilts and Daniel Morton, for their guidance and patience (even when I flew across the country only to arrive in Kelowna with a broken scanner).

I would also like to acknowledge the sources of funding who have made this opportunity possible, including the Ontario Institute for Cancer Research and the Ontario Women's Health Scholar Awards. Their support allowed me to spend my time in graduate school focused on my research rather than my finances, for which I am exceedingly grateful.

Most importantly, I want to thank my friends, family and loved ones. My friends from undergraduate school and high school, too numerous to list, my parents, Vicki Hodgkinson and Kevin Michael, and my amazing partner Katerina Rnic. The importance of their ongoing love and support cannot be overstated.

# Contents

Abstract	i
Co-Authorship Statement	ii
Acknowledgements	iii
List of Figures	vii
List of Tables	x
List of Appendices	xi
List of Abbreviations	xii
1 Introduction	1
1.1 Early Stage Breast Cancer and its Treatment . . . . .	1
1.1.1 Breast Cancer and its Progression . . . . .	1
1.1.2 Treatment of Early Stage Breast Cancer . . . . .	3
1.1.3 Breast Radiotherapy . . . . .	5
1.1.4 Radiobiology . . . . .	5
1.2 Accelerated Partial Breast Irradiation . . . . .	8
1.2.1 Rationale and Key Concepts . . . . .	8
1.2.2 Eligibility and Clinical Evidence . . . . .	10
1.2.3 Interstitial and Intracavitary Breast Brachytherapy . . . . .	11
1.2.4 External Beam APBI . . . . .	13
1.2.5 Intraoperative Radiotherapy . . . . .	13
1.2.6 Emerging Techniques in APBI . . . . .	14
1.2.7 Permanent Breast Seed Implantation . . . . .	15
1.3 Challenges of PBSI . . . . .	18
1.3.1 Operator Dependence and Previous Work . . . . .	18

1.3.2	Limitations of Intraoperative Guidance . . . . .	19
1.3.3	Imaging Dissimilarities Between Planning and Guidance . . . . .	20
1.4	Thesis Objective . . . . .	22
1.5	Relevant Physics: Brachytherapy and 3D Ultrasound . . . . .	22
1.5.1	Brachytherapy Physics . . . . .	22
1.5.2	Three-Dimensional Ultrasound Physics . . . . .	23
1.6	Ultrasound Guidance of Brachytherapy Procedures . . . . .	25
1.6.1	Three-Dimensional US Guidance of Prostate, HDR Breast Brachytherapy . . . . .	25
1.6.2	Other Methods of Needle and Needle Template Tracking and Guidance . . . . .	25
	References . . . . .	26
2	System Development and Validation . . . . .	38
2.1	Introduction . . . . .	38
2.2	Materials and Methods . . . . .	40
2.2.1	System Design . . . . .	40
2.2.1.1	Three-Dimensional US Scanner . . . . .	40
2.2.1.2	Encoded Arm and Modified Needle Template . . . . .	41
2.2.2	System Calibration and Validation . . . . .	43
2.2.2.1	Three-Dimensional Image Reconstruction . . . . .	43
2.2.2.2	Encoder Mapping . . . . .	45
2.2.2.3	Tracking Arm Point Accuracy . . . . .	47
2.2.2.4	Image to Scanner Registration . . . . .	48
2.2.2.5	Template Localization Accuracy . . . . .	49
2.2.2.6	Needle Insertion Accuracy . . . . .	49
2.2.2.7	Phantom Procedure . . . . .	51
2.2.2.8	Statistical Methods . . . . .	53
2.3	Results . . . . .	53
2.3.1	Three-Dimensional Image Reconstruction . . . . .	53
2.3.2	Encoder Mapping . . . . .	55
2.3.3	Tracking Arm Point Accuracy . . . . .	55
2.3.4	Image to Scanner Registration . . . . .	58
2.3.5	Template Localization Accuracy . . . . .	59
2.3.6	Needle Insertion Accuracy . . . . .	59

2.3.7	Phantom Procedure . . . . .	62
2.4	Discussion . . . . .	62
2.4.1	Three-Dimensional Image Reconstruction . . . . .	62
2.4.2	Encoder Mapping . . . . .	63
2.4.3	Tracking Arm Point Accuracy . . . . .	63
2.4.4	Image to Scanner Registration . . . . .	64
2.4.5	Template Localization Accuracy . . . . .	64
2.4.6	Needle Insertion Accuracy . . . . .	64
2.4.7	Phantom Procedure . . . . .	65
2.5	Conclusions . . . . .	66
References		66
3	Conclusions and Future Work	72
3.1	Overview and Research Questions . . . . .	72
3.2	Summary and Conclusions . . . . .	72
3.3	Limitations . . . . .	75
3.4	Future Work . . . . .	76
3.4.1	Device Refinements . . . . .	76
3.4.1.1	Hardware Refinements . . . . .	76
3.4.1.2	Software Refinements . . . . .	78
3.4.2	Clinical Translation . . . . .	79
References		80
Appendices		84
A	Letter to the Editor	84
B	94km Map - Methods	87
C	Ethics Approval	91
D	Permission for Reproduction of Scientific Articles	92
Curriculum Vitae		93

# List of Figures

1.1	Summary of the stages of cancer progression. Adapted from Canadian Partnership Against Cancer, 2015 [3] . . . . .	2
1.2	Illustration of the geographic areas of Canada within 93.6 km travel distance of a Canadian Cancer Centre. For Canadian patients living outside of the areas highlighted in red (estimated 15% of the Canadian population), our analysis revealed that PBSI is less costly than standard radiotherapy. Available online as an interactive map: <a href="http://bit.ly/94kmMap">http://bit.ly/94kmMap</a>	17
2.1	Screenshot from guidance software showing registered needle template relative to central slice of 3D US image and segmented seroma phantom (green). Teal cylinder indicates projection of selected needle template position. . . . .	42
2.2	a) Image of guidance system positioned above commercial breast phantom. b) Illustration of coordinate systems (CSs) used in validation ('Image' CS not shown). . . . .	43
2.3	Summary of information pipeline in the guidance system and the list of experiments used in validation. Experiments 1–6 validate a step in the process indicated by dashed arrows. Experiment 7 evaluates the process as a whole. CS = coordinate system. . . . .	44
2.4	Encoder mapping set-up. a) Surface plate, gauge blocks and height stand in use during calibration of the most distal joint. b) Partially disassembled template tracking arm with tooling balls. The most distal segment (left) has been removed and a tooling ball added in its place. A machined extension and tooling ball (right) has been added. . . . .	46
2.5	Guidance system positioned in tracking arm calibration jig. Jig contained 45 fiducial divots arranged in a $9 \times 5$ grid pattern separated by 2 cm in each direction. Mounting position of scanner adjusted forward/back and left/right in 3 cm increments, so that 180 ( $45 \times 4$ ) known positions are available for calibration/validation. . . . .	47



2.6	Experimental set-up for needle insertion through a tracked template. A collar affixed to the needle allows for a known insertion depth into a bath of isopropyl alcohol and water. Comparison of needle position in tracking and imaging quantifies tracking accuracy. Tracking arm has been bagged to prevent damage if immersed. . . . .	50
2.7	Screenshot showing visual overlay of planned needle position (purple) and projected needle trajectory (cyan) on live 2D US image for guidance during needle insertion. Inserted needle is visible in US image beneath purple overlay. . . . .	52
2.8	Results of linear measurement validation using a 3D grid phantom immersed in 7.25 % by volume isopropyl alcohol solution. Columns and error bars show medians and 95 % confidence intervals, respectively. N=40 per direction, per depth setting. . . . .	54
2.9	Multi-planar views of a 3D US image captured from a healthy volunteer using developed system. Left: View showing representative slices of image along orthogonal planes. Arrows and labels indicate principal axes. Right: View illustrating geometry of reconstructed scans. Field of view visible in axial-elevational plane is constant across lateral axis. . . . .	55
2.10	Integral error of each encoder in the tracking arm as a function of absolute position when calibrated. Each encoder was calibrated using multiple mounting positions in order to span the full range of motion. Dashed black line indicates the estimated integral encoder error after smoothing. All plots show integral error over 360° range (0–4095 encoder counts). . .	56
2.11	Normalized histogram of target registration error (TRE) observed during tracking arm validation plotted with respect to probability (N=240). Dashed black line indicates mean TRE (0.43 mm). . . . .	57
2.12	95 % prediction ellipsoid of arm validation error plotted with respect to the arm coordinate system (units: mm). Black dots indicate individual point measurement errors and red lines indicate boundaries of 95 % confidence ellipsoids. Gray dots and adjacent ellipses indicate projections of the above onto canonical planes. See Figure 2.2b for coordinate system description.	58

2.13	Ninety-five percent prediction ellipsoid of needle placement error plotted with respect to the image coordinate system. Black dots indicate individual point measurement errors and red lines indicate boundaries of 95% confidence ellipsoids. Gray dots and adjacent red ellipsoids indicate projections of the above onto canonical planes. See Figure 2.2b for coordinate system description. . . . .	61
2.14	Post-operative images of phantom procedure. a) Visualization of planned and observed needle positions overlaid on post-op micro-CT. Planned seed-bearing (fiducial) needles shown in blue (cyan) with observed needles shown in red (pink). Pre-op seroma following registration to post-op micro-CT shown in green. b) Reconstucted plane of 3D US with seroma and all 15 needles visible. . . . .	62

# List of Tables

1.1	Simplified table of stage by TNM classification. Adapted from American Joint Committee on Cancer, 2009 [5]. Note that stages appear to overlap in individual categories (T/N/M) only because stage is dependent on all categories (e.g. T2N1M0 is stage 1 while T2N2M0 is stage 2). Tis = tumour - carcinoma in situ; N1mi = N1 micrometastasis) . . . . .	2
1.2	Summary of completed and ongoing phase III prospective randomized clinical trials comparing APBI to WBI. Adapted from Tann et al. 2016 [44] with the addition of recently published results from Coles et al. 2017 [48] on the IMPORT-LOW trial. . . . .	12
2.1	Results of volumetric validation comparing segmented volume in 3D US to water displacement volume. 95% confidence intervals calculated using a Welch's t-test. . . . .	54
2.2	Confidence intervals on the mean error in each axis following tracking arm point accuracy validation. Error evaluated in the arm coordinate system (Figure 2.2b). . . . .	57
2.3	Target and fiducial registration error (TRE and FRE) of registering the scanner and image coordinate systems using a phantom with 12 string intersections (6 fiducials, 6 targets). . . . .	59
2.4	Mean (SD) of components of template localization errors. Rotations and translations expressed with respect to the scanner coordinate system (Figure 2.2b). Positive angles indicate clock-wise rotation about an axis when viewed from the origin. . . . .	59
2.5	Magnitude of needle tip and trajectory error when comparing expected needle position from tracking and insertion depth to observed needle position in 3D US. . . . .	60
2.6	Confidence intervals on the mean error in each axis following needle insertion accuracy validation. Error evaluated in the imaging coordinate system (Figure 2.2b) and averaged across all needle insertion depths. . .	61

# List of Appendices

Appendix A Letter to the Editor . . . . .	84
Appendix B 94km Map - Methods . . . . .	87
Appendix C Ethics Approval . . . . .	91
Appendix D Permission for Reproduction of Scientific Articles . . . . .	92

# List of Abbreviations

$^{125}\text{I}$	Iodine-125
$^{103}\text{Pd}$	Palladium-103
$^{192}\text{Ir}$	Iridium-192
2D	Two-Dimensional
3D	Three-Dimensional
3D-CRT	3D Conformal Radiotherapy
APBI	Accelerated Partial Breast Irradiation
API	Application Programming Interface
BCS	Breast Conserving Surgery
BCT	Breast Conserving Therapy
BED	Biologically Effective Dose
CAD	Canadian Dollars
CRA	Canada Revenue Agency
CS	Coordinate System
CSI	Centre for the Southern Interior
CT	X-ray Computed Tomography
CTV	Clinical Target Volume
DNA	Deoxyribonucleic Acid
DoF	Degree of Freedom
EBRT	External Beam Radiotherapy
EM	Electromagnetic
ER	Estrogen Receptor- $\alpha$
ESCD	Estimated Study Completion Date
FLE	Fiducial Localisation Error
FRE	Fiducial Registration Error
GADM	Database of Global Administrative Areas
GEC-ESTRO	Groupe Européen de Curiethérapie-European Society for Therapeutic Radiology and Oncology

GIS	Geographic Information System
GPS	Global Positioning System
GTV	Gross Tumour Volume
HDR	High Dose-Rate
HER2	Human Epidermal Growth Factor Receptor 2
HR	Hormone Receptor
ICB	Intracavitary Brachytherapy
ICP	Iterative Closest Point
IMRT	Intensity Modulated Radiotherapy
IORT	Intraoperative Radiotherapy
JSON	JavaScript Object Notation
KML	Keyhole Markup Language
kVp	Kilo-Voltage Peak
LDR	Low Dose-Rate
linac	Linear Particle Accelerator
LQ	Linear-Quadratic
MDR	Medium Dose-Rate
MIB	Multicatheter Interstitial Brachytherapy
ML	Multi-Lumen
MLC	Multi-Leaf Collimator
MR	Magnetic Resonance
MRI	Magnetic Resonance Imaging
NIBB	Non-Invasive Breast Brachytherapy
OAR	Organ-at-Risk
PBSI	Permanent Breast Seed Implantation
PC	Personal Computer
PgR	Progesterone Receptor
PTV	Planning Target Volume
RCT	Randomized Clinical Trial
RMSE	Root Mean Squared Error

SABR	Stereotactic Ablative Radiotherapy
SAVI	Strut Adjusted Volume Implant
SBRT	Stereotactic Body Radiation Therapy
SD	Standard Deviation
SERM	Selective Estrogen Receptor Modulator
$T_{\text{actual}}$	Actual (Ground Truth) Transform
$T_{\text{error}}$	Error Transform
TG43	American Association of Physicists in Medicine Task Group 43
$T_{\text{measured}}$	Measured Transform
TNM	Tumour-Node-Metastasis
TPX	Polymethylpentene Plastic
TRE	Target Registration Error
TRUS	Transrectal Ultrasound
US	Ultrasound
USB	Universal Serial Bus
WBI	Whole Breast Irradiation

# Chapter 1

## Introduction

### 1.1 Early Stage Breast Cancer and its Treatment

#### 1.1.1 Breast Cancer and its Progression

For Canadian women, breast cancer is the most commonly diagnosed cancer and the second highest cause of cancer related death, with an estimated 26,300 new cases and 5,000 deaths in 2017 [1]. Globally, breast cancer is the 2nd most common cancer and the 5th highest cause of cancer death, with an estimated 1.7 million cases and 522,000 deaths in 2012 [2].

Like all cancers, if left untreated breast cancer follows a progression from a localized group of abnormal cells to larger invasive tumours that spread (metastasize) to other parts of the body via the lymph nodes and circulatory system. The extent of progression is categorized by stage from 0–4, as summarized in Figure 1.1. Assessment of cancer stage acts as a strong indicator of prognosis, influencing the choice of treatment for each patient.

Cancer stages are defined using the Tumour-Node-Metastasis (TNM) system, which provides criteria to score the cancer’s progression with respect to the size of the original tumour, any spread to nearby lymph nodes, and the presence or absence of distant metastases. Each item on the TNM scale is given a numeric rating (T:0-4, N:0-3, M:0-1), sometimes with additional sub-specification (e.g. Tis for carcinoma in situ), and the aggregation of the three scores is used to define the cancer stage. A simplified version of the definition of cancer stage by TNM category is shown in Table 1.1. The term “early-stage” breast cancer generally refers to stages 0–2 [4].

While knowledge of cancer stage is useful for prognosis and treatment selection, the definition of stage is primarily anatomic, despite a growing number of non-anatomic biomarkers [6]. Of those non-anatomic biomarkers, three are routinely assessed clinically



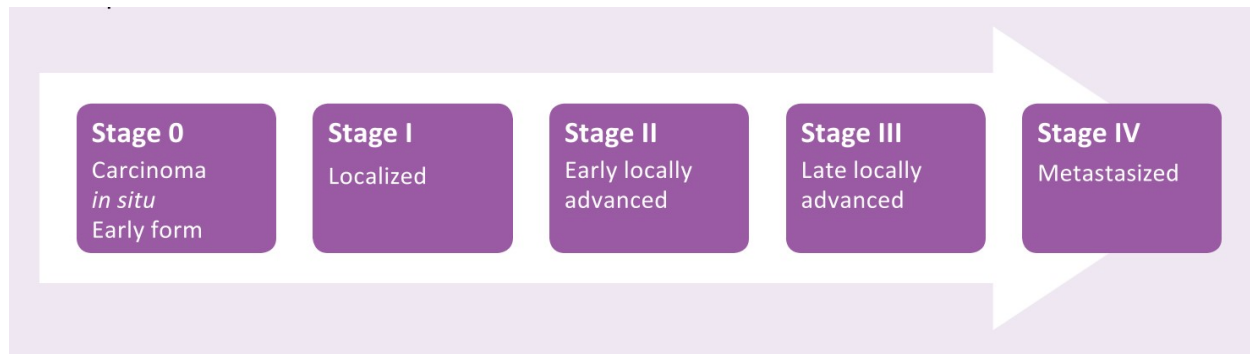


Figure 1.1: Summary of the stages of cancer progression. Adapted from Canadian Partnership Against Cancer, 2015 [3]

Table 1.1: Simplified table of stage by TNM classification. Adapted from American Joint Committee on Cancer, 2009 [5]. Note that stages appear to overlap in individual categories (T/N/M) only because stage is dependent on all categories (e.g. T2N1M0 is stage 1 while T2N2M0 is stage 2). Tis = tumour - carcinoma in situ; N1mi = N1 micrometastasis)

Stage	T	N	M
Stage 0	Tis	N0	M0
Stage I	T0-1	N0-1mi	M0
Stage II	T0-3	N0-1	M0
Stage III	T0-4	N0-2	M0
Stage IV	Any T	Any N	M1

in breast cancer: the expression of two hormone receptors, estrogen receptor- $\alpha$  (ER) and progesterone receptor (PgR), and the presence of HER2 (human epidermal growth factor receptor 2) [7]. All three of these biomarkers indicate a variable by which the cancer cells can be differentiated from healthy cells, making it possible to supplement treatment with targeted therapies. ER and PgR status, referred to as ER or PgR positive respectively, are indicative of tumour cells whose growth is dependent on estrogen, making it possible to target these cells using drugs that either disrupt the interaction of estrogen with these receptors, selective estrogen receptor modulators (SERMs) such as tamoxifen, or that suppress the production of estrogen, such as aromatase inhibitors. Approximately 75% of invasive breast cancers are ER positive and 60–70% are PgR positive [7], with hormone receptor (HR) positive tumours having a generally favorable prognosis relative to HR negative tumours [8]. The third biomarker, HER2, is a proto-oncogene (precursor to a gene that can cause cancer) that is amplified in 20–30% of invasive breast cancers [9]. HER2 positive tumours can be targeted with an antibody based treatment called trastuzumab (trade name Herceptin), which is considered an integral part of therapy for patients with HER2 positive tumours [9].

In addition to tumour specific biomarkers, genetic risk factors for breast cancer have also been identified, most notably mutations in the BRCA1 and BRCA2 genes. These genes are both involved in a key pathway for the repair of DNA damage (homologous recombination repair) and cells with mutations in these genes must rely on a secondary pathway (non-homologous end joining) that is more error-prone [10]. The reliance on an error-prone repair pathway leads to more frequent mutation and a greater risk of tumour development, with an estimated lifetime breast cancer risk of >80% [11]. Despite the exceedingly high breast cancer incidence amongst women with BRCA1/2 mutations, evidence on their value as a prognostic indicator remains unclear [12].

### 1.1.2 Treatment of Early Stage Breast Cancer

Techniques for breast cancer treatment can be summarized into three categories: surgical, systemic, and radiation therapies.

With respect to surgical therapies, one well-established treatment for early stage breast cancer is breast conserving surgery (BCS), also known as lumpectomy, in which the primary tumour is surgically removed while sparing the remainder of the breast. When followed by adjuvant whole breast irradiation (WBI), the combined treatment regimen is referred to as breast conserving therapy (BCT) and is considered the standard of care for early stage breast cancer [13]. Following the surgery, the removed tissue is analyzed histologically to provide additional information about the tumour type and to

examine the extent of normal tissue clearance around the excised tumour. The extent of normal tissue around the excised tumour, is referred to as the excision ‘margins’. ‘Positive margins’ indicate that the tumour comes to the edge of the excised volume, likely indicating that not all of the tumour was removed, making it an indication for re-excision [14]. An excised tumour may also be considered to have ‘close margins’ if the amount of normal tissue around the tumour is less than a prespecified safety margin, typically on the order of 1–5 mm [14]. While close margins may indicate further treatment, such as re-excision, consensus guidelines published in 2013 indicate that more widely clear margins do not decrease the rate of ipsilateral recurrence [14].

Breast conserving therapy was introduced as an alternative to mastectomy [15], or the surgical removal of the entire affected breast, in order to achieve a better cosmetic outcome while still addressing the disease. Although the effectiveness of BCT has been established, mastectomy is still necessary for certain patients such as those with multicentric disease (i.e. multiple tumours in the same breast), patients for whom a lumpectomy has failed to achieve negative margins, or for locally recurrent cases [16].

Systemic therapies refer to treatments that travel through the blood stream, reaching cells throughout the body. While early-stage cancers are, by definition, localized to the breast, it is generally accepted that a portion of patients with disease that is localized by clinical standards will have micro-metastases that are not presently detectable. The risk of micro-metastases motivates the exploration of systemic therapies in combination with surgical and/or radiotherapeutic treatments, even for early-stage disease [17]. Cytotoxic chemotherapy is one form of systemic therapy which uses drugs that preferentially target rapidly dividing cells, typically administered in a combination therapy of multiple drugs [18]. A review of international guidelines suggested that chemotherapy is indicated for patients with tumours  $>1$  cm or with nodal involvement [19].

In addition to the traditional chemotherapeutic forms of systemic therapy, targeted therapies for the cancer subtypes discussed in section 1.1.1 above, namely SERMS or aromatase inhibitors for ER and/or PgR positive tumours and trastuzumab for HER2 positive tumours, are typically indicated when the appropriate subtype has been identified.

Lastly, radiotherapy is an important component of breast cancer management, with the radiobiology and delivery techniques of radiotherapy discussed in more detail below. Often radiotherapy is used in conjunction with surgery, as in BCT, with the intention of killing any occult, microscopic deposits of cancerous cells that would be missed by typical resection margins [20].

### 1.1.3 Breast Radiotherapy

The delivery of breast radiotherapy may use one of two classes of techniques: external beam radiotherapy (EBRT) and brachytherapy, with EBRT currently being by far the most common. In EBRT, a linear particle accelerator (linac) is used to generate a beam of ionizing radiation that is directed towards the patient. The beam is shaped or modulated using secondary collimation such as jaws or multi-leaf collimators (MLC's) in combination with step-and-shoot or arc delivery techniques [21]. EBRT may deliver photons or electrons, depending on the device used to produce them and its configuration, with energies typically ranging from 4–20 MeV [21].

Conversely, brachytherapy uses a sealed source, such as a radioactive seed or wire, placed in or near the target, such as inside a tumour or at the surface of a superficial lesion. The prefix ‘brachy’ comes from the Greek word for ‘short’, reflecting the short distance between the source and the target. The “sealed” source of brachytherapy contrasts with the use of systemic radiotherapy, in which radioactive compounds enter the bloodstream, such as orally administered iodine-131 to treat thyroid cancer [22].

Brachytherapy may be further categorized by the rate at which dose is delivered. Low, medium, and high dose rate (LDR, MDR, and HDR, respectively) brachytherapy is defined as dose rates from 0.2–0.4 Gy/h, 2–12 Gy/h and >12 Gy/h, respectively [23]. Brachytherapy radiation may also be delivered intermittently, known as pulsed dose rate [23], although in modern practice LDR and HDR brachytherapy are most common.

While LDR brachytherapy can be delivered by manually placing sources, HDR brachytherapy is potentially dangerous to the operator and is delivered automatically and remotely using a device called an afterloader. An afterloader is an electronic device that uses motors and sensors to sequentially move a single radioactive source attached to the end of a wire through multiple catheters implanted in or placed near the target. The dose is adjusted based on where the source is moved (dwell positions) and how long it stays there (dwell times). Dwell times and positions are specified in a treatment plan determined based on target geometry determined from imaging of the area [24]. Treatment times are in the range of minutes, and are delivered in discrete ‘fractions’, similar to the EBRT approach. Energies of commonly used brachytherapy sources range from 21–1250 keV [23].

### 1.1.4 Radiobiology

Ionizing radiation disrupts cells by damaging deoxyribonucleic acid (DNA), a large molecule whose structure is characterized by its famous double-helix shape [10]. The energy deposited by ionizing radiation can damage the structure of DNA by breaking

one or both strands of the double-helix, known as single- and double-stranded breaks, respectively. Double stranded breaks are thought to be the most important DNA lesions for radiotherapy as they are principally responsible for cell killing [10]. While ionizing radiation causes damage to healthy cells, it is especially damaging to cancerous cells [25], creating a differential response that allows radiation to be used for treatment. The magnitude of the difference in response between cancerous and non-cancerous cells can be described in terms of the therapeutic ratio, also known as the therapeutic index, which is defined as the ratio of the tumour control probability to the normal-tissue complication probability for a fixed level of normal tissue damage [10].

As a result of the effect of ionizing radiation on both cancerous and healthy cells, radiotherapy is often accompanied by adverse events. These side-effects are caused by either radiation damage to the surrounding healthy tissue of the target organ or to other nearby organs, termed organs-at-risk (OARs). In the case of breast radiotherapy, OARs include the heart, lungs, skin, ribs and contralateral breast [26]. Adverse events of the skin can include erythema (redness), moist desquamation, telangiectasia, and induration [27], while other organ adverse events include cardiomyopathy and secondary cancers [28].

The biological effects of radiotherapy are characterized principally by the dose delivered to tissues measured in Gray (Gy), where 1 Gy corresponds to 1 joule of absorbed energy from ionizing radiation per kilogram of matter [29]. The dose delivered during radiotherapy is calculated using simulations based on the geometry of the target (e.g. tumour) relative to the source, and established calibration data describing the dose distribution. In the case of EBRT, the dose distribution is a function of penetration depth, and in the case of brachytherapy it is a function of distance and angle from the source. The attenuation of dose as it travels through a medium (e.g. tissue) depends on the beam characteristics, with lower energy photons attenuated more rapidly, but generally reach a maximum at or near the entry point of the beam, for EBRT, or adjacent to the source, for brachytherapy, and decay to zero with increasing depth.

In addition to the dose delivered to tissue, biological effects are also strongly influenced by the timing in which the dose is received. Radiotherapy is usually separated into a series of small treatments separated by hours or days, referred to as fractionation, to best leverage the radiobiological phenomena related to cell death. These phenomena are often summarized by the “five R’s of radiobiology”: reassortment, repopulation, reoxygenation, repair, and radiosensitivity [10, 30]. Reassortment refers to the redistribution of cells amongst the various stages of the mitotic cell cycle. Cells are more susceptible to radiation damage in some stages than others due to differences in the dominant DNA

repair mechanisms, making reassortment a mechanism of sensitizing cells that might have been radioresistant during a previous fraction. Repopulation refers to the regrowth of cell populations, healthy or cancerous, to replace cells killed by radiation therapy. Reoxygenation refers to the return of oxygen supply to tumour cells to maximize its radiosensitizing effects in catalyzing the permanent damage of DNA by free radicals. Repair refers to the ability of cells to repair sublethal damage to their DNA. Lastly, radiosensitivity refers to intrinsic differences in the radiosensitivity of different cell types. The historical rationale for fractionated therapy is that it leverages the repair and repopulation of healthy cells to minimize toxicity, while allowing reoxygenation and reassortment to radiosensitize cancerous cells [10].

The relationship between the dose of the fraction delivered and its effect on cell killing has been studied extensively, resulting in the linear-quadratic (LQ) model. In the LQ model, the effect of radiation damage on cell survival is modelled as the sum of two components, one linear with respect to dose ( $\alpha$ ), and the other quadratic ( $\beta$ ), summarized in equation 1.1:

$$S = e^{\alpha D + \beta D^2} \quad (1.1)$$

where  $S$  is the surviving fraction of cells,  $D$  is the radiation dose and  $\alpha$  and  $\beta$  are constants representing properties of a given tissue type. In this model, the linear component is thought to represent the effect of directly lethal damage to the cells while the quadratic component is thought to represent cell-death due to accumulation of sub-lethal damage. The LQ model allows for dosage in different fractionation schemes to be calculated such that they result in the same survival fraction, a concept referred to as biologically effective dose (BED) [10]. As a result, prescribed dose in a regimen with greater fractionation tends to be higher in order to achieve the same BED.

Additionally, BED is dependent on the values of  $\alpha$  and  $\beta$ , specifically on the ratio of  $\alpha/\beta$ , which vary with different tissues. Cancerous tissue tends to have a higher value of  $\alpha/\beta$  than late responding normal tissue, such that the reduction in BED due to fractionation is greater for healthy tissues than cancerous tissues. As a result, fractionation generally allows for the therapeutic ratio to be increased by raising the BED delivered to cancerous tissue while keeping the BED of late responding healthy tissues constant. Traditionally the values of  $\alpha/\beta$  used in BED calculations were taken as 3 Gy for late responding normal tissues and 10 Gy for cancerous tissues [31].

Conceptually, the continuous radiation delivery of permanent seed brachytherapy may be viewed as a special case of fractionation in which treatment is given in an infinite

number of fractions separated by an infinitely small period of time. However, application of the usual equations for BED to permanent seed brachytherapy is complicated by the decaying dose rate over time and by the violation of the usual assumption that time between fractions is sufficient for all sub-lethal radiation damage to be repaired.

While traditional calculations for BED have used the values of 3 Gy and 10 Gy to represent  $\alpha/\beta$  of all cancerous and late responding normal tissues, respectively, recent research has explored breast cancer specific values of  $\alpha/\beta$ . Analysis of data from a phase III randomized clinical trial comparing different fractionation schedules of whole breast irradiation following lumpectomy showed that the difference in  $\alpha/\beta$  between healthy and cancerous tissue in this context may be much smaller than previously thought. Estimated  $\alpha/\beta$  for local-regional relapse was 4.6 Gy (95% CI 1.1–8.1 Gy) and for changes in breast appearance was 3.4 Gy (95% CI 2.3–4.5 Gy) [32]. This evidence suggests that the difference in  $\alpha/\beta$  between cancerous and healthy tissue in breast cancer may be smaller than previously thought, or possibly even reversed. A relatively low value of  $\alpha/\beta$  in breast cancer would support the use of hypofractionation, although the available data is not yet conclusive. Despite the clear implications of  $\alpha/\beta$  for fractionated radiotherapy, radiobiological models for comparing fractionated regimens to continuous, low dose rate radiotherapy (i.e. permanent seed brachytherapy) depend on the recovery rate of sub-lethal damage but are relatively independent of  $\alpha/\beta$  [33]. Thus, the implications of the emerging research on  $\alpha/\beta$  of cancerous and healthy breast tissue for permanent seed breast brachytherapy (discussed below) are unclear.

## 1.2 Accelerated Partial Breast Irradiation

### 1.2.1 Rationale and Key Concepts

In the years of clinical follow-up on the treatment of early-stage breast cancer with BCT, a pattern was observed in which recurrences were more likely to occur at the site of the originally treated tumour [13]. Research investigating the addition of a targeted boost of radiation to the tumour bed in addition to WBI showed improvements in ipsilateral recurrence [34], supporting targeted irradiation as a strategy to improve therapy.

If increased dose to high-risk regions could improve effectiveness, could reduced dose to low-risk regions reduce treatment burden? Such was the motivation for accelerated partial breast irradiation (APBI), the delivery of radiation to only a portion of the breast surrounding the original tumour site at an accelerated rate.

In the context of traditional WBI, the treatment burden is considerable, requiring frequent trips to the hospital over many weeks. Traditional radiation schedules separated treatment into 25 fractions of 2 Gy each [35] (50 Gy total), typically delivered once a day,

five days a week for five weeks. The addition of a targeted boost can extend the total treatment time to 6–7 weeks [34]. While more recent clinical trials have shown equivalent tumour control when whole breast irradiation is shortened to 40 Gy over 15 fractions (2.67 Gy each) [35], this 3-week radiation schedule remains burdensome.

The treatment burden is hypothesized to cause some women to choose mastectomy instead of BCT or even decline radiotherapy and accept an increased risk of recurrence, with evidence for that hypothesis reflected in both anecdotal [36] and statistical accounts [13]. Anecdotally, there is the account of a Venezuelan woman treated using interstitial brachytherapy at the Oschner Clinic in New Orleans, USA, the first APBI patient in the modern era, for whom there were no linear accelerators in her home country within 8 hours of her home [36]. Statistically, BCT is often underutilized, with the proportion of eligible patients who undergo BCT estimated between 35–80% and the proportion of patients who receive BCS but forego radiation therapy estimated between 15–30% [13]. The lengthy duration of radiation treatment is widely thought to contribute to this underutilization [37]. Additionally, several factors that increase the burden of an extended treatment; including distance to treatment, ambulatory status and rural populations; correlate with underutilization of BCT [13]. As a result, APBI is hypothesized to offer a tool to increase the utilization of BCT by eligible patients in addition to reducing the treatment burden of those who would have received radiation therapy regardless of treatment length.

Writing against this hypothesis, Yao & Recht [38] found that the increased use of APBI brachytherapy amongst breast cancer patients in the United States from 0.2–3.1% between 2000–2008 did not correspond to a reduction in the proportion of patients who did not receive radiotherapy. They conclude that the removal of “institutional, logistical and financial barriers” may be more promising avenues to reduce noncompliance [38]. Despite having data from over 300,000 patients, the authors lack data on the proportion of patients for whom APBI brachytherapy was available or their characteristics, nor on any control group that might account for other influences on treatment patterns. As a result, their attribution of a lack of reduction in non-compliance to a failed promise of APBI brachytherapy is largely without evidence.

The observation of the local nature of tumour control and recurrence as well as the significance of treatment burden on breast cancer patients, led to the rise of accelerated partial breast irradiation (APBI) as an active area of research. It was hypothesized that APBI could maintain tumour control with rates of adverse effects held constant or improved while accelerating the treatment and reducing the burden to the patient.

In planning and delivering APBI, target volumes are defined based on terminology



consistent with radiation therapy planning more broadly. In radiotherapy planning, gross tumour volume (GTV) refers to any visible tumour volume under imaging or clinical exam, while the clinical target volume (CTV) includes the GTV as well as subclinical disease not visible under imaging. The CTV thus defines the volume of tissue that is clinically relevant for treatment. The planning target volume (PTV) represents an expansion to the CTV to account for any inaccuracies in set-up or delivery [39]. In the context of APBI more specifically, treatment is generally delivered to the surgical cavity (seroma) following lumpectomy rather than to the tumour itself. Thus, GTV is not generally defined, while borders of the CTV and PTV are determined by expanding contours of the seroma; the fluid-filled cavity left behind from surgery.

### 1.2.2 Eligibility and Clinical Evidence

With the primary motivations for using APBI over WBI related to improving secondary treatment considerations, such as adverse effects and treatment burden, rather than the primary consideration of tumour control, inclusion criteria are limited to patients for whom tumour control from established therapy is already very good. Task groups representing national or international bodies have published recommendations for APBI eligibility criteria, including the American Brachytherapy Society [40], the American Society for Radiation Oncology [41], the American Society of Breast Surgeons [42], and the Groupe Européen de Curiethérapie-European Society for Therapeutic Radiology and Oncology (GEC-ESTRO) [43]. Additionally, many large-scale clinical trials (discussed below) have defined their own criteria. Despite variation between recommendations, most contain a minimum age ( $>45$ – $60$ ), a maximum tumour size ( $<2$ – $3$  cm), tumour margin requirements (negative margin  $>0$ – $2$  mm) and little to no lymph-node involvement ( $\leq 0$ – $3$  nodes). Eligibility recommendations of the task groups mentioned above are summarized by Tann et al. [44] and those used by various phase III clinical trials are described in the citations and clinical trial registry numbers given in Table 1.2.

The most robust source of evidence for the clinical efficacy of APBI is derived from five phase III randomized clinical trials (RCTs) comparing ipsilateral breast tumour recurrence following APBI and WBI. The results of these studies and the techniques of APBI they evaluated are given in Table 1.2, alongside descriptions of four ongoing phase III RCTs and their expected study completion dates (ESCD). Five-year recurrence rates in the control arms of the phase III RCTs published to date have all been  $\leq 1.5\%$ , illustrating the favorable prognosis of eligible patients. In the treatment arms, three of the five studies (GEC-ESTRO, Florence [NCT02104895], and IMPORT-LOW) have unambiguously promising results, with 5-year recurrence rates also  $\leq 1.5\%$ , none of which

were statistically significantly different from their control arms. Of the remaining two trials, ELIOT and TARGIT-A, both were delivered with intraoperative radiotherapy (IORT). Recurrence rates in the ELIOT trial were worse than the treatment arm (4.4% vs 0.4%,  $p < 0.0001$ ) while differences in recurrence rates of the TARGIT-A trial (3.3% treatment vs 1.3% control) had a p-value of 0.04. However, recurrence rate differences in TARGIT-A were deemed not significantly different by the study's authors due to a pre-defined significance level of 0.01 to reflect multiple comparisons [45]. The study's authors concluded the results demonstrated non-inferiority, although interpretation of the trial was met with considerable controversy when it was published (discussed in section 1.2.5 below).

Two recent reviews of the clinical efficacy of APBI reached contradictory conclusions, with one excluding IORT trials and concluding that the efficacy of APBI relative to WBI was supported [46], while the other included IORT trials and concluding the opposite [47]. Both reviews were written prior to the publication of the IMPORT-LOW trial, which provided additional evidence supporting APBI.

In summary, with the possible exception of IORT based approaches, data available from multiple large RCT's supports the use of APBI for well-selected patients, with results from other RCT's comprising an additional 10,000 patients pending in the coming years.

### 1.2.3 Interstitial and Intracavitary Breast Brachytherapy

The first modern treatment of APBI was delivered using interstitial breast brachytherapy [36], in which 15–25 needles are inserted into the breast and exchanged for flexible catheters [54]. With the catheters implanted, an afterloader is used to deliver HDR brachytherapy over the following week based on a treatment plan developed using CT. Treatment is typically fractionated over five days, after which the catheters are removed. LDR brachytherapy has been delivered using iodine-125 ( $^{125}\text{I}$ ) or iridium-192 ( $^{192}\text{I}$ ) but the most common source configuration is HDR  $^{192}\text{I}$  [55].

Despite initial success with interstitial brachytherapy, the technique was not widely adopted. Planning and delivering the procedure is time-consuming and requires a specialized skill set [37], and with limited availability of adequate training, adoption was largely limited to high-volume centres [13].

As a result, the intracavitary approach was developed to simplify breast brachytherapy, placing an instrument into the seroma through an incision where it expands to fill the cavity and is left in place. Like the interstitial approach, a remote afterloader is used to deliver a source through one or more lumens within the implanted device. The

Table 1.2: Summary of completed and ongoing phase III prospective randomized clinical trials comparing APBI to WBI. Adapted from Tann et al. 2016 [44] with the addition of recently published results from Coles et al. 2017 [48] on the IMPORT-LOW trial.

Trial	# of Patients in Trial	Follow-up Period (Years)	APBI Technique	5-Year LR, APBI vs WBI
TARGIT-A [49]	3451	2.4	IORT	3.3 vs 1.3
ELIOT [50]	1305	5.8	IORT	4.4 vs 0.4
GEC-ESTRO [51]	1184	5.0	MIB	1.4 vs 0.9
Florence (NCT02104895) [52]	520	5.0	EBRT (IMRT)	1.5 vs 1.5
IMPORT-LOW [48]	2018	6.0	EBRT (IMRT)	0.5 vs 1.5
IRMA (NCT01803958)	3302	Pending	EBRT (3D-CRT)	Pending (ESCD: Apr 2020)
NSABP B-39/ RTOG 0413 (NCT00103181)	4300	Pending	MIB or ICB or EBRT(3D-CRT)	Pending (ESCD: Apr 2020)
RAPID (OCOG) [53] (NCT00282035)	2135	Pending	EBRT(3D-CRT)	Pending (ESCD: Dec 2020)
SHARE (NCT01247233)	1006	Pending	EBRT(3D-CRT)	Pending (ESCD: Oct 2025)

3D-CRT: 3D conformal external-beam radiotherapy; ESCD: estimated study completion date (from clinicaltrials.gov as of Sep 2017), ICB: intracavitary brachytherapy, LR: local recurrence, MIB: multicatheter interstitial brachytherapy, IMRT: intensity modulated radiotherapy, IORT: intraoperative radiotherapy

first intracavitary device developed was the MammoSite applicator, approved by the FDA in 2002 [13], which contained a single centrally positioned lumen inside of a spherical balloon. The symmetrically shaped applicator and single lumen mean the device is unable to deliver asymmetrical dose distributions and adequate conformance to the seroma may be problematic [13]. Newer, multi-lumen devices such as the MammoSite ML (multi-lumen) and the Contura balloon applicator, as well as the non-balloon based strut adjusted volume implant (SAVI) device, have since been developed to offer greater dosimetric flexibility, including the delivery of asymmetrical plans. As of 2017, Hologic, the makers of MammoSite ML and the Contura device, claim that over 90,000 women in the United States have received intracavitary APBI using their devices [56].

#### 1.2.4 External Beam APBI

In addition to brachytherapy approaches to APBI, several techniques also exist using EBRT, principally 3D conformal radiotherapy (3D CRT) and intensity-modulated radiotherapy (IMRT). In 3D CRT, MLCs are used to modify the shape of the beams to conform to the outline of the PTV in the ‘beams-eye view,’ reducing the dose delivered to healthy tissue. Conversely, IMRT modifies both the shape and intensity of the beams, using the motion of the MLC leaves to modify the dose across the beam by leaving some portions of the field open for more time than others.

In completed and ongoing phase III clinical trials of APBI that incorporated an external beam arm, dose fractionation schemes range from 30–40 Gy to the PTV in 5–15 fractions [44]. The most common fractionation scheme, used in the three largest phase III clinical trials of EBRT, is 38.5 Gy in 10 fractions delivered over 5–10 days. A simulation-based dosimetric analysis of organs at risk during APBI suggested that EBRT-APBI techniques deliver less dose to OARs than WBI or MIB [28].

#### 1.2.5 Intraoperative Radiotherapy

Intraoperative radiotherapy (IORT), a form of brachytherapy, uses a mobile, electronic device implanted in the surgical cavity during the lumpectomy. Depending on the device, radiation may be delivered in the form of photons in the 30–50 keV range, or as electrons in the 3–12 MeV range [13]. By delivering radiotherapy concurrently with lumpectomy, radiotherapy is delivered without any additional treatment visits, making this approach the most convenient and timely option for patients. However, as was noted above, positive margins are typically an exclusion criterion for APBI and this information is not available at the time of lumpectomy. To address this, some studies have adopted a “risk-adapted” approach in which patients with adverse features identified post-lumpectomy were given standard WBI, a criterion affecting approximately 15% of

patients, with IORT serving as a radiation boost to the tumour bed [45].

There are two published phase III RCT's incorporating IORT, the ELIOT trial and the TARGIT-A trial, both of which are discussed in Table 1.2. ELIOT compared electron based IORT to WBI in an equivalence design and found that electron based IORT had significantly higher rates of recurrence (4.4% vs 0.4%, hazard ratio 9.3) [50]. Despite these rates being within a prespecified equivalence margin (7.5%) [50], the results were viewed as disappointing [57] and the increased recurrence attributed to patient selection [50, 57].

Conversely, TARGIT-A used photon based IORT and stratified sampling into pre- and post- histology groups. The pre-histology group was randomized prior to lumpectomy and used the risk-adapted approach described above, while the post-histology group was randomized after histology was available and IORT performed by reopening the surgical cavity. The TARGIT-A trial found 5-year local recurrence rates for TARGIT and EBRT of 3.3% and 1.3%, respectively ( $p = 0.04$ ), considered not statistically significant due to a pre-specified significance level of 0.01 to account for repeated tests due to an interim analysis published in 2010 [58]. The authors concluded that recurrence was within a pre-specified non-inferiority margin of 2.5% [49].

Publication of the results from the TARGIT-A trial were met with considerable controversy, with at least six commenting articles critical of the trial published in response [35, 57, 59–62]. Criticisms focus on a relatively short follow-up (median 2 years, 5 months), concerns around the statistical design and interpretation of a non-inferiority trial, and whether a decrease in non-breast-cancer related deaths is attributable to reduced radiation exposure. Despite IORT offering the potential for the shortest, most convenient treatment option, interpretation of the clinical evidence to date remains mired in controversy.

### 1.2.6 Emerging Techniques in APBI

In addition to the techniques described above, other emerging forms of APBI have also been described in the literature including non-invasive breast brachytherapy (NIBB) and ablative radiotherapy.

NIBB is delivered using the AccuBoost Brachytherapy System (Advanced Radiation Therapy, Inc., Billerica, MA). The system uses mammography-like compression paddles with on-board kV x-ray imaging to image the breast and deliver brachytherapy using applicators positioned on the opposite side of the paddles. An HDR  $^{192}\text{Ir}$  source is delivered to the applicators using an afterloader and the process repeated at both a medial-lateral and cranial-caudal orientation of the paddles [63]. Although the device

has been used for standalone APBI, clinical trials of this application of the device have so far been limited to assessment of 40 patients to evaluate feasibility and tolerability [63].

There are also emerging EBRT techniques for APBI, including stereotactic body radiation therapy (SBRT) and preoperative radiation therapy [64]. SBRT, also known as stereotactic ablative radiotherapy (SABR) [65], delivers radiotherapy in very large fractions, generally 10–20 Gy per fraction over 1–5 fractions [66]. Conversely, preoperative radiotherapy is a form of APBI that delivers radiotherapy pre-lumpectomy rather than post-lumpectomy, as is customary amongst more established APBI methods [64]. SBRT and preoperative radiotherapy are not mutually exclusive, with some SBRT trials delivering radiation preoperatively [64]. As of this writing, there are at least six ongoing trials of SBRT APBI as well as five ongoing trials of non-stereotactic, preoperative APBI [64].

### 1.2.7 Permanent Breast Seed Implantation

Pioneered at Toronto’s Sunnybrook Hospital, Permanent Breast Seed Implantation (PBSI) uses permanently implanted seeds of palladium-103 ( $^{103}\text{Pd}$ ) to deliver radiation therapy. Once the seeds are implanted, the patient is sent home while the seeds decay over the course of approximately two and a half months (half-life 17 days). Once decayed, the seeds are biologically inert and can safely remain in the patient. The use of permanently implanted seeds to deliver brachytherapy is used most widely in prostate brachytherapy, where seeds of  $^{125}\text{I}$  are implanted via needles inserted through the perineum [67]. PBSI uses the same principles as the prostate procedure [68], using the lower energy  $^{103}\text{Pd}$  seeds rather than  $^{125}\text{I}$  (average of 21 keV vs 27 MeV) in order to keep the radiation dose to others (e.g. patient’s partner/spouse) within safe levels [69, 70].

Currently, PBSI is planned and delivered according to the methods first described by Pignol et al. [68] and later modified by Batchelar et al [71]. A radiation treatment plan is crafted using a planning X-ray computed tomography (CT) scan with intraoperative image guidance provided by 2D ultrasound (US). The seroma and surrounding fibrosis is contoured in the CT scan and expanded by 10 mm, cropped to a minimum distance of 5 mm from the skin and chest wall, to define the CTV [27]. The PTV is an additional 5 mm expansion (15 mm total) that is also cropped 5 mm from the skin and chest wall [27]. Prescribed dose to the PTV is 90 Gy, with plans calling for (mean  $\pm$  SD)  $75 \pm 18$  seeds delivered using  $17 \pm 4$  needles [72].

Delivery of the treatment plan is then implemented intraoperatively using a standard needle template, felt markings outlining a projection of the PTV onto the skin surface, and intraoperative 2D US [71]. The needle template consists of a rectangular plate with

a regular grid of holes through which needles are inserted. The template is oriented such that needle trajectory is approximately tangential to the chest wall to minimize the risk of chest wall perforation. A ‘fiducial needle’ is inserted through the centre of the seroma in order to provide, in combination with the template, a reference for how far needles have been inserted [73]. With the fiducial needle inserted, the seed-bearing needles are inserted according to the dosimetric plan. Observed differences in seroma shape from the planning CT are noted by the clinician and any changes to the treatment plan made manually [71].

Clinical outcomes of a combined cohort of 134 patients are available with a median follow-up of 63 months [27]. Five-year local recurrence-free survival for the cohort was  $98.8 \pm 1.20\%$ , similar to estimates for the cohort based on established statistical tables (nomograms) of  $98.5 \pm 0.98\%$  ( $p =$  not significant) [27]. Rates of radiation-related side-effects were similar to that of whole breast irradiation [27].

In addition to clinical effectiveness of the procedure, a recently published study of cost-effectiveness found that the average societal cost (sum of costs to the healthcare system and patient) of treating a patient with PBSI is only modestly more than the cost of traditional 25-fraction WBI, \$8700 CAD vs \$6200 CAD [74]. Subsequent analysis of the paper’s findings, published as a letter to the editor in response to the study [75], showed their model predicts a ‘threshold distance’ of 94 km for one-way travel, above which the societal cost of PBSI is lower than WBI due to increasing patient travel costs. The letter further argues that, due to the model’s assumptions, the true threshold is likely lower [75]. The text of this letter and accompanying analysis are included in this thesis as Appendix A. Subsequent response from the study’s authors confirmed the modelled threshold and agreed with the hypothesis that the true threshold is likely lower [76].

To illustrate the significance of this threshold in the Canadian context, Figure 1.2 shows the resulting travel distance boundary around 46 Canadian radiation oncology centres. Based on our analyses and on the cancer centres identified, for Canadian patients living outside of the areas highlighted in red, PBSI is a more cost-effective option than 25-fraction WBI. We estimate that the areas for which PBSI is more cost-effective represent approximately 15% of the Canadian population.

Centres were identified based on directories of the Canadian Association of Radiation Oncologists and the Canadian Organization of Medical Physicists. Population estimates were made based on data from the Gridded Population of the World, version 4 as published by the United States National Aeronautics and Space Administration (NASA). A detailed description of the methods used to create the map and estimate the corresponding population, as well as a list of the radiation oncology centres identified are included

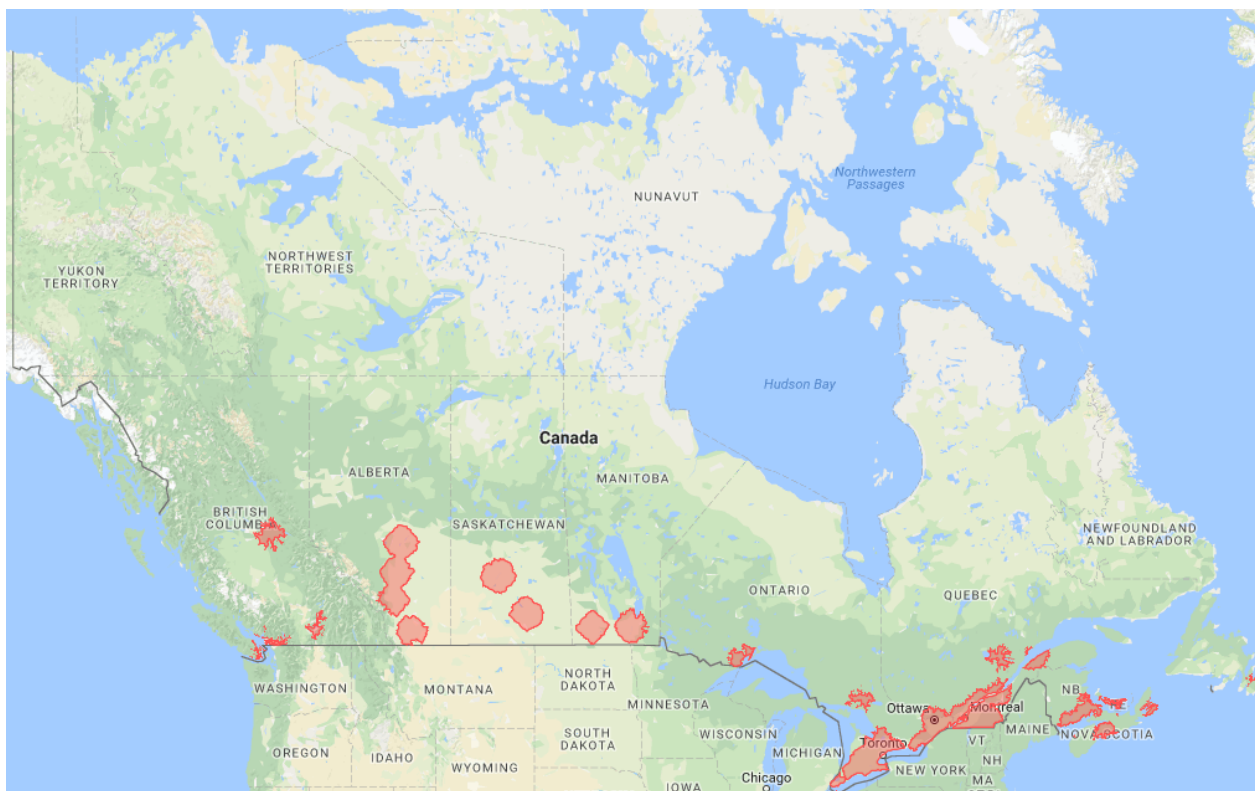


Figure 1.2: Illustration of the geographic areas of Canada within 93.6 km travel distance of a Canadian Cancer Centre. For Canadian patients living outside of the areas highlighted in red (estimated 15% of the Canadian population), our analysis revealed that PBSI is less costly than standard radiotherapy. Available online as an interactive map: <http://bit.ly/94kmMap>

in this thesis as Appendix B.

Highlighted areas are based on travel distance by car as estimated by Google Maps (Google Inc., Menlo Park, USA). Cities located outside the travel distance isoline include: Kamloops, BC (Pop. 90,000); Medicine Hat, AB (Pop. 63,000); Fort McMurray, AB (Pop. 61,000); Sault Ste Marie, ON (Pop. 73,000); North Bay, ON (Pop. 52,000); Sarnia, ON (Pop. 72,000); and Fredericton, NB (Pop. 58,000).

An additional study of PBSI is currently ongoing and recruiting participants [77]. Although inclusion/exclusion criteria have varied slightly for past studies of PBSI, summarized by Pignol et al. [27], the criteria used in the ongoing trial accepts patients  $\geq 55$  years of age with unifocal stage 0–1 breast cancer, a tumour  $\leq 2$  cm in size that is ER positive, clear surgical margins and without known genetic mutation in BRCA1/2 [77]. In addition to the aforementioned criteria, generally consistent with criteria for APBI in general, technical constraints of PBSI also require a seroma  $\leq 3$  cm in diameter that is



clearly visible in US and CT and that results in a PTV of  $\leq 125 \text{ cm}^3$ .

PBSI offers a promising technique for the delivery of APBI, decoupling the relationship between patient burden and duration of radiotherapy to achieve a convenient, single-visit therapy while maximizing the radiobiological benefits of prolonged radiation to deliver promising recurrence rates in phase I/II clinical trials.

## 1.3 Challenges of PBSI

### 1.3.1 Operator Dependence and Previous Work

PBSI is a technically demanding procedure and operator dependence has been previously highlighted as a challenge to making PBSI more generalizable [71]. Implantation accuracy is crucial to implant quality because, unlike when using an afterloader, there is no opportunity to correct for misplacement by varying dwell times or positions [73]. Furthermore, the use of lower-energy  $^{103}\text{Pd}$  makes the dose distribution more sensitive to misplacement than implants of  $^{125}\text{I}$  used in prostate brachytherapy [78]. Poor visibility of implanted seeds under 2D US has been described [79] and a learning curve effect reported with respect to dosimetry [72], highlighting the effect of the operator's skill and experience on implant quality. Even with an experienced operator, a recent study of seed placement error found a mean ( $\pm\text{SD}$ ) seed error of  $9 \pm 5 \text{ mm}$  between planned and implanted positions, with 5 out of 20 implants falling short of desired dosimetric coverage [80]. These error magnitudes compare unfavourably to those reported for LDR prostate brachytherapy of  $3 \pm 6 \text{ mm}$  [80]. Additionally, seeds have been shown to migrate between implantation and two-month follow-up, with a tendency to coalesce, resulting in hot spots in the implants, although the distance migrated by individual seeds was not evaluated [72].

Historically, operator dependence has played a significant role in determining the success of APBI brachytherapy techniques, impeding the dissemination of interstitial approaches [34] while catapulting the adoption of intracavitary ones [13]. The challenging nature of the interstitial approach has been blamed for its poor adoption [15], with its use limited primarily to high-volume centres [13]. The first intracavitary device, the Mammosite applicator, was developed explicitly to simplify breast brachytherapy with the goal of making it more widely available [81]. In stark contrast to the limited adoption of interstitial brachytherapy, over 40,000 intracavitary devices were sold even before 5-year data on safety and efficacy was available [34]. The success and failure of prior APBI approaches with respect to adoption underscores the importance of addressing operator dependence in PBSI. Simplifying and streamlining the procedure is not simply a matter of convenience or efficiency, but rather a prerequisite for its widespread use.

Work to date addressing operator dependence and reproducibility of the procedure has included changes to the workflow of the procedure [71, 82], and previous development of a custom imaging system [83]. The current approach of using a fiducial needle and template was itself the result of early experimentation by the pioneers of the technique to improve on freehand needle delivery, finding a reduction of seed placement error in a phantom study [82]. More recently, the Kelowna group improved reproducibility of patient setup by using a same-day CT simulation and by positioning the template support prior to sterilizing the surgical area when the absence of surgical drapes makes support adjustments easier to make [71].

The effect of visualization differences between CT and US on planning and dosimetry has also been explored using co-registered images of the seroma in CT and 3D US. Simulated shifts in the delivery of treatment plans based on differences in centroid between the two modalities were found to decrease mean coverage (V100) of the CT defined PTV by 10 % [84]. The authors recommended incorporation of 3D US into the planning procedure to account for the documented differences and found that delivery of the treatment plan to the combined PTV of both modalities was a viable option.

Lastly, a purpose-built imaging device has previously been proposed for PBSI in the form of a gamma camera. Designed to evaluate seed positions post-implantation, the proposed clinical device would use a pair of planar gamma cameras to capture 2D images based on the emitted photons of the seeds from orthogonal perspectives and use both images to triangulate the seed positions in three dimensions [83]. Images of an anthropomorphic phantom using a simplified prototype of the device, consisting of one camera and a repositioned phantom rather than two orthogonal cameras, was able to localize seeds within 30 seconds with a median error of 1 mm [83]. However, the device requires combination with a second, anatomical imaging modality (e.g. ultrasound) to relate seed positions to the target volume. Additionally, despite the obvious utility in intraoperative assessment, intraoperative guidance provided by the device is limited to the influence that knowledge of already implanted seeds has on the implantation of subsequent seeds, rather than offering implantation guidance prospectively.

Despite the valuable contribution of past researchers in this area, the problem of improving the simplicity and repeatability of PBSI remains unsolved.

### 1.3.2 Limitations of Intraoperative Guidance

The current approach of using freehand 2D US for intraoperative guidance poses two primary limitations: the lack of a fixed reference for implant coordinates during the procedure and challenges related to interpreting 3D anatomy from 2D images.

During LDR prostate brachytherapy procedures, both the transrectal ultrasound probe and the needle template are mounted to a “stepping” support, capable of finely adjusted translations on a stable platform. The use of a common support for the template and US probe allows the two to be co-registered and projections of the needle template overlaid on the live ultrasound image [67]. In this way, a series of fixed references (needle template projections) are visible at depth with respect to the target volume (prostate). The position and orientation of 2D transrectal ultrasound (TRUS) images can be reliably related to each other based on the known motion of the stepper.

Conversely, in PBSI, the position of ultrasound images with respect to the needle template is only approximately known and until the fiducial needle is placed there is no fixed reference. Even after the fiducial needle is placed, its use as a reference is impeded by ambiguity in the orientation of the US image with respect to the template and by an inability to identify the distance of the image from the fiducial tip when the fiducial needle is viewed in cross-section.

The lack of a robust fixed reference during the procedure makes it difficult to relate intraoperative US images to the coordinates of the planned implant. Without being able to precisely relate observed needle and seed positions to intended ones, opportunities for intraoperative feedback are limited, contributing to the difficulty and operator dependence of the procedure.

In addition to the lack of a fixed reference, the interpretation of 3D anatomy from a 2D imaging modality has well documented limitations [85]. The process of interpreting a 3D structure from a series of 2D images requires that the operator mentally transform the 2D images to gain an impression of 3D anatomy, a process that is both time-consuming and subjective [85]. Additionally, practical limits on probe positioning make certain image orientations difficult or impossible to view, such as planes parallel to the skin surface. Lastly, the ambiguity of needle position and orientation when viewed in cross-section under 2D US limits the ability to compare needle positions to other landmarks (e.g. local anatomy, other needles) unless those landmarks are visible with the needle trajectory in-plane with respect to the image. Together, these limitations of 2D US also contribute to the procedure’s operator dependence.

### 1.3.3 Imaging Dissimilarities Between Planning and Guidance

In addition to the challenges posed by limitations of intraoperative guidance, additional complexity is added by the dissimilarities between guidance (intraoperative) imaging and planning (preoperative) imaging. The two major contributors to those dissimilarities are differences in modality and time.

The current use of two different imaging modalities, CT for planning and US for guidance, creates dissimilar images that makes comparing intraoperative images to the preoperative plan more challenging. Images differ both in their appearance; such as the interpretation of bright/dark regions, contrast and texture; as well as the anatomical information contained.

With respect to anatomical information, the vastly different sources of the contrast observed in CT and US means that the information contained in images from each modality is fundamentally different, irrespective of how that image is represented. For instance, in current practice, target volumes are defined based on contours of the seroma and surrounding fibrosis [27], both of which are visible under CT. Conversely, ultrasound images allow for visualization of only the fluid-filled cavity and not the surrounding fibrosis [86], likely explaining why seroma volume studies have found smaller average seroma volumes when contouring in 3D US than in CT [87]. In addition to differences in size, differences in position have also been documented, with mean ( $\pm$ SD) centroid shifts of  $7 \pm 3$  mm [84]. As a result, identifying movement or deformation of the seroma and differences between actual and planned implants is confounded by differences in what can be seen in each modality.

In addition to the information content of each modality, more superficial differences in image appearance between modality, such as the reversal of seroma contrast (bright in CT, dark in US), limited slice thickness in CT, and speckle pattern in US also complicate the comparison of pre- and intra-operative images. Comparison is further complicated by a relative dearth of anatomical landmarks other than the target volume, such as would be provided by the urethra, bladder and rectum in prostate brachytherapy procedures.

The separation of pre- and intra-operative imaging with respect to time presents another source of dissimilarity between planning and guidance. Breast tissue is both mobile and deformable, presenting the opportunity for considerable motion between imaging sessions. A portion of this motion error is mitigated by using consistent protocols for patient positioning during planning and implantation [71], and through the addition of a same day simulation in order to minimize the time between imaging sessions [71]. While these protocols mitigate differences introduced by temporal separation, some residual error is unavoidable. Additionally, anesthesia induced tissue sag is present during the procedure but absent during the planning process. Although a laser levelling system and skin tattoos is used to account for shifts in patient position [71], internal or non-rigid motion is currently unaccounted for.

## 1.4 Thesis Objective

To address the operator dependence of PBSI, we propose the use of an intraoperative 3D US guidance system. Thus, the objective of this thesis is to develop and validate a 3D US guidance system that can be used during PBSI with minimal disruptions to the clinical workflow and to demonstrate the utility of the system in a proof-of-concept phantom procedure. By developing this system, we aim to simplify and streamline PBSI to make it easier for clinicians to adopt, with the ultimate goal of improving the available radiotherapeutic options for women with early stage breast cancer.

## 1.5 Relevant Physics: Brachytherapy and 3D Ultrasound

### 1.5.1 Brachytherapy Physics

As discussed in section 1.1.3, brachytherapy makes use of radioactive sources placed adjacent to the irradiation target. The relevant physics of energy deposition and distribution in this context are described below.

Radioactive decay of brachytherapy source material produces decay products characteristic of the source material. Most commonly used brachytherapy sources are gamma emitters, which produce photons of characteristic energies determined by the process(es) of disintegration for a given isotope.

In the case of permanent implants, where activity changes considerably over the course of treatment, the activity of the source and thus the dose rate delivered falls as the material decays but the photon energies remain the same. As a result, the relative spatial distribution of the dose also remains constant with time. That spatial distribution of dose is calculated for the purposes of planning and evaluating treatment according to the American Association of Physicists in Medicine task group 43 (TG43) formalism [88]. The TG43 formalism uses experimental data as the basis for generation of source-specific data tables used in a formula that summarizes the effects of attenuation in the surrounding material, anisotropy due to internal seed construction and angle-dependent effects of self-filtering as gamma rays exit the seed [88, 89]. The TG43 formalism models the surroundings of the seed as a homogeneous region of water and calculates the total dose resulting from multiple sources or source positions as the sum of their individual dose contributions. TG43 calculations make the simplifying assumption of ignoring inter-seed attenuation and, unlike dosimetry of external beam radiotherapy, ignores the effects of radiation scattering.

Clinically, the geometric distribution of dose around the source exhibits rapid fall-off due to the low energies used relative to external beam radiotherapy. This rapid fall-off

in dose allows for sparing of nearby normal tissue at the cost of making requirements for treatment accuracy more stringent [23]. As an illustration of the dose fall-off in  $^{103}\text{Pd}$  seeds, for two commercial models of cylindrically shaped seeds, dose rates 2.5 cm perpendicularly from the seed centre were <50 % of the dose rate 1 cm from the seeds, falling to <10 % at a distance of 5 cm [88].

### 1.5.2 Three-Dimensional Ultrasound Physics

Medical ultrasound is an imaging modality that uses focused pulses of acoustic energy to generate images of internal anatomy. Pulses of sound are generated by piezoelectric crystals in the ultrasound probe, or transducer, that reflect off of internal structures. A portion of those reflections return to the transducer and the piezoelectric crystal produces a signal. Using an assumed speed of sound in tissue of 1540 m/s and the time difference between sending and receiving the reflected pulse, the depth of the scattering structure that produced the reflection can be inferred. Historically, information along a single scan line, the path traversed by one pulse, could be displayed as an ‘A-mode’ scan. In modern systems, multiple ‘A-mode’ scans are performed along adjacent trajectories to create a ‘B-mode’ scan, displayed as a 2D grayscale image.

The geometry of adjacent trajectories in a B-mode scan and the mechanisms for producing them give rise to three categories of transducers: linear array, curved array, and phased array transducers [90]. In a linear array, transducer elements are arranged in a linear, 1D array with a subset of the elements used to generate a given scan line. By shifting the subset of elements used along the length of the array, a series of parallel scan lines are generated, resulting in a rectangular image with constant lateral resolution [90]. Conversely, a curved array also uses a 1D array of elements but with the elements arranged in a line that curves convexly. The result is a series of diverging scan lines that produce a pie-slice-shaped image, providing a larger field of view than a linear array, particularly at large depth settings, at the cost of a lateral resolution that worsens with increasing depth [90]. Lastly, a phased array uses beamforming to determine the direction of the scan line, introducing temporal delays between elements in the transmission and reception of ultrasonic pulses to change the direction of the wave produced by constructive interference between pulses from different elements. Images from phased arrays are approximately triangular and allow for images to be captured with a reduced transducer footprint, particularly important for applications where the acoustic window is limited (e.g. imaging through the space between adjacent ribs) [90]. In the context of PBSI, a relatively small and superficial target is to be imaged without constraints related to an acoustic window. As a result, a linear transducer is used.

While the path of each sound wave through the tissue may be thought of as a line, the sound wave passes through a column of tissue with finite size in all three dimensions, with the resulting image influenced by all the material contained within it. Furthermore, the shape of that column varies as a function of distance away from the probe, starting relatively wide at the probe, tapering to a minimum as it reaches the focal depth of the image and widening again beyond the focal depth. The result is a resolution in the lateral and elevational directions that varies with depth, reaching an optimum at the focal depth. Conversely, the axial resolution, determined by the duration of the US pulse, remains constant. Multiple transmit zones may also be used in which a composite image is formed from repeated pulses along the same path at different focal depths to improve the lateral and elevational resolutions.

Extending these principles to 3D US imaging can use one of three strategies: 1) 2D arrays, in which the 1D array of transducer elements used in 2D imaging is repeated to create a 2D grid for 3D imaging; 2) using an external sensor to track position and orientation of a freehand 2D US transducer and reconstructing a 3D image from the 2D images and their known positions in space; or 3) through the use of a mechanical approach, which mimics the position sensing strategy to reconstruct a 3D image from many 2D images but uses a mechanical or robotic actuator to constrain probe motion along a predetermined path [91].

Three-dimensional scanners using the mechanical approach may be further described by the motion of the US transducer as either linear, tilt/rotational, or hybrid scans, combining both linear and rotational motion simultaneously. In the case of the solution to be described in subsequent chapters, a mechanical 3D US system using a hybrid geometry has been developed. The hybrid geometry employed combines a linear translation and outward tilt, with linear and rotational motion maintaining a constant proportion: thus, all adjacent slices have equal linear and angular separation. The resulting spacing of 2D slices creates worsening elevational spacing with increased distance from the transducer due to the tilt component of the scan. Although the elevational direction of the transducer changes with tilt angle, for convenience the axes of the reconstructed scan may be described according to the axial, lateral and elevational directions of the 2D US transducer when the tilt angle is  $0^\circ$ .

## 1.6 Ultrasound Guidance of Brachytherapy Procedures

### 1.6.1 Three-Dimensional US Guidance of Prostate, HDR Breast Brachytherapy

Three-dimensional US has been previously used in the guidance of other brachytherapy procedures, including prostate brachytherapy, gynecological brachytherapy and interstitial breast brachytherapy. Bax et al. [92] developed a prostate guidance system that used a mechatronically rotated TRUS probe to capture a 3D image. In addition to using 3D US, the typical use of a co-registered needle template was extended to a co-registered mechanical linkage, creating a dynamic needle guide that allowed for oblique insertion [92]. Proof of concept work has also been performed using a mechatronically rotated TRUS probe for gynecological brachytherapy [93], as well as a 360° transvaginal US system for the same application [94].

In the case of interstitial breast brachytherapy, Poulin et al. developed a 3D US guidance system that used variable mounting positions and one degree-of-freedom of live tracking to register it to the compressive plates typically used in the procedure. Use of the system would potentially allow a CT scan to be avoided, streamlining patient workflow [95]. To prevent artifacts caused by probe motion, a thin plate of acoustically translucent polymethylpentene (TPX™) plastic is placed between the probe and the breast [95]. Despite being tailored to the needs of breast brachytherapy, its reliance on the presence of compressive templates on either side of the breast makes it inappropriate for the guidance of PBSI without further modification.

### 1.6.2 Other Methods of Needle and Needle Template Tracking and Guidance

While numerous mechatronic 3D US systems have been developed for needle guidance, other approaches to needle and needle template tracking exist, including the use of CT and magnetic resonance (MR) imaging techniques, optical tracking and pielectromagnetic (EM) tracking.

In the context of gynecological brachytherapy, guidance techniques using MR and CT imaging have been developed including iterative imaging following insertion of each needle, either with MR [96] or CT [97], as well as with near real-time (0.67 Hz) 0.5 T MR used intraoperatively [98]. For all of these techniques, specialized equipment and a time-consuming workflow pose major limitations to widespread adoption.

Optical tracking of tools has been widely adopted for various image guided interventions and is the most established modality in tracking devices for image guided interven-



tions [99]. Despite its widespread use, optical tracking suffers from a reliance on line of sight and would represent a relatively bulky complication to the operating room.

Electromagnetic tracking, which has the advantage of not requiring line of sight, has been applied to interstitial breast brachytherapy for insertion guidance [100], catheter reconstruction [101], and quality assurance [102]. However, the use of pre-loaded needles in PBSI would prohibit placement of sensors at the needle tips. Placement of sensors on the US transducer and needle template would be possible, but add considerable cost and complexity as a result of the specialized equipment and calibration protocols.

# References

- [1] Canadian Cancer Society’s Advisory Committee on Cancer Statistics. Canadian Cancer Statistics 2017. Technical report, Canadian Cancer Society, Toronto, 2017.
- [2] Jacques Ferlay, Isabelle Soerjomataram, Rajesh Dikshit, et al. Cancer incidence and mortality worldwide: Sources, methods and major patterns in GLOBOCAN 2012. *International Journal of Cancer*, 136(5):E359–E386, March 2015.
- [3] Canadian Partnership Against Cancer. Cancer Stage in Performance Measurement: A First Look - A System Performance Spotlight Report. Technical report, The Canadian Partnership Against Cancer, Toronto, 2015.
- [4] Starr Koslow and Rache M. Simmons. Principles of surgical treatment of invasive breast cancer. In John Benson, Gerald Gui, and Todd Tuttle, editors, *Early Breast Cancer*, chapter 35, pages 360–364. CRC Press, January 2013.
- [5] American Joint Committee on Cancer. Breast Cancer Staging (Poster). <https://cancerstaging.org/references-tools/quickreferences/Documents/BreastMedium.pdf>, 2009.
- [6] Carolyn C Compton, David R Byrd, Julio Garcia-Aguilar, et al. *AJCC Cancer Staging Atlas*. Springer New York, New York, NY, 2012.
- [7] D Craig Allred. Issues and updates: evaluating estrogen receptor- $\alpha$ , progesterone receptor, and HER2 in breast cancer. *Modern Pathology*, 23:S52–S59, May 2010.
- [8] Soo Youn Bae, Sangmin Kim, Jun Ho Lee, et al. Poor prognosis of single hormone receptor- positive breast cancer: similar outcome as triple-negative breast cancer. *BMC Cancer*, 15(1):138, December 2015.
- [9] Issa J Dahabreh, Helen Linardou, Fotios Siannis, George Fountzilas, and Samuel Murray. Trastuzumab in the Adjuvant Treatment of Early-Stage Breast Cancer:

- A Systematic Review and Meta-Analysis of Randomized Controlled Trials. *The Oncologist*, 13(6):620–630, June 2008.
- [10] Eric J. Hall and Amato J. Giaccia. *Radiobiology for the Radiologist*, volume 39. 7e edition, 2012.
- [11] G. Bonadonna, Gabriel N. Hortobagyi, and Pinuccia. Valagussa. *Textbook of breast cancer : a clinical guide to therapy*. Taylor & Francis, 2006.
- [12] Alexandra J. van den Broek, Marjanka K. Schmidt, Laura J. van ‘t Veer, Rob A.E.M. Tollenaar, and Flora E. van Leeuwen. Worse Breast Cancer Prognosis of BRCA1/BRCA2 Mutation Carriers: What’s the Evidence? A Systematic Review with Meta-Analysis. *PLOS ONE*, 10(3):e0120189, March 2015.
- [13] John A Cox and Todd A Swanson. Current modalities of accelerated partial breast irradiation. *Nature Reviews Clinical Oncology*, 10(6):344–356, April 2013.
- [14] Meena S Moran, Stuart J Schnitt, Armando E Giuliano, et al. Society of Surgical Oncology–American Society for Radiation Oncology Consensus Guideline on Margins for Breast-Conserving Surgery With Whole-Breast Irradiation in Stages I and II Invasive Breast Cancer. *International Journal of Radiation Oncology\*Biophysics\*Physics*, 88(3):553–564, March 2014.
- [15] Christopher F Njeh, Mark W Saunders, and Christian M Langton. Accelerated Partial Breast Irradiation (APBI): A review of available techniques. *Radiation oncology (London, England)*, 5(1):90, January 2010.
- [16] Gerald Gui. Skin-sparing forms of mastectomy. In John Benson, Gerald Gui, and Todd Tuttle, editors, *Early Breast Cancer*. CRC Press, January 2013.
- [17] Ian Kunkler. Breast Cancer. In Paul Symonds, Charles Deehan, John Mills, and Cathy Meredith, editors, *Walter & Miller’s Textbook of Radiotherapy: Radiation Physics, Therapy and Oncology*, chapter 26, pages 431–466. Elsevier Churchill Livingstone, 7th edition, 2012.
- [18] Pippa G. Corrie. Cytotoxic chemotherapy: clinical aspects. *Medicine*, 36(1):24–28, January 2008.
- [19] R. Wolters, A.C. Regierer, L. Schwentner, et al. A comparison of international breast cancer guidelines – Do the national guidelines differ in treatment recommendations? *European Journal of Cancer*, 48(1):1–11, January 2012.

- [20] Shruti Jolly, Larry L. Kestin, Neal S. Goldstein, and Frank A. Vicini. Pathologic Anatomy of Early-Stage Breast Cancer and Its Relevance to APBI: Defining the Target. In David E Wazer, Douglas W. Arthur, and Frank A. Vicini, editors, *Accelerated Partial Breast Irradiation: Techniques and Clinical Implementation*, chapter 3, pages 35–45. Springer-Verlag, Berlin, Heidelberg, 2nd edition, 2009.
- [21] Paul Symonds, Charles Deehan, John Mills, and Cathy Meredith. *Walter and Miller’s Textbook of Radiotherapy: Radiation Physics, Therapy and Oncology*. Elsevier Churchill Livingstone, 7th edition, 2012.
- [22] Markus Luster, Andreas Pfestroff, Heribert Hänscheid, and Frederik A Verburg. Radioiodine Therapy. *Seminars in nuclear medicine*, 47(2):126–134, March 2017.
- [23] Paolo Montemaggi and Patrizia Guerrieri. The Physics of Brachytherapy. In Paolo Montemaggi, Mark Trombetta, and Luther W. Brady, editors, *Brachytherapy: An International Perspective, Medical Radiology*, pages 13–28. Springer International Publishing, Cham, 2016.
- [24] Paul Symonds and Charles Deehan. Brachytherapy. In Paul Symonds, Charles Deehan, John Mills, and Cathy Meredith, editors, *Walter & Miller’s Textbook of Radiotherapy: Radiation Physics, Therapy and Oncology*, chapter 11, pages 189–200. Elsevier Churchill Livingstone, 7th edition, 2012.
- [25] Rajamanickam Baskar, Jiawen Dai, Nei Wenlong, Richard Yeo, and Kheng-Wei Yeoh. Biological response of cancer cells to radiation treatment. *Frontiers in Molecular Biosciences*, 1:24, November 2014.
- [26] A. Stewart and R. Dale. The Radiobiology of Accelerated Partial Breast Irradiation. In David E Wazer, Douglas W. Arthur, and Frank A. Vicini, editors, *Accelerated Partial Breast Irradiation: Techniques and Clinical Implementation*, chapter 4, pages 47–57. Springer-Verlag, Berlin, Heidelberg, 2nd edition, 2009.
- [27] Jean-Philippe Pignol, Jean-Michel Caudrelier, Juanita Crook, et al. Report on the Clinical Outcomes of Permanent Breast Seed Implant for Early-Stage Breast Cancers. *International Journal of Radiation Oncology\*Biology\*Physics*, 93(3):614–621, November 2015.
- [28] Jean-Philippe Pignol, Brian M Keller, and Ananth Ravi. Doses to internal organs for various breast radiation techniques - implications on the risk of secondary cancers and cardiomyopathy. *Radiation Oncology*, 6(1):5, January 2011.

- [29] T. J. Godden. Physical aspects of brachytherapy. A. Hilger in collaboration with the Hospital Physicists' Association, 1988.
- [30] G. Gordon Steel, T.J. McMillan, and J.H. Peacock. The 5Rs of Radiobiology. *International Journal of Radiation Biology*, 56(6):1045–1048, January 1989.
- [31] Alan E. Nahum. The Radiobiology of Hypofractionation. *Clinical Oncology*, 27(5):260–269, May 2015.
- [32] START Trialists' Group, S M Bentzen, R K Agrawal, et al. The UK Standardisation of Breast Radiotherapy (START) Trial A of radiotherapy hypofractionation for treatment of early breast cancer: a randomised trial. *The Lancet Oncology*, 9(4):331–341, April 2008.
- [33] Albert Van Der Kogel. The dose-rate effect. In *Basic Clinical Radiobiology Fourth Edition*, pages 158–168. CRC Press, March 2009.
- [34] Thomas A. Buchholz and Eric A. Strom. Accelerated Partial Breast Irradiation: History, Rationale, and Controversies. In David E Wazer, Douglas W. Arthur, and Frank A. Vicini, editors, *Accelerated Partial Breast Irradiation: Techniques and Clinical Implementation*, chapter 1, pages 1–17. Springer-Verlag, Berlin, Heidelberg, 2nd edition, 2009.
- [35] Joanne S Haviland, J Roger Owen, John A Dewar, et al. The UK Standardisation of Breast Radiotherapy (START) trials of radiotherapy hypofractionation for treatment of early breast cancer: 10-year follow-up results of two randomised controlled trials. *The Lancet. Oncology*, 14(11):1086–94, October 2013.
- [36] Robert R. Kuske. Brachytherapy Techniques: The Arizona Approach. In *Accelerated Partial Breast Irradiation*, pages 219–246. Springer Berlin Heidelberg, Berlin, Heidelberg, 2009.
- [37] David E. Wazer, Douglas W. Arthur, and Frank A. Vicini, editors. *Accelerated Partial Breast Irradiation*. Springer Berlin Heidelberg, Berlin, Heidelberg, 2nd edition, 2009.
- [38] Nengliang Yao and Abram Recht. Did the adoption of accelerated partial-breast irradiation reduce the noncompliance with adjuvant radiation in lumpectomy patients? *The American Journal of Surgery*, 212(1):178–179, July 2016.

- [39] Shahram Vaezy and Vesna Zderic. Image Guided Therapy Systems. Artech House, Norwood, MA, 2009.
- [40] Chirag Shah, Frank Vicini, David E Wazer, Douglas Arthur, and Rakesh R Patel. The American Brachytherapy Society consensus statement for accelerated partial breast irradiation. *Brachytherapy*, 12(4):267–77, January 2013.
- [41] Benjamin D. Smith, Douglas W. Arthur, Thomas A. Buchholz, et al. Accelerated Partial Breast Irradiation Consensus Statement From the American Society for Radiation Oncology (ASTRO). *International Journal of Radiation Oncology\*Biolog\*Physics*, 74(4):987–1001, July 2009.
- [42] The American Society of Breast Surgeons. The American Society of Breast Surgeons: Consensus Statement for Accelerated Partial Breast Irradiation. [https://www.breastsurgeons.org/new\\_layout/about/statements/PDF\\_Statements/APBI.pdf](https://www.breastsurgeons.org/new_layout/about/statements/PDF_Statements/APBI.pdf), 2011.
- [43] Csaba Polgár, Erik Van Limbergen, Richard Pötter, et al. Patient selection for accelerated partial-breast irradiation (APBI) after breast-conserving surgery: Recommendations of the Groupe Européen de Curiethérapie-European Society for Therapeutic Radiology and Oncology (GEC-ESTRO) breast cancer working group based on clinical evidence (2009). *Radiotherapy and Oncology*, 94(3):264–273, March 2010.
- [44] Anne W Tann, Sandra S Hatch, Melissa M Joyner, Lee R Wiederhold, and Todd A Swanson. Accelerated partial breast irradiation: Past, present, and future. *World Journal of Clinical Oncology*, 7(5):370, October 2016.
- [45] Jayant S. Vaidya, Frederik Wenz, Max Bulsara, et al. Risk-adapted targeted intra-operative radiotherapy versus whole-breast radiotherapy for breast cancer: 5-year results for local control and overall survival from the TARGIT-A randomised trial. *The Lancet*, 383(9917):603–613, February 2014.
- [46] Frank Vicini, Chirag Shah, Rahul Tendulkar, et al. Accelerated partial breast irradiation: An update on published Level I evidence. *Brachytherapy*, 15(5):607–615, 2016.
- [47] Brigid E Hickey, Melissa L James, Margot Lehman, et al. Hypofractionated radiation therapy for early breast cancer. *Cochrane Database of Systematic Reviews*, July 2016.

- [48] Charlotte E. Coles, Clare L. Griffin, Anna M. Kirby, et al. Partial-breast radiotherapy after breast conservation surgery for patients with early breast cancer (UK IMPORT LOW trial): 5-year results from a multicentre, randomised, controlled, phase 3, non-inferiority trial. *The Lancet*, 390(10099):1048–1060, September 2017.
- [49] Jayant S Vaidya, Frederik Wenz, Max Bulsara, et al. Risk-adapted targeted intraoperative radiotherapy versus whole-breast radiotherapy for breast cancer: 5-year results for local control and overall survival from the TARGIT-A randomised trial. *The Lancet*, 383(9917):603–613, February 2014.
- [50] Umberto Veronesi, Roberto Orecchia, Patrick Maisonneuve, et al. Intraoperative radiotherapy versus external radiotherapy for early breast cancer (ELIOT): a randomised controlled equivalence trial. *The Lancet. Oncology*, 14(13):1269–77, December 2013.
- [51] Vratislav Strnad, Oliver J Ott, Guido Hildebrandt, et al. 5-year results of accelerated partial breast irradiation using sole interstitial multicatheter brachytherapy versus whole-breast irradiation with boost after breast-conserving surgery for low-risk invasive and in-situ carcinoma of the female breast: randomised, phase 3, non-inferiority trial. *The Lancet*, 387(10015):229–238, January 2016.
- [52] Lorenzo Livi, Icro Meattini, Livia Marrazzo, et al. Accelerated partial breast irradiation using intensity-modulated radiotherapy versus whole breast irradiation: 5-year survival analysis of a phase 3 randomised controlled trial. *European Journal of Cancer*, 51(4):451–463, March 2015.
- [53] Ivo A. Olivotto, Timothy J. Whelan, Sameer Parpia, et al. Interim Cosmetic and Toxicity Results From RAPID: A Randomized Trial of Accelerated Partial Breast Irradiation Using Three-Dimensional Conformal External Beam Radiation Therapy. *Journal of Clinical Oncology*, 31(32):4038–4045, November 2013.
- [54] Rakesh Patel and Sushil Beriwal. Overview of North American Trials. In *Accelerated Partial Breast Irradiation*, pages 125–150. Springer International Publishing, 2009.
- [55] Jaroslaw T Hepel and David E Wazer. A comparison of brachytherapy techniques for partial breast irradiation. *Brachytherapy*, 11(3):163–75, January 2012.
- [56] Hologic. Frequently Asked Questions | 5-Day Radiation Therapy. <http://www.5daytherapy.com/patients/faqs#9>, 2017.

- [57] Meena S. Moran and Pauline T. Truong. Intraoperative Accelerated Partial Breast Irradiation: Caution Still Warranted. *International Journal of Radiation Oncology\*Biology\*Physics*, 89(3):496–498, July 2014.
- [58] Jayant S Vaidya, David J Joseph, Jeffrey S Tobias, et al. Targeted intraoperative radiotherapy versus whole breast radiotherapy for breast cancer (TARGIT-A trial): an international, prospective, randomised, non-inferiority phase 3 trial. *The Lancet*, 376(9735):91–102, July 2010.
- [59] Jack Cuzick. Radiotherapy for breast cancer, the TARGIT-A trial. *The Lancet*, 383(9930):1716, May 2014.
- [60] Jaroslaw Hepel and David E. Wazer. A Flawed Study Should Not Define a New Standard of Care. *International Journal of Radiation Oncology\*Biology\*Physics*, 91(2):255–257, February 2015.
- [61] Penny Mackenzie, Anthony Fyles, and Caroline Chung. Radiotherapy for breast cancer, the TARGIT-A trial. *The Lancet*, 383(9930):1717, May 2014.
- [62] John Yarnold, Birgitte Vrou Offeren, Ivo Olivotto, Philip Poortmans, and Rajiv Sarin. Radiotherapy for breast cancer, the TARGIT-A trial. *The Lancet*, 383(9930):1717–1718, May 2014.
- [63] Jaroslaw T. Hepel, Jessica R. Hiatt, Sandra Sha, et al. The rationale, technique, and feasibility of partial breast irradiation using noninvasive image-guided breast brachytherapy. *Brachytherapy*, 13(5):493–501, 2014.
- [64] Asal Rahimi and Robert Timmerman. New Techniques for Irradiating Early Stage Breast Cancer: Stereotactic Partial Breast Irradiation. *Seminars in Radiation Oncology*, 27(3):279–288, July 2017.
- [65] Filippo Alongi, Stefano Arcangeli, Andrea Riccardo Filippi, Umberto Ricardi, and Marta Scorsetti. Review and Uses of Stereotactic Body Radiation Therapy for Oligometastases. *The Oncologist*, 17(8):1100–1107, August 2012.
- [66] R Timmerman and B Kavanagh. Stereotactic Body Radiation Therapy. *Current Problems in Cancer*, 29(3):120–157, May 2005.
- [67] Peter Lim, Pei Shuen Hoskin. Prostate: Low Dose Rate Brachytherapy. In Paolo Montemaggi, Mark Trombetta, and Luther W. Brady, editors, *Brachytherapy:*



- An International Perspective, *Medical Radiology*, pages 299–318. Springer International Publishing, Cham, 2016.
- [68] Jean Philippe Pignol, Brian Keller, Eileen Rakovitch, et al. First report of a permanent breast  $^{103}\text{Pd}$  seed implant as adjuvant radiation treatment for early-stage breast cancer. *International Journal of Radiation Oncology\*Biology\*Physics*, 64(1):176–181, 2006.
- [69] Brian Keller, Raxa Sankreacha, Eileen Rakovitch, Peter O’Brien, and Jean-Philippe Pignol. A permanent breast seed implant as partial breast radiation therapy for early-stage patients: a comparison of palladium-103 and iodine-125 isotopes based on radiation safety considerations. *International Journal of Radiation Oncology\*Biology\*Physics*, 62(2):358–65, June 2005.
- [70] Brian M Keller, Jean-Philippe Pignol, Eileen Rakovitch, Raxa Sankreacha, and Peter O’Brien. A radiation badge survey for family members living with patients treated with a  $(^{103}\text{Pd})$  permanent breast seed implant. *International Journal of Radiation Oncology\*Biology\*Physics*, 70(1):267–71, January 2008.
- [71] Deidre Batchelar, Michelle Hilts, Tracey Rose, et al. Simulation and Intraoperative Checks for Improved Standardization and Reproducibility of Partial Breast Seed Implant Technique. In *Brachytherapy*, volume 13, page S84, March 2014.
- [72] Brian M Keller, Ananth Ravi, Raxa Sankreacha, and Jean-Philippe Pignol. Permanent breast seed implant dosimetry quality assurance. *International Journal of Radiation Oncology\*Biology\*Physics*, 83(1):84–92, May 2012.
- [73] Jean-Philippe Pignol and Brian M Keller. Permanent Breast Seed Implants. In *Accelerated Partial Breast Irradiation*, pages 263–276. 2009.
- [74] M. McGuffin, T. Merino, B. Keller, and J.-P. Pignol. Who Should Bear the Cost of Convenience? A Cost-effectiveness Analysis Comparing External Beam and Brachytherapy Radiotherapy Techniques for Early Stage Breast Cancer. *Clinical Oncology*, 29(3):e57–e63, March 2017.
- [75] J. Michael, J. Crook, D. Morton, et al. Reply to: Who Should Bear the Cost of Convenience? A Cost-effectiveness Analysis Comparing External Beam and Brachytherapy Radiotherapy Techniques for Early Stage Breast Cancer. *Clinical Oncology*, 29(6):392–393, June 2017.

- [76] M McGuffin, T Merino, B Keller, and J-P Pignol. Response to: 'Reply to: Who Should Bear the Cost of Convenience? A Cost-effectiveness Analysis Comparing External Beam and Brachytherapy Radiotherapy Techniques for Early Stage Breast Cancer'. *Clinical Oncology*, 15(0):302–310, April 2017.
- [77] ClinicalTrials.Gov. Partial Breast Irradiation Using Interstitial Permanent Palladium-103 Seed Implant (PBSI). <https://clinicaltrials.gov/ct2/show/NCT02297672>.
- [78] S Nath, Z Chen, N Yue, S Trumppore, and R Peschel. Dosimetric effects of needle divergence in prostate seed implant using 125I and 103Pd radioactive seeds. *Medical Physics*, 27(5):1058–66, May 2000.
- [79] Ananth Ravi, Curtis B Caldwell, Brian M Keller, Alla Reznik, and Jean-Philippe Pignol. Online gamma-camera imaging of 103Pd seeds (OGIPS) for permanent breast seed implantation. *Physics in Medicine and Biology*, 52(19):5921–32, October 2007.
- [80] Daniel Morton, Michelle Hilts, Deidre Batchelar, and Juanita Crook. Seed Placement in Permanent Breast Seed Implant Brachytherapy: Are Concerns Over Accuracy Valid? *International Journal of Radiation Oncology\*Biography\*Physics*, 95(3):1050–1057, February 2016.
- [81] Gregory K Edmundson, Frank A Vicini, Peter Y Chen, Christina Mitchell, and Alvaro A Martinez. Dosimetric characteristics of the MammoSite RTS, a new breast brachytherapy applicator. *International Journal of Radiation Oncology\*Biography\*Physics*, 52(4):1132–1139, March 2002.
- [82] JP Pignol, B Keller, E Rakovitch, et al. A breast permanent implant (BPI) for partial breast irradiation using 103Pd stranded seeds: A comparison of a 'free hand' versus a 'fiducial needle' technique. *Radiotherapy and Oncology*, 72:S57, September 2004.
- [83] Ananth Ravi, Curtis B Caldwell, and Jean-Philippe Pignol. Experimental evaluation of an online gamma-camera imaging of permanent seed implantation (OGIPSI) prototype for partial breast irradiation. *Medical Physics*, 35(6):2485–92, June 2008.
- [84] Daniel Morton, Deidre Batchelar, Michelle Hilts, Tanya Berrang, and Juanita Crook. Incorporating three-dimensional ultrasound into permanent breast seed

- implant brachytherapy treatment planning. *Brachytherapy*, 16(1):167–173, January 2017.
- [85] A Fenster, D B Downey, and H N Cardinal. Three-dimensional ultrasound imaging. *Physics in Medicine and Biology*, 46(5):R67–99, May 2001.
- [86] Jean-Philippe Pignol and Juanita Crook. Breast Brachytherapy: Permanent Breast Seed Implants – How and Why? In Paolo Montemaggi, Mark Trombetta, and Luther W. Brady, editors, *Brachytherapy: An International Perspective*, pages 185–196. Springer, Cham, 2016.
- [87] Tanya S Berrang, Pauline T Truong, Carmen Popescu, et al. 3D Ultrasound Can Contribute to Planning CT to Define the Target for Partial Breast Radiotherapy. *International Journal of Radiation Oncology\*Biophysics*, 73(2):375–383, February 2009.
- [88] Mark J Rivard, Bert M Coursey, Larry A DeWerd, et al. Update of AAPM Task Group No. 43 Report: A revised AAPM protocol for brachytherapy dose calculations. *Medical Physics*, 31(3):633–74, March 2004.
- [89] Ravinder Nath. Dosimetry of interstitial brachytherapy sources: Recommendations of the AAPM Radiation Therapy Committee Task Group No. 43. *Medical Physics*, 22(2):209, February 1995.
- [90] K Kirk Shung and Jesse Yen. Array Transducers and Beamformers. In Aaron Fenster and James C. Lacefield, editors, *Ultrasound imaging and therapy*, chapter 1, pages 3–37. CRC Press, Boca Raton, 2015.
- [91] Aaron Fenster, Grace Parraga, and Jeff Bax. Three-dimensional ultrasound scanning. *Interface focus*, 1(4):503–19, August 2011.
- [92] Jeffrey Bax, David Smith, Laura Bartha, et al. A compact mechatronic system for 3D ultrasound guided prostate interventions. *Medical Physics*, 38(2):1055–1069, January 2011.
- [93] Jessica Robin Rodgers, Kathleen Surry, Eric Leung, David D’Souza, and Aaron Fenster. Toward a 3D transrectal ultrasound system for verification of needle placement during high-dose-rate interstitial gynecologic brachytherapy. *Medical Physics*, 44(5):1899–1911, May 2017.

- [94] Jessica R. Rodgers, Kathleen Surry, David D'Souza, Eric Leung, and Aaron Fenster. 360-degree 3D transvaginal ultrasound system for high-dose-rate interstitial gynaecological brachytherapy needle guidance. In Neb Duric and Brecht Heyde, editors, *SPIE Medical Imaging*, volume 10139, page 101390T. International Society for Optics and Photonics, March 2017.
- [95] Eric Poulin, Lori Gardi, Kevin Barker, et al. Validation of a novel robot-assisted 3DUS system for real-time planning and guidance of breast interstitial HDR brachytherapy. *Medical Physics*, 42(12):6830–9, December 2015.
- [96] Tina Kapur, Jan Egger, Antonio Damato, Ehud J. Schmidt, and Akila N. Viswanathan. 3-T MR-guided brachytherapy for gynecologic malignancies. *Magnetic Resonance Imaging*, 30(9):1279–1290, November 2012.
- [97] Larissa J. Lee, Antonio L. Damato, and Akila N. Viswanathan. Clinical outcomes of high-dose-rate interstitial gynecologic brachytherapy using real-time CT guidance. *Brachytherapy*, 12(4):303–310, July 2013.
- [98] Akila N. Viswanathan, Robert Cormack, Caroline L. Holloway, et al. Magnetic resonance-guided interstitial therapy for vaginal recurrence of endometrial cancer. *International Journal of Radiation Oncology\*Biography\*Physics*, 66(1):91–99, September 2006.
- [99] Alfred M. Franz, Tamas Haidegger, Wolfgang Birkfellner, et al. Electromagnetic Tracking in Medicine - A Review of Technology, Validation, and Applications. *IEEE Transactions on Medical Imaging*, 33(8):1702–1725, August 2014.
- [100] H. Brastianos, T. Vaughan, M. Westerland, et al. Electromagnetic Tracking for Catheter Insertion Guidance for High-Dose-Rate Breast Brachytherapy: A Phantom Experiment. *International Journal of Radiation Oncology\*Biography\*Physics*, 96(2):E643, October 2016.
- [101] Eric Poulin, Emmanuel Racine, Dirk Binnekamp, and Luc Beaulieu. Fast, automatic, and accurate catheter reconstruction in HDR brachytherapy using an electromagnetic 3D tracking system. *Medical Physics*, 42(3):1227–1232, February 2015.
- [102] Markus Kellermeier, Jens Herbolzheimer, Stephan Kreppner, et al. Electromagnetic tracking (EMT) technology for improved treatment quality assurance in interstitial brachytherapy. *Journal of Applied Clinical Medical Physics*, 18(1):211–222, 2017.

# Chapter 2

## System Development and Validation

### 2.1 Introduction

The standard of care for early stage breast cancer is breast conserving therapy (BCT) [1], consisting of lumpectomy followed by whole breast irradiation (WBI) in fractionated doses over 3–7 weeks [2]. Despite cancer recurrence rates equivalent to mastectomy while preserving the breast [3], BCT may be underutilized, with some patients opting instead for mastectomy in order to avoid radiation [4], a decision often influenced by the lengthy duration of WBI [5]. These findings have contributed to an active area of research in accelerated partial breast irradiation (APBI) in an effort to reduce the burden of treatment and increase access to care.

Permanent breast seed implantation (PBSI) is one of a variety of APBI techniques that have been developed [4, 6]. PBSI delivers low-dose-rate brachytherapy using permanently implanted Palladium-103 ( $^{103}\text{Pd}$ ) seeds during a single procedure lasting 1–2 hours [7, 8]. By using permanently implanted seeds, radiation procedure time is reduced to a single visit with radiation dose to the heart and other organs at risk minimized [9]. Seeds are implanted on an outpatient basis, with seed placement planned using pre-operative x-ray computed tomography (CT). In the current workflow [2], intraprocedural guidance is provided by live freehand 2D ultrasound (US), using a template in an articulated arm and adjusted for the chosen angle of entry. A non-seed-bearing ‘fiducial’ needle acts as an US landmark.

Follow up of 134 PBSI patients showed 5–year recurrence rates similar to the expected outcomes for WBI with an improved side effect profile [2]. Despite positive outcomes, post-implant assessment of 20 PBSI patients showed a mean ( $\pm$ SD) difference of  $9 \pm 5$  mm between planned and implanted positions, comparing unfavorably to the estimated 3–6 mm accuracy achieved in permanent seed prostate implants [8]. Some cases

indicated a systematic bias in implant position, suggesting issues related to setup reproducibility [8]. Acceptable dosimetry has been reported for PBSI, with the volume of the evaluative PTV (seroma + 0.5 cm) receiving 100% of the prescribed dose being 91 % for the first 25 patients treated in an early cohort, increasing to 95 % for the final 10 [10]. However, technical challenges such as the use of different image modalities in the planning and guidance of the procedure, and the lack of a registered coordinate system for needle guidance at depth, such as the co-registered US stepping unit present in prostate implant procedures, represent areas for improvement [8]. In addition to implantation accuracy, standardization and reproducibility of the procedure have also been highlighted as an area of research, with the goal of making PBSI more easily adopted [11].

Previous improvements to the workflow and accuracy of the procedure have been limited to the use of needle template guidance and checks of patient alignment [11, 12]. Pignol et al. improved upon free-hand needle insertion using a template and fiducial needle [12], while Batchelar et al. incorporated a same-day CT simulation and intraoperative physical checks using a room laser and external markers [11]. These intraoperative checks assist in setup positioning but cannot account for non-rigid breast deformation and still require imaging to locate internal targets. A gamma camera system to intraoperatively locate implanted seeds has also been explored [13, 14], however its use as a guidance tool is limited to identifying seed displacements rather than minimizing displacements prospectively and would require additional development to integrate it with a second, anatomical imaging modality [14]. Despite these prior works, the unmet needs of a reproducible technique with fixed reference and common-modality planning and guidance persist.

Similar needs have been previously addressed for permanent seed prostate brachytherapy [15] and breast multicatheter interstitial brachytherapy (MIB)[16] using US systems with registered needle guides. In prostate brachytherapy, the standard delivery method uses a mechanical stabilizer that supports both a transrectal US (TRUS) probe and a co-registered needle template. Co-registration of the template allows projections of the needle template positions to be overlaid on the TRUS images, providing a fixed reference at depth during the procedure [17]. Numerous groups have developed robotic systems to extend the technique to 3D US imaging [18].

The breast MIB guidance system developed by Poulin et al. used an analogous approach to prostate brachytherapy, registering a needle template to a robotic 3D US scanner [16]. The registered needle guide consisted of two parallel plates compressing the breast on the medial and lateral aspects. The scanner was fixed between the plates and tracked in one rotational degree-of-freedom (DoF) using an encoder, with a second

translational DoF provided by multiple mounting positions. A thin plate of sonolucent polymethylpentene (TPX<sup>TM</sup>, Mitsui Chemicals, Tokyo, Japan) plastic, acoustically coupled with US gel on both sides, was positioned between the 2D probe and the breast to prevent motion artifacts due to probe movement. The system facilitated intraprocedural planning, allowing a pre-implant CT to be omitted. Though suitable for planning and guidance of MIB breast brachytherapy, the system described by Poulin et al. relies on compressive, parallel plates used in MIB but not in PBSI. Since PBSI is delivered to an unconstrained breast, registering the scanner and template requires six DoF's rather than two and accommodation of greater distances between the scanner and template.

Alternate approaches to catheter guidance include electromagnetic (EM) tracking and the use of intraoperative magnetic resonance imaging (MRI) guidance. EM tracking has been previously proposed for catheter reconstruction in HDR brachytherapy [19], including breast [20, 21] and prostate brachytherapy [22]. However, the use of pre-loaded needles in PBSI presents a considerable complication with respect to placement of EM sensors on the needles. Intraoperative MRI has been previously used to guide gynecological brachytherapy [23, 24], however the cost and complexity of specialized facilities required would pose major limitations to clinical adoption.

To address the additional technical requirements, we have developed a 3D US guidance system with the necessary DoF's and range of motion for template tracking in PBSI. We propose use of the system in PBSI with the goal of improving the accuracy and decreasing operator dependence of the implant procedure. To our knowledge, there have been no prior reports of a patient or phantom PBSI procedure guided with intraprocedural 3D imaging. In this thesis, we present the development and validation of the guidance system, culminating with its use in a phantom procedure.

## 2.2 Materials and Methods

### 2.2.1 System Design

The system consists of three components: 1) a 3D US scanner, 2) an encoded tracking arm mounted to the scanner, and 3) a needle template with fiducial divots at known locations. With the scanner and needle template held in fixed positions, the tracking arm is used to locate the template fiducials, registering the needle template (Figure 2.2a).

#### 2.2.1.1 Three-Dimensional US Scanner

The 3D US scanner uses a modification of the previously described assembly developed for breast MIB [16]. Briefly, a motorized scanner sweeps a 2D US probe through a pre-defined 'hybrid' motion, combining 5 cm of linear translation and 60° angular tilt. A

connected personal computer (PC) controls the scanner and reconstructs 150 2D images, each separated by 0.33 mm and 0.4°, into a 3D image with an approximately trapezoidal cross-section (Figure 2.1) and width equal to the width of the 2D images. While the scanner can be adapted to any 2D US system and transducer, experiments were conducted using a Phillips iU22 US system with an L12-5 linear transducer (Philips Ultrasound, Bothell, USA). Reconstructed voxel size increased with increasing depth setting, ranging from 0.07–0.13 mm in the lateral and axial directions, and 0.17 mm in the elevational direction. The field of view is 50 mm wide with a height equal to the depth of the 2D images (40–80 mm) and length equal to the sum of the scanner’s linear translation and the 2D image depth (90–130 mm, total). The scanner’s frame rate is set to be slower than the 2D US system to avoid repeated frames, causing scan time to vary from 10–18 seconds depending on depth and other settings of the 2D system. Image reconstruction is performed continually during image acquisition and the 3D image is available immediately after scan completion. During use, the scanner is rigidly held by an adjustable, counterbalanced mechanical arm.

#### 2.2.1.2 Encoded Arm and Modified Needle Template

The needle template is intermittently tracked in order to register it to the 3D US image, allowing a 3D visualization of the needle template and projections of the needle trajectories onto the 3D image to be displayed on a PC during the procedure (Figure 2.1). Template holes have a grid spacing of 5 mm and are sized to accommodate 18 gauge needles (1.27 mm diameter) with the exception of the centre position, sized for 17 gauge needles (1.47 mm diameter), matching clinically used seed-bearing and fiducial needles, respectively.

Template registration is accomplished using a passive mechanical tracking arm mounted to the 3D US scanner (Figure 2.2a). The tracking arm has three, 3D printed nylon segments that each rotate at a one DoF joint, with the arm segment most proximal to the scanner 30 mm in length and the remaining two segments 65 mm each. Each joint is tracked by a 12-bit magnetic encoder and measurements communicated to the PC using a BEI USB sensor interface (BEI Sensors, Thousand Oaks, USA), allowing the position of the arm to be calculated. The end effector of the arm is a stainless-steel ball 12.7 mm in diameter that seats into conical, fiducial divots on a modified needle template. By measuring the positions of four non-collinear divots, the needle template is registered with the 3D US image by rigid, homologous-point-based (landmark) registration [25]. Once the template is registered, the arm may be folded against the scanner.

Material costs of the tracking arm, including encoders, sensor board and the 3D printed segments, are in the hundreds of Canadian dollars.



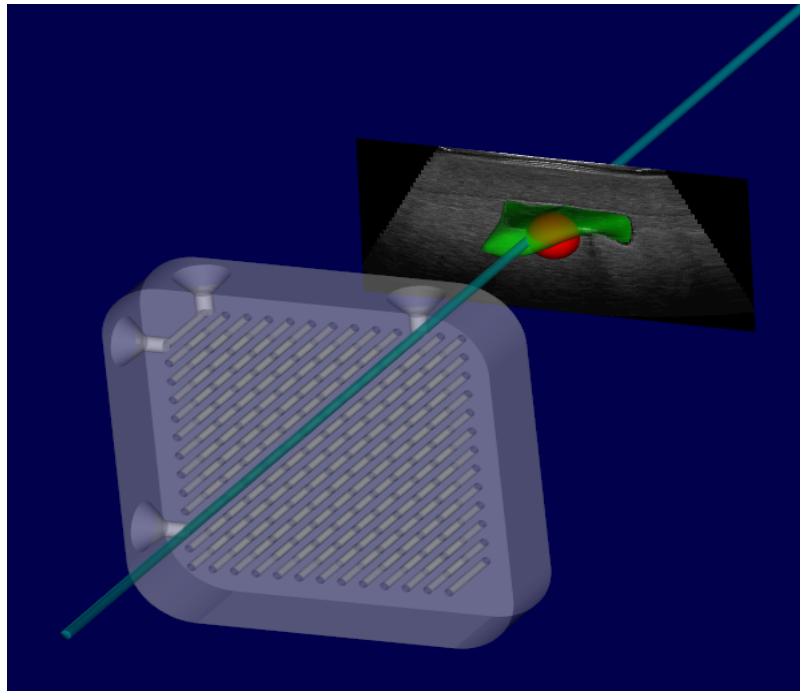


Figure 2.1: Screenshot from guidance software showing registered needle template relative to central slice of 3D US image and segmented seroma phantom (green). Teal cylinder indicates projection of selected needle template position.

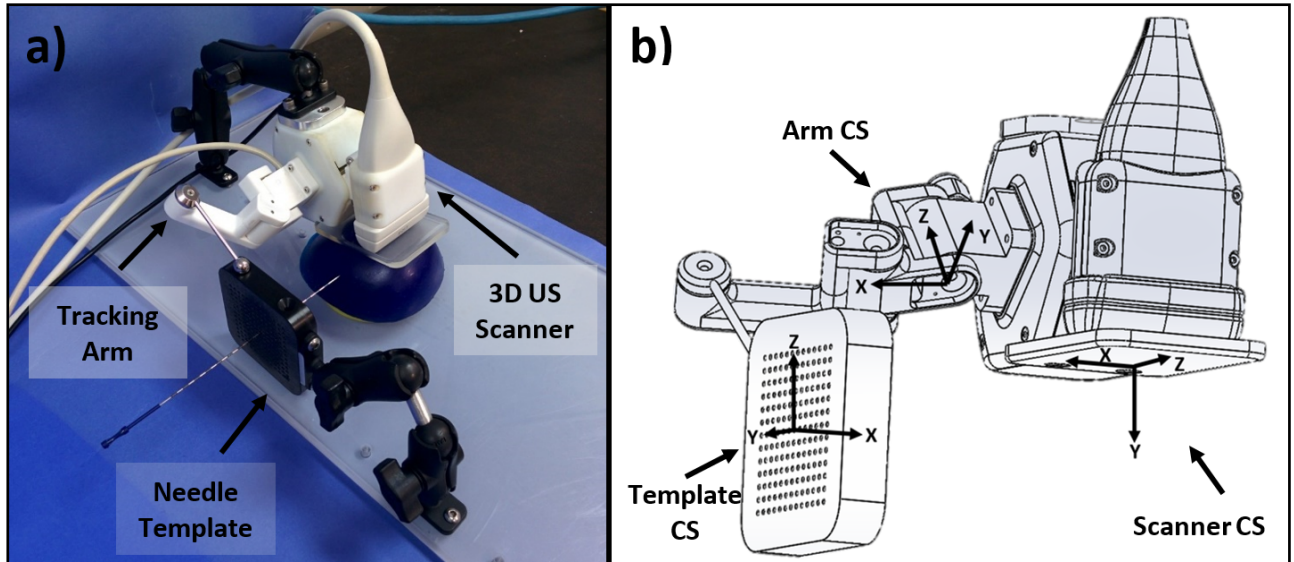


Figure 2.2: a) Image of guidance system positioned above commercial breast phantom. b) Illustration of coordinate systems (CSs) used in validation ('Image' CS not shown).

### 2.2.2 System Calibration and Validation

The validation strategy for the system and its components is summarized in Figure 2.3, outlining the flow of information through the system and the experimental validation of each step. An additional experiment validates the system as a whole by guiding a mock procedure in a phantom. The constructed system and an illustration of its coordinate systems (CSs) are shown in Figure 2.2b. Axes of the template CS are parallel with the template grid and its origin aligned with the centre template position. The arm CS has its Z and Y axes parallel with the rotation axes of the first and second joints, respectively, and its origin at the point on the first joint axes closest to the second joint axis. The axes of the scanner CS are parallel with the lateral, axial and elevational axes of the 2D US transducer when centred and the CS origin on the bottom surface of the TPX plate. Axes of the reconstructed 3D US image (image CS, not shown) are approximately parallel with those of the scanner coordinate system and its origin at the centre of the X-Z image plane closest to the probe, such that the two CS's are nearly coincident.

#### 2.2.2.1 Three-Dimensional Image Reconstruction

The generated 3D image was tested for accuracy of the reconstruction and for in vivo suitability of the scanner. Linear measurements were validated using a previously described [26] phantom consisting of four parallel layers of strings, each 10 mm apart. Each layer of the phantom is arranged in a 10 mm by 10 mm grid pattern and immersed

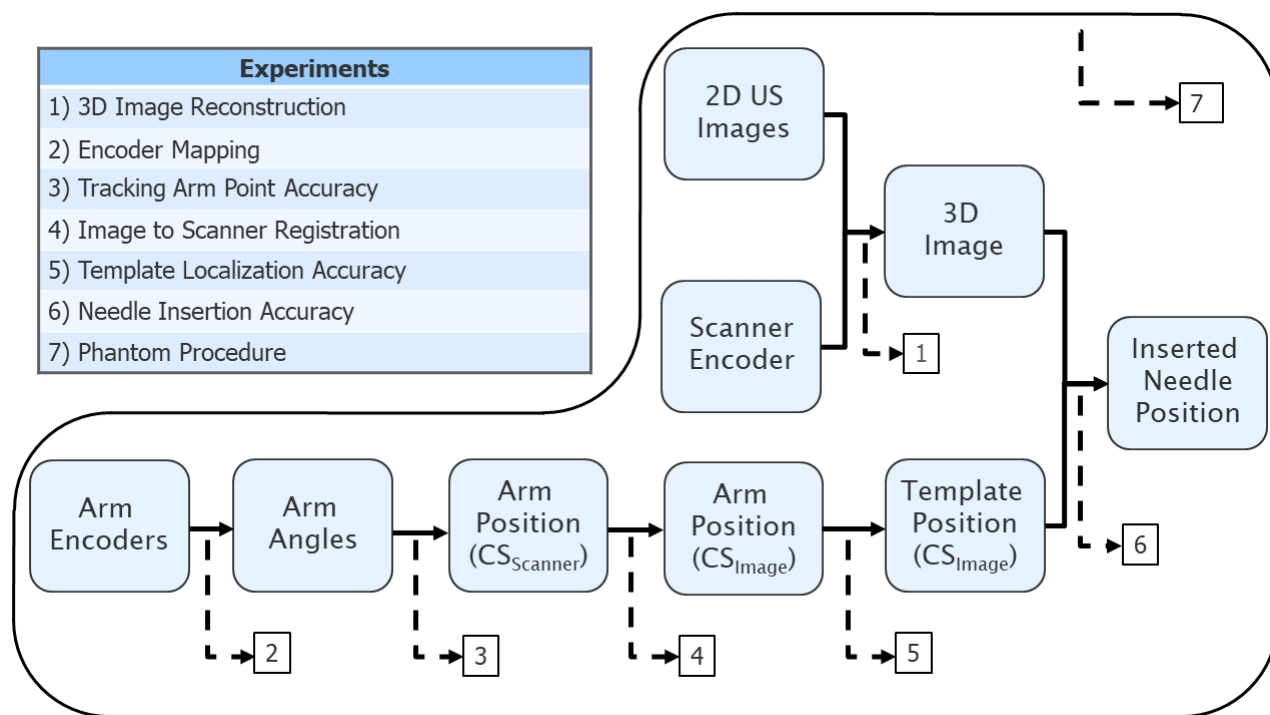


Figure 2.3: Summary of information pipeline in the guidance system and the list of experiments used in validation. Experiments 1–6 validate a step in the process indicated by dashed arrows. Experiment 7 evaluates the process as a whole. CS = coordinate system.

in a water-isopropanol bath (7.25 % isopropanol by volume) in order to match the nominal speed of sound in tissue, 1540 m/s [27]. Scans were taken of the immersed phantom at six depth settings (40, 45, 50, 60, 70 and 80 mm, respectively) and 40 manual measurements of the distance between adjacent, parallel strings were taken per direction per depth setting in the lateral and elevational directions. Axially separated strings are offset to prevent shadowing and measurements in this axis taken between perpendicular strings.

Volumetric validation was performed by scanning and manually segmenting two seroma-shaped agar phantoms and comparing segmentation volume to measured water displacement. The seroma-shape of the phantoms was created by forming the agar in 3D printed moulds matching seroma contours of 3D US scans of 2 PBSI patients. Contoured 3D US images were captured using an optically tracked, 2D US transducer (RESTITU Platform, Resonant Medical Inc., Montreal, Canada). Phantom material consists of an agar and glycerol mixture (by mass, 3 % and 8 %, respectively) having a speed of sound of 1540 m/s at room temperature [28]. No scattering agent was added to the seroma phantom, simulating the hypoechoic appearance of a seroma under US, while 3 g/l of SigmaCell cellulose (Sigma-Aldrich, St. Louis, USA) was added to the background material to create contrast and simulate the surrounding breast tissue. Phantoms were scanned using the developed 3D US system, resampled at 1 mm intervals and manually contoured using 3D Slicer [29]. Contour volumes were compared to water displacement measurements, each of which was repeated 4 times per phantom.

In-vivo image quality was assessed using breast scans taken of one healthy female volunteer. Scans were captured in accordance with the University of Western Ontario Institutional Review Board approved protocol by an experienced ultrasonographer who provided qualitative feedback on image quality, acoustic coupling, and device usability.

#### 2.2.2.2 Encoder Mapping

For each tracking arm encoder, errors were mapped and corrected for to improve the accuracy of the tracking arm. Encoders were calibrated by mounting each segment of the arm above a surface plate and correlating encoder measurements with known angular geometries to create a calibration table.

To provide known geometries, a unique setup was required for each joint. For the joint most distal to the base of the arm, the arm's existing spherical tip was placed on top of gauge blocks to set the tip's height above the surface plate and the height of the joint was measured with a height gauge (Figure 2.4a). The angle of the joint with respect to the surface plate was calculated from geometry, providing a known angle. When calibrating the middle joint of the arm, the calibration process was repeated with the most distal segment removed and a tooling ball inserted in its place (Figure 2.4b, left). Finally, the

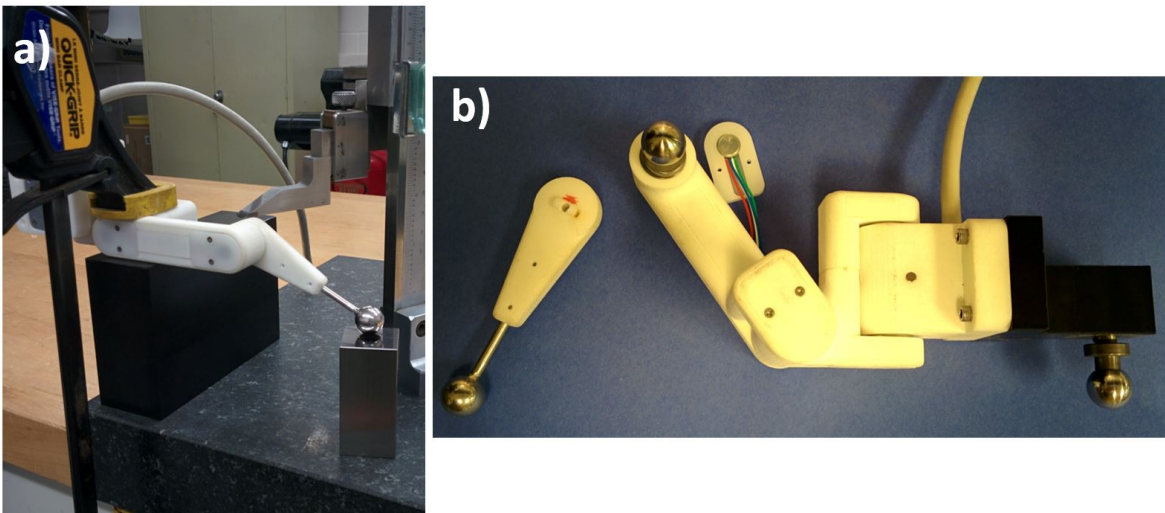


Figure 2.4: Encoder mapping set-up. a) Surface plate, gauge blocks and height stand in use during calibration of the most distal joint. b) Partially disassembled template tracking arm with tooling balls. The most distal segment (left) has been removed and a tooling ball added in its place. A machined extension and tooling ball (right) has been added.

most proximal joint was calibrated by attaching a machined extension 35 mm in length with a tooling ball at its end to the base of the arm (Figure 2.4b, right), such that the extended length was equal to the other segments of the arm (65 mm). For all joints, gauge block heights and encoder readings were recorded in approximately  $1^\circ$  intervals of joint motion by making variable increments in gauge block height.

The sensitivity of angle to gauge block height increases as the joint angle approaches vertical, making this calibration method suitable for only a limited angular range (approximately  $\pm 80^\circ$  from horizontal). To span the full range of each joint, 3–6 different mounting positions were used per encoder to take measurements in overlapping regions of the encoder’s range.

An integral error offset was calculated between mounting positions by interpolating data in overlapping regions to create corresponding points between two mounting positions and computing the mean difference between them. Encoder mapping produced a plot of each encoder’s integral (accumulated) error as a function of encoder position with the integral arbitrarily beginning from the first position measured.

Once the integral error of each encoder was measured, the result was smoothed using a moving average filter 30 encoder counts (nominally  $2.6^\circ$ ) wide and interpolated to create a look-up table of corrected angles. The accuracy of the resulting look-up tables was evaluated during the point-localization accuracy experiment, described in Section 2.2.2.3

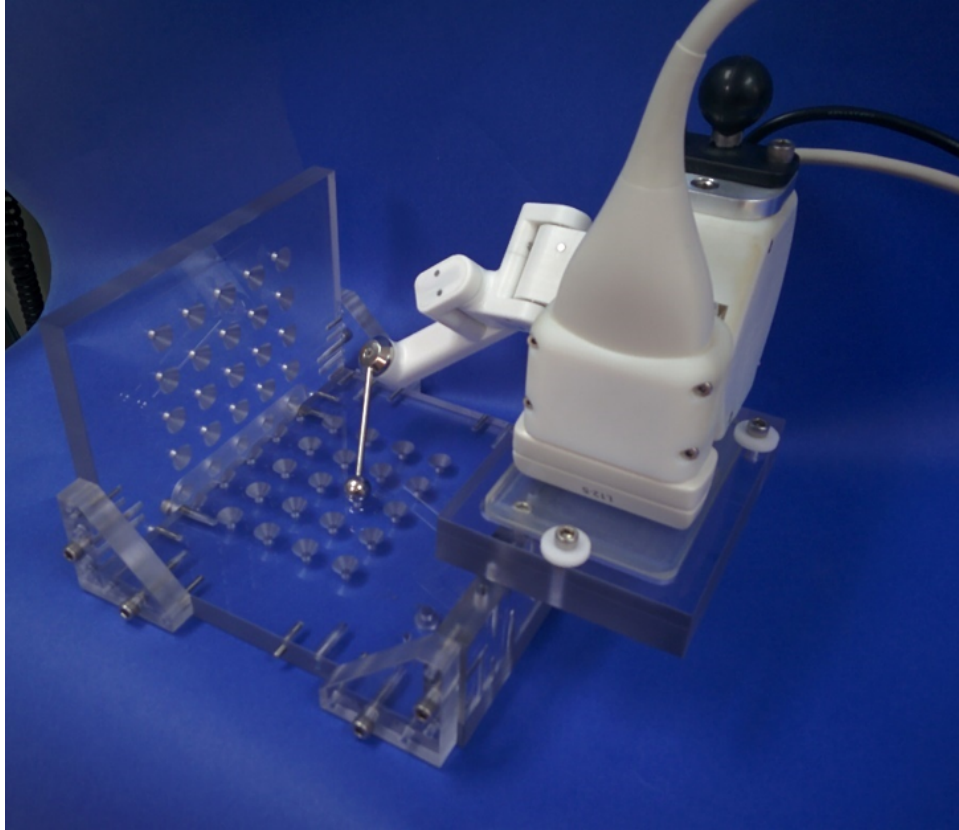


Figure 2.5: Guidance system positioned in tracking arm calibration jig. Jig contained 45 fiducial divots arranged in a  $9 \times 5$  grid pattern separated by 2 cm in each direction. Mounting position of scanner adjusted forward/back and left/right in 3 cm increments, so that 180 ( $45 \times 4$ ) known positions are available for calibration/validation.

below, by comparing the point measurement error with the correction tables implemented to errors with the naïve encoder interpretation.

### 2.2.2.3 Tracking Arm Point Accuracy

With the encoders calibrated for angular accuracy, the next step in the flow of information (Figure 2.3, experiment 3) was using those angles to determine arm position. Point measurement accuracy of the arm was assessed using a machined test jig with 45 fiducial divots placed at known positions on two planes (Figure 2.5). The divots were regularly spaced on a grid with 2 cm separation of 9 rows and 5 columns: 4 rows on the horizontal plane, 4 rows on the vertical plane, and one row at the intersection of the two. The scanner and attached arm were mounted to the jig by the scanner's TPX™ plate, with the plate parallel to the horizontal plane at a 7.5 cm elevation. This configuration placed the divots approximately where a needle template would be placed relative to the scanner during a procedure.

Additionally, the mounting position of the scanner was adjusted to four positions on the jig, forward/back and left/right, separated by 3 cm in each direction. The 3 cm difference in mounting positions and 2 cm divot spacing ensured that divot positions relative to the scanner were unique for each mounting position, creating 180 locations for testing from the 45 physical points. Of the 45 physical points, 15 were used for calibration and 30 for validation, with all fiducial points measured three times per mounting position. Calibration was performed by solving for the location of each measured point in the arm CS (Figure 2.2b) based on measured encoder values. Points in the arm CS were rigidly registered to a reference point cloud in the scanner CS, describing the known positions on the jig, by landmark registration. Forward kinematics of the arm requires the encoder measurements at which the 2nd and 3rd arm segments are parallel to the 1st segment, referred to as the ‘zero-points’, to be known. Zero-points of the 2nd and 3rd encoders were found by minimizing the root mean squared error (RMSE) of the transformed calibration points using an exhaustive search strategy in the region around an initial approximation ( $\pm 40$  encoder counts, nominally  $\pm 3.5^\circ$ ; search resolution of 1 encoder count) and fiducial registration error (FRE) [30] of the resulting registration was reported. Selection of a zero-point for the 1st encoder was not optimized as it corresponds to a DoF in the arm to scanner registration and thus does not affect measurement accuracy.

With the arm calibrated, its zero-points and registration to the scanner were then used to determine the measured position of the validation points and compare them to their known positions. Results of the validation were assessed by calculating the target registration error (TRE) [30] of the validation points and assessed for bias by reporting 95 % confidence intervals on the mean error components in each axis of the arm CS.

#### 2.2.2.4 Image to Scanner Registration

Scanner and imaging CSs were registered by imaging intersections of a string phantom mounted in a known position relative to the scanner (Figure 2.3, experiment 4). The phantom consists of three layers of strings with 1 cm axial separation. Each layer consists of four strings arranged to form a 2 cm by 2 cm square, with subsequent layers offset  $\pm 1$  cm in both axes parallel to the layer to avoid shadowing the layers below. Of the 12 intersection points, six were chosen as fiducials, consisting of two opposing corners of each layer, alternating in position between layers, with the remaining six used as targets. The phantom was immersed in the aforementioned isopropyl alcohol solution and scanned at each of the six depth settings described (Section 2.2.2.1).

To minimize localization error, intersection points were found by modelling each string as a line in 3D space and solving for their least squares intersections. To develop the 3D line models, 3D Slicer [29] was used to resample the image at 2.5 mm intervals along the

length of the string and points were manually placed in all planes where the string was clearly visible. A 3D line of best fit through these points along each string, and their corresponding intersections, was then calculated using MATLAB R2016a (MathWorks, Natick, USA). Rigid registration between the scanner and image CSs was computed by landmark registration. Following registration, scanner-to-image transformations were separated into translation vectors and rotation angles about the axes of the scanner CS and both FRE and TRE were calculated.

#### 2.2.2.5 Template Localization Accuracy

With the tracking arm calibrated and registered to the image, the process of registering the needle template using its fiducial divots could be validated (Figure 2.3, experiment 5). A test jig was constructed in which the scanner and needle template were mounted in known locations. The needle template was localized first using measurements from the localizing arm and second from the known position of the fiducial divots on the jig. Error at each fiducial was assessed by comparing their measured and actual locations. Overall error of the resulting registration was assessed by determining the rigid rotation and translation describing the registration error ( $T_{Error}$ ), defined as,

$$T_{Error} = (T_{Actual})^{-1} \times T_{Measured} \quad (2.1)$$

where  $T_{Measured}$  is the measured transform between template and scanner CSs and  $T_{Actual}$  is the ground truth transform based on the geometry of the test jig.  $T_{Error}$  was then separated into a translation vector and rotation angles in each axis. Registration was repeated for five sets of template measurements with the template remaining in the same position for all five.

#### 2.2.2.6 Needle Insertion Accuracy

With the 3D US scanner and template tracking arm calibrated and registered, its overall targeting accuracy could be assessed by measuring agreement between the two sub-systems. The needle template was registered and needles inserted to a known depth through the template into a bath of isopropyl alcohol solution (described in Section 2.2.2.1) before being scanned. Needle positioning error was found by comparing the needle trajectory and tip position in the 3D US image with that expected from template tracking and insertion depth.

In order to image the inserted needles, the scanner was positioned such that its imaging surface was submerged while the motor housing was not (Figure 2.6). A cylindrical plastic sleeve was placed over the tracking arm to prevent damage in case of accidental





Figure 2.6: Experimental set-up for needle insertion through a tracked template. A collar affixed to the needle allows for a known insertion depth into a bath of isopropyl alcohol and water. Comparison of needle position in tracking and imaging quantifies tracking accuracy. Tracking arm has been bagged to prevent damage if immersed.

immersion. Insertion depth was controlled by fixing collars to the needles to create a physical stop at the surface of the template. Collar position was measured with callipers prior to insertion and averaged over three repeated measurements.

Tracked needle insertion was repeated at four needle insertion depths and five template positions. Template positions were chosen to define the four corners of a rectangle 50 mm wide and 30 mm tall centred on the needle template. The width and height of this rectangle were chosen by examining ten PBSI radiation treatment plans and finding the mean dimensions of the planned needle positions, rounded up to the nearest 5 mm increment. The fifth template position was immediately above the centre (fiducial) position of the template. Needle insertion depths were selected as 11, 13, 15 and 17 cm in order to span the range of insertion depths estimated from 25 PBSI patients (planned depth in tissue + needle template thickness; range: 10.8–17.4 cm, median 12.8 cm). For each insertion depth, the template was positioned such that the needle tip was visible within the 3D US image for all five hole positions without adjusting the template or scanner.

Apparent tip positions and trajectories in the 3D images were determined by manually placing one point at the needle tip and another along the needle shaft at the furthest visible position from the tip. Points at the tip and shaft were averaged across three repeated placements per scan each separated by at least 24 hours. Additionally, repeated

needle tip placements were used to calculate fiducial localisation error (FLE) [30].

#### 2.2.2.7 Phantom Procedure

An agar phantom with a mock-seroma matching patient contours was created and needles delivered according to the corresponding treatment plan using the developed system, with needle placement accuracy evaluated using micro-CT.

An agar mock-seroma was created using a 3D printed mould as in Section 2.2.2.1, with the mould matching CT visible seroma contours, and the above-described agar mixture without a scattering agent was enriched with 0.5% by mass tungsten powder, a formula previously validated for speed of sound [31], to provide contrast in CT. Using a small (5 cm × 4 cm × 4 cm) rectangular container, four 1 cm layers of hyper-echoic and CT hypo-intense agar were poured and the hypo-echoic, CT hyper-intense mock-seroma embedded inside. At each layer, four metal ball-bearings 1 mm in diameter were placed at the perimeter of the container, alternating between a box-corners and “+” shaped pattern, creating 16 CT visible fiducials embedded in a “bounding box” around the mock-seroma. The bounding box was then embedded inside a phantom breast using a bowl approximately 12 cm in diameter as a mould. Due to the relatively stiff mechanical properties of agar, the mould was designed to provide a flat surface at the top of the breast for imaging. An additional fiducial marker was placed at the outer edge of the phantom breast to ensure fiducial asymmetry. The phantom breast was then placed on top of a block of agar 30 mm thick with a 10 mm deep recess matching the diameter of the breast phantom to hold the breast phantom stationary. The block and phantom were then placed on top of a plastic platform designed to fit in the bore of a micro-CT scanner. An adjustable support for the needle template was also mounted to the platform and designed to provide 6 DoF’s while keeping metal components separate from the template.

With the phantom constructed, a micro-CT image (Locus Ultra, General Electric HealthCare, London, Canada) was captured before and after needle delivery at 120 kVp and 20 mA tube current with isotropic 0.154 mm voxels. Prior to implant the mock-seroma was manually contoured in the pre-treatment micro-CT image at 0.154 mm slice separation. The patient treatment plan, consisting of one fiducial needle and 14 seed-bearing needles containing 59 seeds, was registered to the pre-treatment micro-CT using a rigid, surface based registration, the iterative closest point (ICP) algorithm [32], between the patient and phantom seroma contours, defining the phantom treatment plan.

Three-dimensional US images of the phantom were captured with the developed system while stabilized by a counterbalanced mechanical arm and the images manually contoured. The treatment plan was registered from the pre-treatment micro-CT to the

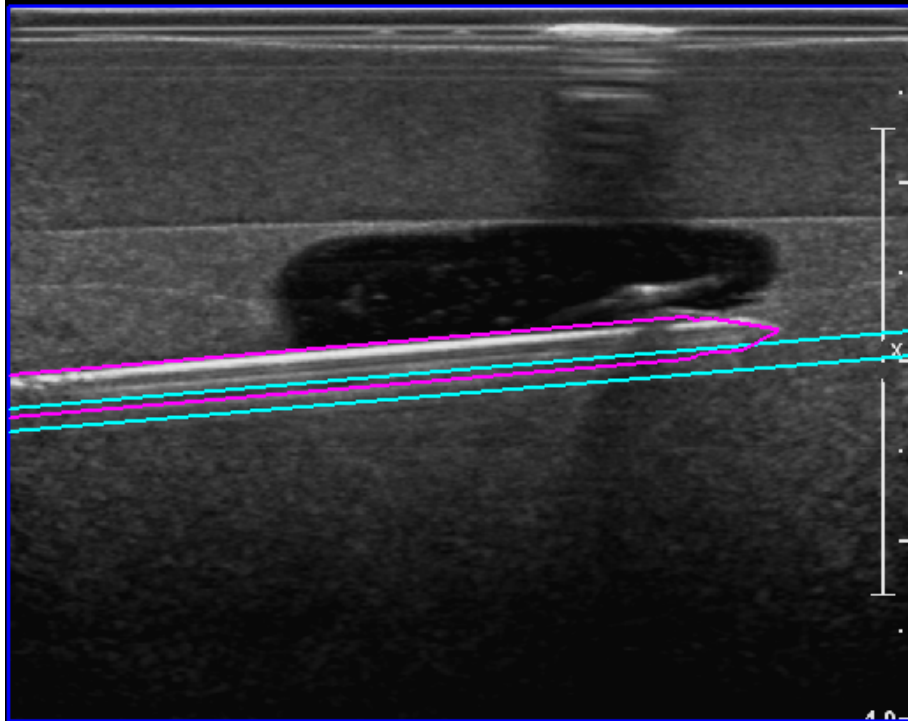


Figure 2.7: Screenshot showing visual overlay of planned needle position (purple) and projected needle trajectory (cyan) on live 2D US image for guidance during needle insertion. Inserted needle is visible in US image beneath purple overlay.

3D US using the ICP algorithm [32] and seroma contours. While the embedded fiducial markers were visible in 3D US, they were not used to guide the procedure. With the phantom treatment plan registered to the intraoperative image, the needle template was registered and its position iteratively adjusted to match the treatment plan. Once the template position was satisfactory, needles were inserted through the needle template according to their positions in the treatment plan starting with the fiducial needle and proceeding from the deepest needles to the most superficial, in keeping with clinical practice. When inserting each needle, the 2D US transducer was moved by the system such that the needle was predicted to intersect with the live image and user-initiated adjustments of the transducer position made as necessary. A visual overlay of the desired needle position was drawn onto the live 2D image (Figure 2.7), providing real-time feedback as the needle was inserted.

A post-implant micro-CT was obtained with all needles present in the phantom. Needle positions were manually identified by placing a point at each needle tip and along each needle shaft. Pre- and post-treatment micro-CT images were registered by manually placing points at the fiducial beads in each image and performing landmark

registration. Of the 16 markers near the seroma, 8 were used as fiducials and 8 as targets to calculate TRE. The 17th asymmetrically placed marker was used only qualitatively to prevent a 'flipped' registration due to the otherwise symmetric arrangement of fiducial markers. In order to quantify FLE, point placement was repeated five times each for the fiducial needle and half (7) of the mock seed-bearing needles as well as for half (8) of the embedded markers in both pre- and post-operative images.

Based on registration between the pre- and post-operative micro-CT images, needle placement error was quantified with respect to tip position and needle trajectory as the difference between observed needle positions and the phantom treatment plan. Additionally, seed positions were extrapolated based on needle positions and the planned seed configuration within the needles to calculate modelled seed placement error assuming no additional error due to dropping seeds.

#### 2.2.2.8 Statistical Methods

Linear distances between strings were tested for normality in each direction and depth setting based on a D'Agostino-Pearson test, using a Bonferroni correction to adjust for multiple (18) tests. Once the data passed (failed) the tests for normality, 95% confidence intervals of the mean (median) measurements were calculated using the one sample Student's t-test (Wilcoxon signed rank test) in GraphPad Prism 7 (GraphPad Software, La Jolla, USA). Ninety-five percent confidence intervals of the differences in seroma phantom volume between segmentation and water-displacement measurements were calculated using a Welch's t-test. The Welch's t-test was chosen over a Student's t-test due to the dissimilar methods of measurement between groups, suggesting their variances may be unequal.

TRE following tracking arm validation with and without encoder maps applied was compared using a paired Student's t-test using MATLAB 2016a (MathWorks, Natick, USA). For both tracking arm point accuracy and needle insertion accuracy validation, 95% confidence intervals on the mean error in each axis were calculated using a one-sample Student's t-test using MATLAB 2016a (MathWorks, Natick, USA) and a 95% prediction ellipsoid, an ellipsoidal volume centred on the sample mean such that any future observation is expected to have a 95% probability of falling within the ellipsoid, was calculated using principle component analysis.

## 2.3 Results

### 2.3.1 Three-Dimensional Image Reconstruction

Of the 18 sets of linear distance measurements, 4 failed the Bonferroni corrected tests of normality ( $p < 0.05/18$ ). Median values across all directions and depth settings were

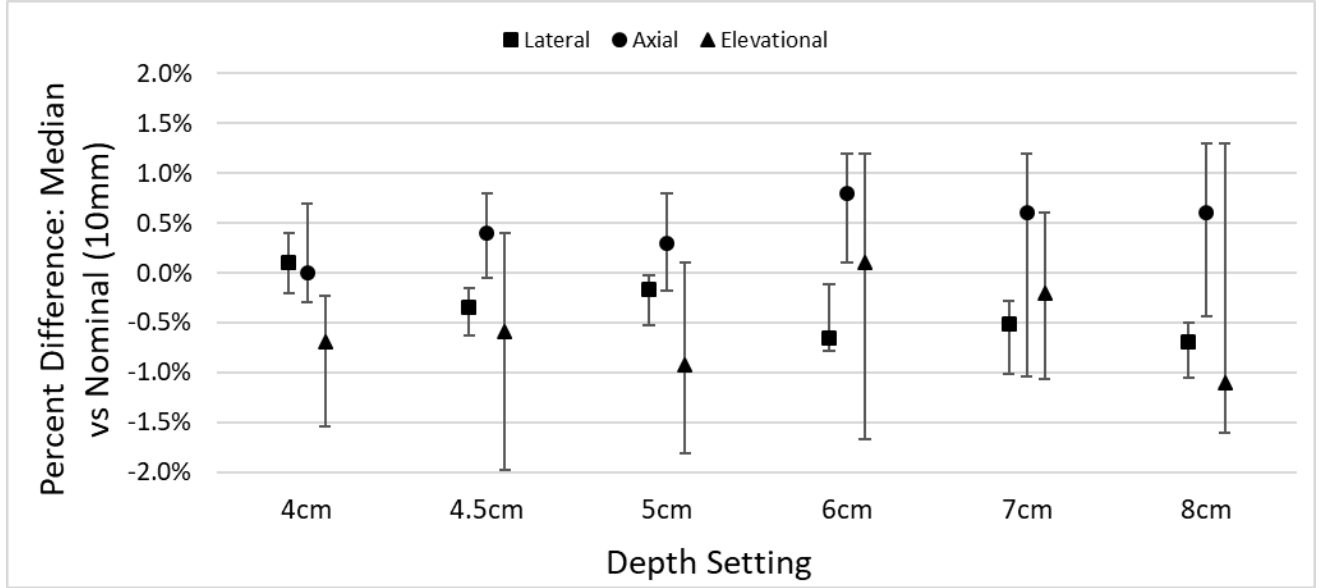


Figure 2.8: Results of linear measurement validation using a 3D grid phantom immersed in 7.25 % by volume isopropyl alcohol solution. Columns and error bars show medians and 95 % confidence intervals, respectively. N=40 per direction, per depth setting.

Table 2.1: Results of volumetric validation comparing segmented volume in 3D US to water displacement volume. 95 % confidence intervals calculated using a Welch 's t-test.

Phantom	3D US (cm <sup>3</sup> )		Water Displacement (cm <sup>3</sup> )		Difference (cm <sup>3</sup> )	
	Mean	St. Dev.	Mean	St. Dev.	Mean	95 % CI
Seroma 1	5.73	0.04	5.57	0.14	0.16	[-0.06, 0.37]
Seroma 2	3.75	0.03	3.61	0.13	0.15	[-0.08, 0.37]

within  $\pm 1.1\%$  (0.11 mm) of nominal and 95 % confidence intervals of the median were within  $\pm 2.0\%$  (0.20 mm), as shown in Figure 2.8.

Volumetric measurements of the seroma-shaped phantoms showed mean segmentation volumes 2.8 % greater than water displacement for the smaller seroma ( $3.75 \pm 0.03$  cm<sup>3</sup> vs  $3.61 \pm 0.13$  cm<sup>3</sup>) and 4.1 % greater for the larger seroma ( $5.73 \pm 0.04$  cm<sup>3</sup> vs  $5.57 \pm 0.14$  cm<sup>3</sup>) (Table 2.1). Neither difference was found to be statistically significant (both  $p = 0.06$ ).

Breast 3D US images captured from a healthy volunteer (Figure 2.9) showed image quality comparable to clinically used 2D US images, as assessed by the ultrasonographer who captured them. Images showed no evidence of artefacts due to excessive scanner or tissue motion and there was little to no evidence of shadowing artefacts due to inadequate

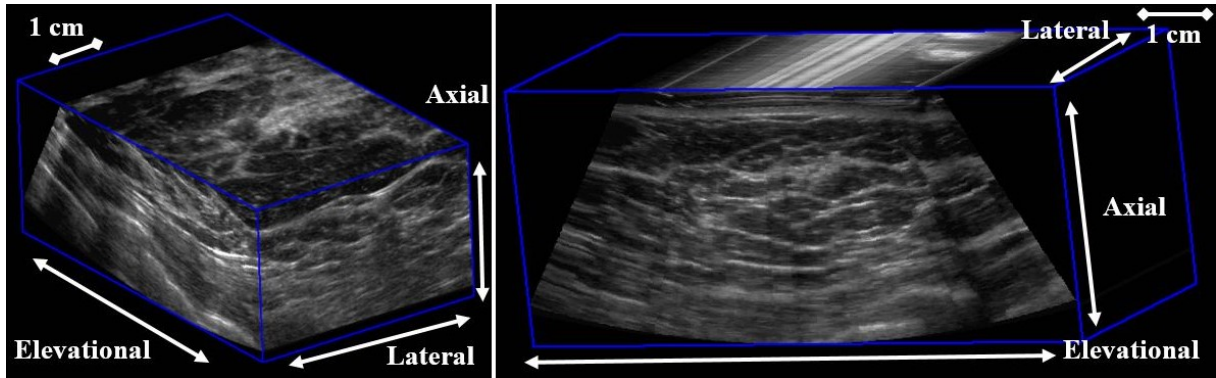


Figure 2.9: Multi-planar views of a 3D US image captured from a healthy volunteer using developed system. Left: View showing representative slices of image along orthogonal planes. Arrows and labels indicate principal axes. Right: View illustrating geometry of reconstructed scans. Field of view visible in axial-elevational plane is constant across lateral axis.

coupling at either surface of the TPX<sup>TM</sup> plate.

### 2.3.2 Encoder Mapping

Encoder error mapping was performed for the entire range of motion of all three encoders and the resulting error maps shown in Figure 2.10. Mean angular spacing between measurement points was  $1.1^\circ$  (SD  $0.13^\circ$ ).

Adjacent mounting positions across all encoders had a minimum overlap region of 182 encoder counts (nominally  $16^\circ$ ) and, after alignment, had a residual RMSE of  $<0.06^\circ$  (nominally 0.7 encoder counts). In the plotted error maps (Figure 2.10), positive (negative) slopes in the integral error indicate an over- (under-) estimation of the angle between two positions, while the first position within the encoder’s range of motion is arbitrarily chosen as the point from which the integral begins.

### 2.3.3 Tracking Arm Point Accuracy

Optimization of the zero-points of the encoders yielded offsets within 10 encoder counts (nominally,  $0.88^\circ$ ) of the manually estimated values. RMSE over the range of offsets searched showed a smooth, convex surface with a single global minimum of 0.47 mm, corresponding to an FRE of 0.47 mm. With the optimized offsets and registration chosen, TRE of the remaining validation points was 0.43 mm (SD 0.19 mm), with a histogram of the magnitude of target errors shown in Figure 2.11.

The above process of registration and accuracy validation was conducted using the encoder maps described in Figure 2.10. When repeated with the naïve encoder interpretation, TRE (FRE) worsened, from  $0.43 \pm 0.19$  mm ( $0.43 \pm 0.18$  mm) to  $0.57 \pm 0.29$  mm ( $0.59 \pm 0.26$  mm).

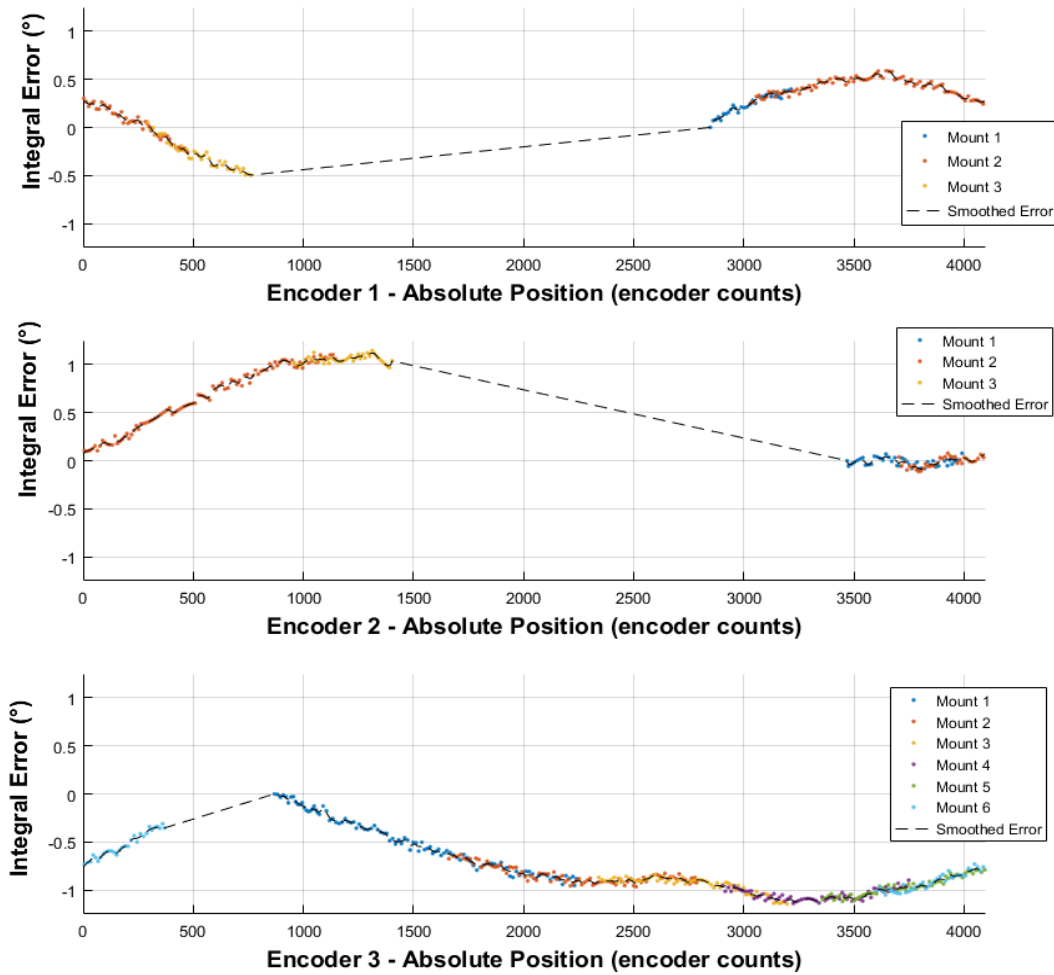


Figure 2.10: Integral error of each encoder in the tracking arm as a function of absolute position when calibrated. Each encoder was calibrated using multiple mounting positions in order to span the full range of motion. Dashed black line indicates the estimated integral encoder error after smoothing. All plots show integral error over  $360^\circ$  range (0–4095 encoder counts).

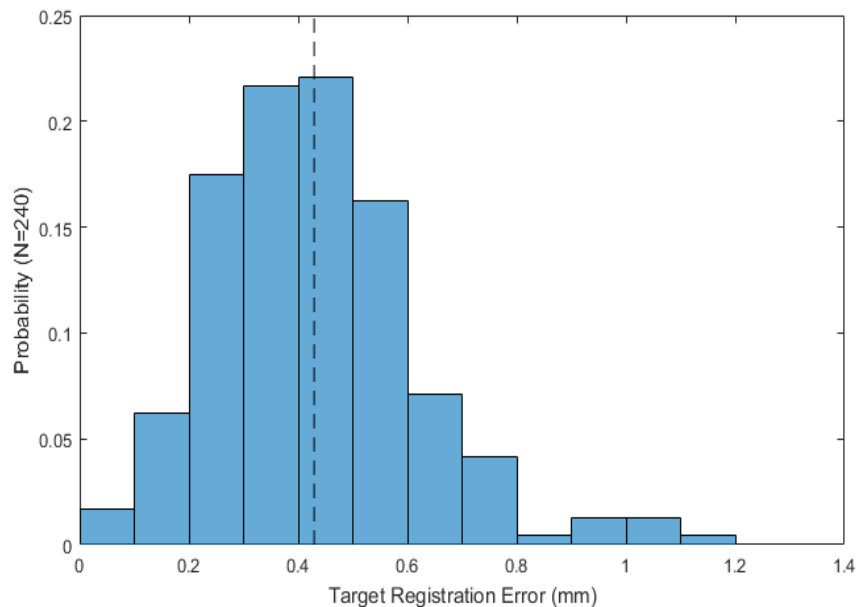


Figure 2.11: Normalized histogram of target registration error (TRE) observed during tracking arm validation plotted with respect to probability (N=240). Dashed black line indicates mean TRE (0.43 mm).

TRE using the corrected and naïve encoder interpretations were statistically significantly different ( $p < 0.05$ ).

To evaluate directional trends in the observed errors, 95 % confidence intervals of the mean error in each axis were calculated in the arm CS and all intervals found to be within  $\pm 0.07$  mm as shown in Table 2.2. While two of the three axes (X and Z) were statistically significantly different ( $p < 0.05$ ), the small magnitude of the differences ( $< 0.05$  mm) suggest the biases are not clinically relevant.

The 95 % prediction ellipsoid of the validation error, shown in Figure 2.12, has its

Table 2.2: Confidence intervals on the mean error in each axis following tracking arm point accuracy validation. Error evaluated in the arm coordinate system (Figure 2.2b).

Axis	Error (mm)	
	Mean	95 % CI
X (Perpendicular to base of arm)	-0.03	[-0.05, 0.00]
Y (Left/Right with respect to base of arm)	-0.01	[-0.03, 0.06]
Z (Up/Down with respect to base of arm)	0.04	[0.00, 0.07]



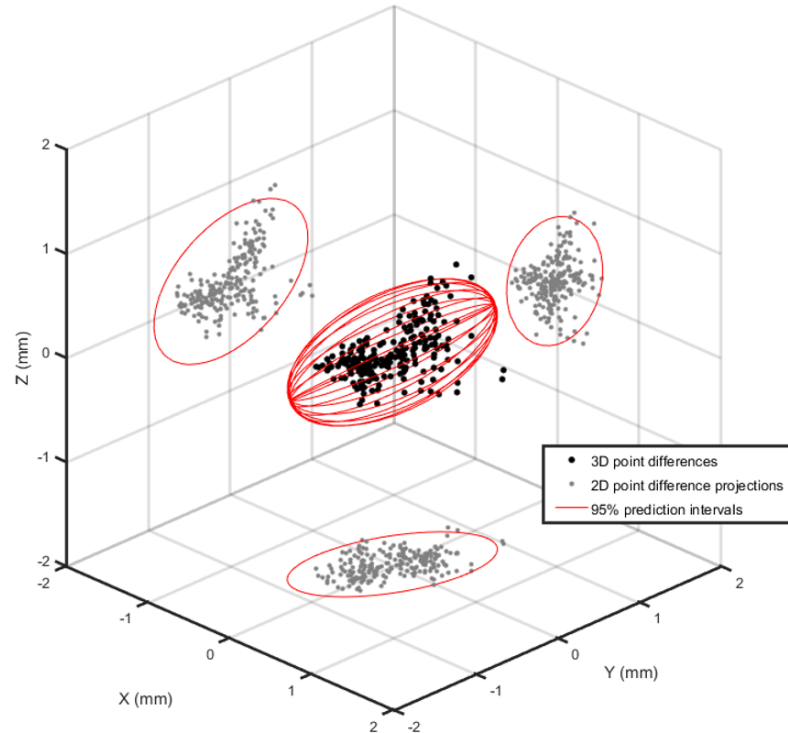


Figure 2.12: 95 % prediction ellipsoid of arm validation error plotted with respect to the arm coordinate system (units: mm). Black dots indicate individual point measurement errors and red lines indicate boundaries of 95 % confidence ellipsoids. Gray dots and adjacent ellipses indicate projections of the above onto canonical planes. See Figure 2.2b for coordinate system description.

direction of largest variance close to the Y axis (angle between  $27^\circ$ ), with a 95 % prediction interval along that direction of  $\pm 1.0$  mm.

### 2.3.4 Image to Scanner Registration

Across all depth settings studied, 3D line models used a mean of 17 points per string (range: 8–21) and resulted in TRE of  $\leq 0.87$  mm across all depth settings (FRE  $\leq 0.37$  mm). TRE and FRE for each depth setting are shown in Table 2.3.

As discussed in Section 2.2.1.2, the scanner and image CSs are nearly coincident. Translations in the X and Y axis of the scanner CS (Figure 2.2b) were  $< 0.2$  mm in magnitude for all depth settings but had a positive translation of 1.8–2.4 mm in the Z axis, the elevational axis of the scan. Similarly, rotation angles in the Y and Z axes were  $< 0.6^\circ$ . However, the X-axis, which is parallel with the rotation axis of the tilting portion of the US transducer’s hybrid motion, had a positive rotation of 1.4–2.4 $^\circ$ .

Table 2.3: Target and fiducial registration error (TRE and FRE) of registering the scanner and image coordinate systems using a phantom with 12 string intersections (6 fiducials, 6 targets).

Depth Setting (cm)	TRE (mm)	FRE (mm)
4.0	0.65	0.26
4.5	0.70	0.26
5.0	0.49	0.19
6.0	0.57	0.21
7.0	0.87	0.37
8.0	0.62	0.25

Table 2.4: Mean (SD) of components of template localization errors. Rotations and translations expressed with respect to the scanner coordinate system (Figure 2.2b). Positive angles indicate clock-wise rotation about an axis when viewed from the origin.

Rotation Angles ( $^{\circ}$ )			Translational Components (mm)		
X	Y	Z	X	Y	Z
0.6 (<0.1)	0.0 (0.1)	1.0 (<0.1)	-0.50 (0.06)	1.25 (0.11)	0.66 (0.10)

### 2.3.5 Template Localization Accuracy

Measurements of individual fiducials on the template showed strong reproducibility, with a mean deviation distance between repeated measurements of 0.13 mm (maximum 0.37 mm). However, the mean distance between measured and ground truth locations for each point was 1.56 mm (range 1.17–1.82 mm). With respect to the accuracy of the overall template registration, error transforms as defined in Equation 2.1 showed mean rotation angles in each axis of  $<1^{\circ}$  (Table 2.4). Translational components were  $\leq 1.25$  mm in each axis with the largest transformation in the Y axis, indicating that the template was measured to be lower (further from the scanner) than expected.

### 2.3.6 Needle Insertion Accuracy

Mean ( $\pm$  SD) needle tip error across all depth settings was  $2.46 \pm 0.88$  mm, with errors at each insertion depth shown in Table 2.5. At the smallest insertion depth tested (11 cm), template positions were limited by an inability to submerge the tracking arm encoders, a constraint not relevant to patient procedures. As a result, only 6–8 mm of the needles at this insertion depth were visible in the 3D US image compared with  $>20$  mm for all other depths, making needle trajectories more susceptible to localization error and

Table 2.5: Magnitude of needle tip and trajectory error when comparing expected needle position from tracking and insertion depth to observed needle position in 3D US.

Needle Insertion Depth (cm)	Magnitude of Needle Tip Error (mean $\pm$ SD) (mm)	Magnitude of Needle Trajectory Error (mean $\pm$ SD) (degrees)
11	2.16 $\pm$ 0.46	3.1 $\pm$ 2.3 <sup>a</sup>
13	1.60 $\pm$ 0.74	1.2 $\pm$ 1.0
15	3.15 $\pm$ 0.71	1.1 $\pm$ 0.3
17	2.92 $\pm$ 0.64	0.8 $\pm$ 0.4
All	2.46 $\pm$ 0.87	1.6 $\pm$ 1.5 <sup>a</sup>
All (Excluding 11 cm)	-	1.0 $\pm$ 0.6

<sup>a</sup>Visible length of needle at 11 cm insertion depth was short ( $\leq 8$  mm), leading to increased error in measuring trajectory. As a result, mean trajectory error is also reported with this depth excluded.

resulting in a mean trajectory error of  $3.1 \pm 2.3^\circ$  compared to means of  $\leq 1.2^\circ$  for all other depths. For this reason, trajectory errors are also reported with this insertion depth excluded, yielding a mean trajectory error of  $1.0 \pm 0.6^\circ$ . FLE of the needle tips in 3D US was found to be 0.26 mm.

As in Section 2.3.3, directional trends in the observed errors were assessed using 95 % confidence intervals on the error in each axis and by calculating 95 % prediction ellipsoids (Figure 2.13). Statistically significant biases were found in all three axes of the image CS, with the largest biases approximately 1.5 mm in both the elevational and axial directions. In the axial direction, there was a bias of  $-1.44$  mm, indicating that the needle appears in imaging to be closer to the scanner than expected. This upward bias may result from a combination of a stronger visibility of the top surface of the needle in the 3D US image and relatively large blurring effect as a result of the sharp boundary between the needle and surrounding fluid. Additionally, there was a bias of  $+1.50$  mm in the elevational direction, indicating that the needle tip appeared closer to the scanner's motor housing than predicted. The bias in the lateral axis, approximately corresponding with the needle insertion direction, was smaller at  $+0.51$  mm, indicating that the needle tip appeared further from the needle template than expected.

The 95 % prediction ellipsoid of the needle insertion error shown in Figure 2.13, has its direction of largest variance close to the elevational axis (angle between  $23^\circ$ ). The size of the 95 % prediction ellipsoid along this direction is  $\pm 3.52$  mm.

Table 2.6: Confidence intervals on the mean error in each axis following needle insertion accuracy validation. Error evaluated in the imaging coordinate system (Figure 2.2b) and averaged across all needle insertion depths.

Axis	Error (mm)	
	Mean	95 % CI
Lateral	0.51	[0.26, 0.77]
Axial	-1.44	[-1.80, -1.08]
Elevational	1.5	[0.95, 2.06]

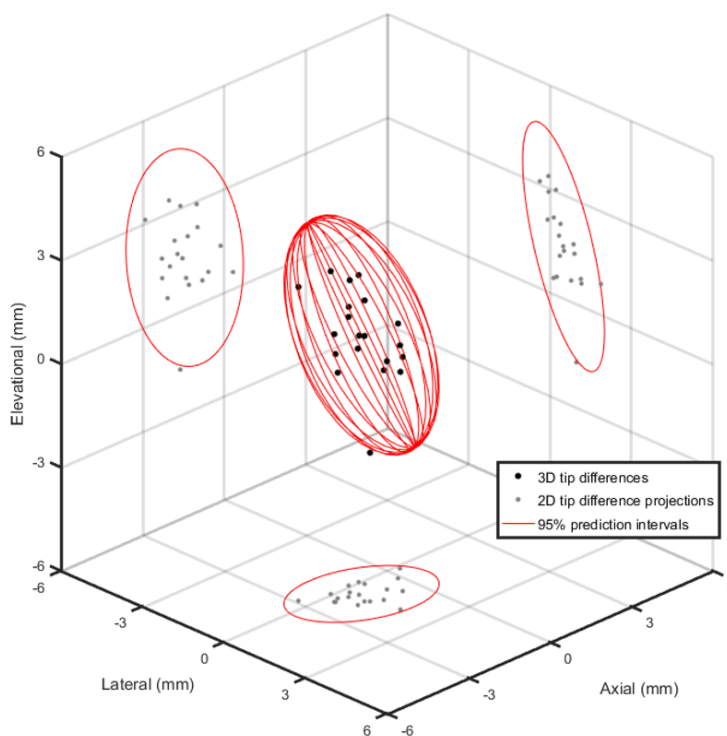


Figure 2.13: Ninety-five percent prediction ellipsoid of needle placement error plotted with respect to the image coordinate system. Black dots indicate individual point measurement errors and red lines indicate boundaries of 95 % confidence ellipsoids. Gray dots and adjacent red ellipsoids indicate projections of the above onto canonical planes. See Figure 2.2b for coordinate system description.

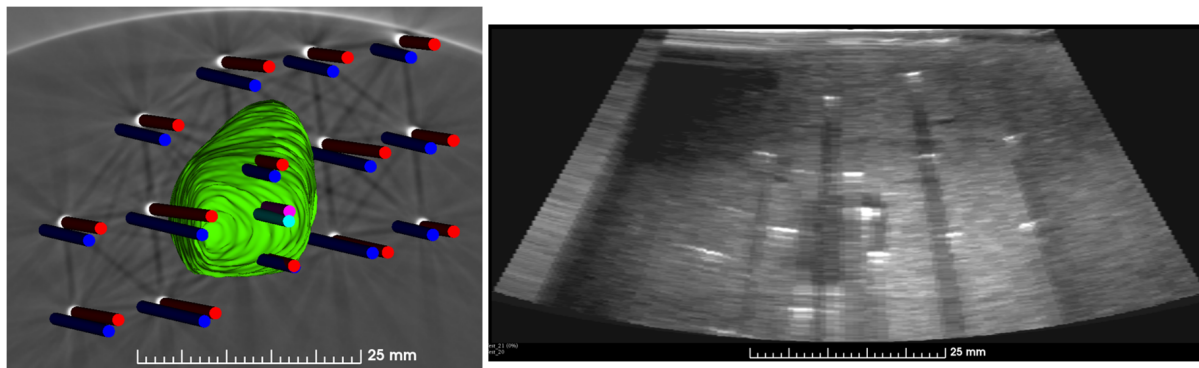


Figure 2.14: Post-operative images of phantom procedure. a) Visualization of planned and observed needle positions overlaid on post-op micro-CT. Planned seed-bearing (fiducial) needles shown in blue (cyan) with observed needles shown in red (pink). Pre-op seroma following registration to post-op micro-CT shown in green. b) Reconstructed plane of 3D US with seroma and all 15 needles visible.

### 2.3.7 Phantom Procedure

Mean ( $\pm$  SD) needle tip and trajectory error was found to be  $2.08 \pm 0.73$  mm and  $2.6 \pm 0.3^\circ$ , respectively, with planned and observed positions visualized in Figure 2.14. Needles in the post-op micro-CT appeared straight, with no signs of bending. Modelled seed positions showed mean ( $\pm$  SD) seed error of  $2.50 \pm 0.67$  mm with a maximum error of 3.67 mm. TRE (FRE) between pre- and post-op micro-CT images was found to be 0.18 mm (0.18 mm), while FLE for implanted markers and needle tips was 0.06 mm and 0.15 mm, respectively.

Errors in observed needle tips and trajectories showed a systematic shift. In the planned template CS, needle tip errors had statistically significant biases of 1.84 mm to the left (+Y, template CS) and 0.38 mm down (-Z, template CS). Similarly, the azimuth and elevation angles of observed needle trajectory errors were both significantly different from 0, with a mean orientation error of  $1.5^\circ$  azimuth (towards template left) and  $2.1^\circ$  elevation (towards template up).

## 2.4 Discussion

### 2.4.1 Three-Dimensional Image Reconstruction

Median linear measurement errors were within  $\pm 1.1\%$ , comparable to the 0.1–3.0% observed in previous 3D US systems [16, 33, 34], while absolute volume differences of 0.15–0.16 cm<sup>3</sup> were comparable or better. However, the relative volume difference of 2.8–4.1% was higher than those observed in similar systems, likely due to the small

volumes measured (4–6 cm<sup>3</sup> vs 1–288 cm<sup>3</sup>). Positive feedback on volunteer image quality indicated acceptable ultrasound coupling between the TPX™ plate and breast while mitigating motion artifacts.

### 2.4.2 Encoder Mapping

Encoder error mapping significantly improved the tracking arm’s point accuracy by 25 % (0.43 mm vs 0.57 mm). Overlapping regions of calibration from neighboring mounting positions showed consistent slopes and resulting RMSE of overlapping errors was within noise-level (nominally 0.7 encoder counts), suggesting that a portion of the encoder error observed was repeatable and the methodology of empirically aligning neighboring regions is sound.

### 2.4.3 Tracking Arm Point Accuracy

Tracking arm point error of 0.43 mm is comparable with errors of optical and electromagnetic (EM) systems, while mitigating their environmental susceptibilities, namely line of sight obstruction and magnetic field distortion, respectively. A recent review of EM tracking in medicine described errors of 0.25–1.19 mm and 0.26–7.59 mm in undistorted and distorted environments, respectively [35], suggesting presently reported errors are comparable to EM tracking in the undistorted case and potentially superior in the distorted case. Optical tracking has been shown to be accurate to within 0.25–0.35 mm [36], only marginally better than present values. While the mechanical approach presented is still susceptible to obstructions in its “line-of-reach,” its proximity to the needle template ( $\leq 16$  cm) mitigates the burden of this constraint. Although the mechanical tracking arm is limited to intermittent measurements of unmoving tools in a relatively small tracking volume, these limitations are thought to be an acceptable compromise for improved simplicity, cost and environmental sensitivity when localizing a single tool that remains fixed the majority of the procedure.

In addition to error magnitude, biases present are negligible for the purposes of brachytherapy guidance. Ninety-five percent confidence intervals of the mean error in each axis are within  $\pm 0.1$  mm. The statistically significant differences in X and Z (arm CS, Figure 2.2b) of 0.03 mm and 0.04 mm, respectively, are of little practical consequence. With respect to directionality, the largest direction of error (long axis of the 95 % prediction ellipsoid, (2.12) was close to the Y-axis of the arm (Figure 2.2b). The effect of angular uncertainty at a given position is proportional to the distance between the joint axis and the tip of the arm, causing angular error at the first joint to have the largest effect on joint position. When the first joint is centred, the derivative of tip position with respect to the first joint angle is along the Y axis, possibly explaining the large error

close to that axis.

#### 2.4.4 Image to Scanner Registration

During registration of the 3D US image to the scanner, TRE was  $<1$  mm for all depth settings, with no clear trends at changing depth. The nylon strings created blurring artifacts of a size not seen in phantom/patient images and the resulting visualization uncertainties likely account for much of the observed error.

The observed rotation about the lateral axis and translation in the elevational axis are consistent with image shift due to mechanical backlash in the hybrid motion of the 3D scan. Backlash in the gears of the scanner's drive-train create a small dead-space when the transducer motion changes directions, rotating the image about the tilt axis of the hybrid geometry and bringing the 3D image towards the scanner's motor housing.

#### 2.4.5 Template Localization Accuracy

Registration of the template to the scanner was achieved with angular errors of  $<1^\circ$  and translational errors of  $\leq 1.25$  mm. The observed bias in the Y axis, causing the template to appear 1.25 mm lower than expected, was consistent with the bias observed in Section 2.3.6, with needles appearing 1.5 mm higher than expected, potentially indicating error in the registration of the tracking arm to the scanner. During registration of the tracking arm to the scanner (Section 2.2.2.3), both calibration and validation of point measurement accuracy were performed on the same jig, potentially leading to unnoticed errors in the position of the scanner relative to the jig. However, other sources of error when evaluating needle insertion accuracy and the use of a single template position in the template localization accuracy suggest further investigation may be warranted.

#### 2.4.6 Needle Insertion Accuracy

The average ( $\pm$ SD) needle tip error was  $2.46 \pm 0.87$  mm, within the dosimetric benchmark of 5 mm for the smallest  $^{103}\text{Pd}$  seed error that would significantly affect dose distribution [37]. The axes of largest variance and bias, respectively, were both near or along the elevational axis which, as the reconstructed axis, had the worst resolution. The elevational axis was also the axis along which the 3D image most deviated from its expected position, as discussed in Section 2.4.4. Additionally, although 20 needles were assessed, they represented only four needle template registrations, for which template registration error will be the same. As a result, directional biases may be exaggerated by the compromised independence of multiple needle observations taken from the same template registrations.

### 2.4.7 Phantom Procedure

The needles of a PBSI patient treatment plan were successfully delivered to a phantom with mean ( $\pm$  SD) seed error of  $2.50 \pm 0.67$  mm and a maximum error of 3.67 mm, meeting established dosimetric benchmarks ( $<5$  mm) [37]. Although the magnitude of the errors observed was acceptable, a systematic shift was observed. The systematic errors in needle positioning were likely a result of positioning error at the needle template that is propagated to all needles.

Mean needle tip error remained similar to needle insertion accuracy (Section 2.3.6; 2.46 mm vs 2.08 mm) while phantom trajectory error more than doubled ( $1.0^\circ$  vs  $2.6^\circ$ ). The increased trajectory error is thought to be due to errors in manually positioning the orientation of the template. The adjustable template support was designed to fit inside the micro-CT bore. As a result, rotational DoF's have their axis of rotation at a distance of 5–10 cm from their parallel axes in the template CS, creating a levered effect that made fine rotations difficult. These constraints would not be present during patient procedures, making a more easily adjusted template support feasible. The presented phantom procedure used an “open-loop” approach to position the needle template, relying only on information provided by the tracking sub-system. Alternatively, a “closed-loop” approach could be adopted using feedback from the first inserted needle to refine the needle template position and re-insert if necessary, potentially reducing needle placement error further.

A limitation of this phantom study was that seed positions were extrapolated from needle positions assuming no additional error due to seed deposition. While errors due to seed dropping have not been explicitly evaluated in the context of PBSI, needle drag in permanent seed prostate brachytherapy has been partially implicated as a source of a systematic bias across patients. A study of seed placement error by Morton et al. reported no analog to that bias for PBSI procedures [8].

The results of this study should be interpreted in the context of a phantom with limitations to its fidelity, such as differing mechanical properties, lack of breathing motion and lack of pre- to intra-operative seroma shift or deformation that may occur in clinical implants. In particular, rigid registration between manual segmentations of the pre- and intra-operative seroma would likely be inadequate in a clinical context, suggesting development of semi-automatic segmentation and deformable registration techniques are warranted. Additionally, modelled seed error represents an optimistic estimate of implant accuracy, potentially subject to additional displacements from the seed dropping process.

To our knowledge, this is the first report of a patient or phantom PBSI procedure guided with intraprocedural 3D imaging. Three-dimensional visualization of the seroma



intraoperatively combined with needle template registration is hypothesized to decrease uncertainty in PBSI guidance and may result in improved seed placement accuracy and reduced operator dependence of the procedure. Historical experience with high dose-rate breast brachytherapy techniques suggests operator dependence will be an important factor in adoption of this procedure, having previously impeded the adoption of interstitial approaches [38] while catapulting the development and adoption of less demanding intracavitary techniques [4]. Future work includes refinement of the system for improved template tracking accuracy, non-interventional patient use to collect data for segmentation and registration development, and a comparison with current practice in phantoms.

## 2.5 Conclusions

A 3D US guidance system for PBSI has been developed with suitable benchtop performance and image quality in volunteer scans. An integrated template tracking arm showed point measurement error of  $0.43 \pm 0.19$  mm and, in combination with a trackable template, allowed for tip position and trajectory to be predicted to within  $2.46 \pm 0.88$  mm and  $1.6 \pm 1.5^\circ$ . A phantom PBSI procedure was successfully delivered using the system, to our knowledge the first delivered using intraoperative 3D imaging, with a mean and maximum modelled seed error of  $2.50 \pm 0.67$  mm and 3.67 mm, respectively. Translation into the clinic is forthcoming, with the ultimate goal of increasing access to BCT by making PBSI easier for physicians to adopt.

# References

- [1] Sharad Goyal, Sheenu Chandwani, Bruce G Haffty, and Kitaw Demissie. Effect of travel distance and time to radiotherapy on likelihood of receiving mastectomy. *Annals of Surgical Oncology*, 22(4):1095–101, April 2015.
- [2] Jean-Philippe Pignol, Jean-Michel Caudrelier, Juanita Crook, et al. Report on the Clinical Outcomes of Permanent Breast Seed Implant for Early-Stage Breast Cancers. *International Journal of Radiation Oncology\*Biology\*Physics*, 93(3):614–621, November 2015.
- [3] Bernard Fisher, Stewart Anderson, John Bryant, et al. Twenty-Year Follow-up of a Randomized Trial Comparing Total Mastectomy, Lumpectomy, and Lumpectomy plus Irradiation for the Treatment of Invasive Breast Cancer. *The New England Journal of Medicine*, 347(16):1233–41, October 2002.
- [4] John A Cox and Todd A Swanson. Current modalities of accelerated partial breast irradiation. *Nature Reviews Clinical Oncology*, 10(6):344–356, April 2013.
- [5] David E. Wazer, Douglas W. Arthur, and Frank A. Vicini, editors. *Accelerated Partial Breast Irradiation*. Springer Berlin Heidelberg, Berlin, Heidelberg, 2nd edition, 2009.
- [6] Frank Vicini, Chirag Shah, Rahul Tendulkar, et al. Accelerated partial breast irradiation: An update on published Level I evidence. *Brachytherapy*, 15(5):607–615, 2016.
- [7] Jean Philippe Pignol, Brian Keller, Eileen Rakovitch, et al. First report of a permanent breast  $^{103}\text{Pd}$  seed implant as adjuvant radiation treatment for early-stage breast cancer. *International Journal of Radiation Oncology\*Biology\*Physics*, 64(1):176–181, 2006.

- [8] Daniel Morton, Michelle Hilts, Deidre Batchelar, and Juanita Crook. Seed Placement in Permanent Breast Seed Implant Brachytherapy: Are Concerns Over Accuracy Valid? *International Journal of Radiation Oncology\*Biography\*Physics*, 95(3):1050–1057, February 2016.
- [9] Jean-Philippe Pignol, Brian M Keller, and Ananth Ravi. Doses to internal organs for various breast radiation techniques - implications on the risk of secondary cancers and cardiomyopathy. *Radiation Oncology*, 6(1):5, January 2011.
- [10] Deidre Batchelar, Michelle Hilts, Marie-Pierre Milette, and Juanita Crook. Starting a Pd-103 Permanent Breast Seed Implant Program: Dosimetric Results for Our First 25 Cases. *Brachytherapy*, 15:S45, May 2016.
- [11] Deidre Batchelar, Michelle Hilts, Tracey Rose, et al. Simulation and Intraoperative Checks for Improved Standardization and Reproducibility of Partial Breast Seed Implant Technique. In *Brachytherapy*, volume 13, page S84, March 2014.
- [12] JP Pignol, B Keller, E Rakovitch, et al. A breast permanent implant (BPI) for partial breast irradiation using 103Pd stranded seeds: A comparison of a ‘free hand’ versus a ‘fiducial needle’ technique. *Radiotherapy and Oncology*, 72:S57, September 2004.
- [13] Ananth Ravi, Curtis B Caldwell, Brian M Keller, Alla Reznik, and Jean-Philippe Pignol. Online gamma-camera imaging of 103Pd seeds (OGIPS) for permanent breast seed implantation. *Physics in Medicine and Biology*, 52(19):5921–32, October 2007.
- [14] Ananth Ravi, Curtis B Caldwell, and Jean-Philippe Pignol. Experimental evaluation of an online gamma-camera imaging of permanent seed implantation (OGIPSI) prototype for partial breast irradiation. *Medical Physics*, 35(6):2485–92, June 2008.
- [15] Jeffrey Bax, David Smith, Laura Bartha, et al. A compact mechatronic system for 3D ultrasound guided prostate interventions. *Medical Physics*, 38(2):1055–1069, January 2011.
- [16] Eric Poulin, Lori Gardi, Kevin Barker, et al. Validation of a novel robot-assisted 3DUS system for real-time planning and guidance of breast interstitial HDR brachytherapy. *Medical Physics*, 42(12):6830–9, December 2015.

- [17] Peter Lim, Pei Shuen Hoskin. Prostate: Low Dose Rate Brachytherapy. In Paolo Montemaggi, Mark Trombetta, and Luther W. Brady, editors, *Brachytherapy: An International Perspective*, Medical Radiology, pages 299–318. Springer International Publishing, Cham, 2016.
- [18] Nikolai Hungr, Michael Baumann, Jean-Alexandre Long, and Jocelyne Troccaz. A 3-D Ultrasound Robotic Prostate Brachytherapy System With Prostate Motion Tracking. *IEEE Transactions on Robotics*, 28(6):1382–1397, December 2012.
- [19] Eric Poulin, Emmanuel Racine, Dirk Binnekamp, and Luc Beaulieu. Fast, automatic, and accurate catheter reconstruction in HDR brachytherapy using an electromagnetic 3D tracking system. *Medical Physics*, 42(3):1227–1232, February 2015.
- [20] H. Brastianos, T. Vaughan, M. Westerland, et al. Electromagnetic Tracking for Catheter Insertion Guidance for High-Dose-Rate Breast Brachytherapy: A Phantom Experiment. *International Journal of Radiation Oncology\*Biography\*Physics*, 96(2):E643, October 2016.
- [21] Markus Kellermeier, Jens Herbolzheimer, Stephan Kreppner, et al. Electromagnetic tracking (EMT) technology for improved treatment quality assurance in interstitial brachytherapy. *Journal of Applied Clinical Medical Physics*, 18(1):211–222, 2017.
- [22] Jun Zhou, Leonid Zamdborg, and Evelyn Sebastian. Review of advanced catheter technologies in radiation oncology brachytherapy procedures. *Cancer Management and Research*, 7:199, July 2015.
- [23] Tina Kapur, Jan Egger, Antonio Damato, Ehud J. Schmidt, and Akila N. Viswanathan. 3-T MR-guided brachytherapy for gynecologic malignancies. *Magnetic Resonance Imaging*, 30(9):1279–1290, November 2012.
- [24] Akila N. Viswanathan, Jackie Szymonifka, Clare M. Tempany-Afdhal, Desmond A. O’Farrell, and Robert A. Cormack. A prospective trial of real-time magnetic resonance-guided catheter placement in interstitial gynecologic brachytherapy. *Brachytherapy*, 12(3):240–247, May 2013.
- [25] J. Michael Fitzpatrick, Derek L.G. Hill, and Calvin R. Maurer Jr. Image Registration. In Milan Sonka and J. Michael Fitzpatrick, editors, *Handbook of Medical Imaging Volume 2. Medical Image Processing and Analysis*, pages 447–514. SPIE Press, Bellingham, WA, 2009.

- [26] Paul De Jean, Luc Beaulieu, and Aaron Fenster. Three-dimensional ultrasound system for guided breast brachytherapy. *Medical Physics*, 36(11):5099 – 5106, October 2009.
- [27] Audrey Thouvenot, Tamie Poepping, Terry M. Peters, and Elvis C. S. Chen. Characterization of various tissue mimicking materials for medical ultrasound imaging. page 97835E. International Society for Optics and Photonics, April 2016.
- [28] D W Rickey, P A Picot, D A Christopher, and A Fenster. A wall-less vessel phantom for Doppler ultrasound studies. *Ultrasound in Medicine & Biology*, 21(9):1163–76, January 1995.
- [29] Andriy Fedorov, Reinhard Beichel, Jayashree Kalpathy-Cramer, et al. 3D Slicer as an image computing platform for the Quantitative Imaging Network. *Magnetic Resonance Imaging*, 30(9):1323–1341, November 2012.
- [30] J.M. Fitzpatrick, J.B. West, and C.R. Maurer. Predicting error in rigid-body point-based registration. *IEEE Transactions on Medical Imaging*, 17(5):694–702, 1998.
- [31] Derek Cool, Shi Sherebrin, Jonathan Izawa, Joseph Chin, and Aaron Fenster. Design and evaluation of a 3D transrectal ultrasound prostate biopsy system. *Medical Physics*, 35(10):4695–4707, September 2008.
- [32] P.J. Besl and Neil D. McKay. A method for registration of 3-D shapes. *IEEE Transactions on Pattern Analysis and Machine Intelligence*, 14(2):239–256, February 1992.
- [33] Jessica Robin Rodgers, Kathleen Surry, Eric Leung, David D’Souza, and Aaron Fenster. Toward a 3D transrectal ultrasound system for verification of needle placement during high-dose-rate interstitial gynecologic brachytherapy. *Medical Physics*, 44(5):1899–1911, May 2017.
- [34] J Kishimoto, S de Ribaupierre, D S C Lee, et al. 3D ultrasound system to investigate intraventricular hemorrhage in preterm neonates. *Physics in Medicine and Biology*, 58(21):7513–26, November 2013.
- [35] Alfred M. Franz, Tamas Haidegger, Wolfgang Birkfellner, et al. Electromagnetic Tracking in Medicine - A Review of Technology, Validation, and Applications. *IEEE Transactions on Medical Imaging*, 33(8):1702–1725, August 2014.

- [36] NDI Medical. NDI Medical - Polaris Specifications. <https://www.ndigital.com/medical/products/polaris-family/#specifications>. Accessed 2017-08-09.
- [37] S Nath, Z Chen, N Yue, S Trumppore, and R Peschel. Dosimetric effects of needle divergence in prostate seed implant using  $^{125}\text{I}$  and  $^{103}\text{Pd}$  radioactive seeds. *Medical Physics*, 27(5):1058–66, May 2000.
- [38] Thomas A. Buchholz and Eric A. Strom. Accelerated Partial Breast Irradiation: History, Rationale, and Controversies. In David E Wazer, Douglas W. Arthur, and Frank A. Vicini, editors, *Accelerated Partial Breast Irradiation: Techniques and Clinical Implementation*, chapter 1, pages 1–17. Springer-Verlag, Berlin, Heidelberg, 2nd edition, 2009.

# Chapter 3

## Conclusions and Future Work

### 3.1 Overview and Research Questions

This thesis sought to reduce the operator dependence and procedural complexity of PBSI by developing a system for intraoperative 3D image guidance tailored to the needs of the procedure. As clinical data on the efficacy of PBSI matures and its advantages are recognized, the development of this guidance system is crucial in making PBSI easier for centres to adopt and ensuring that this promising procedure is available to the women who would benefit from it.

### 3.2 Summary and Conclusions

As discussed in Chapter 2, a 3D US system with integrated template tracking has been developed and its performance systematically validated. Three-dimensional image reconstruction was shown to have linear and volumetric measurement accuracy consistent with previously reported 3D US systems, and a pilot study with a healthy volunteer demonstrated its ability to produce high quality images of breast tissue. The developed tracking arm showed point measurement error of  $0.43 \pm 0.19$  mm and allowed the tip position and trajectory of inserted needles to be predicted to within errors of  $2.46 \pm 0.88$  mm and  $1.6 \pm 1.5^\circ$ . Lastly, a proof-of-concept phantom procedure was performed using the system that resulted in an average needle tip and trajectory error of  $2.08 \pm 0.73$  mm and  $2.64 \pm 0.28^\circ$ . Modelled seed positions of the phantom procedure, representing an optimistic estimate of implant accuracy, were an average of  $2.50 \pm 0.67$  mm from their intended positions. To our knowledge, this represents the first report of a phantom PBSI procedure delivered using intraoperative 3D image guidance.

In summary, this thesis describes 1) the design of a novel 3D US guidance system for PBSI, 2) the systematic validation of the system and characterization of step-wise

errors in the system, and 3) a proof of concept phantom study illustrating the potential workflow for adoption of the system in the clinic.

In addition to the development and validation described above, a second system has been delivered to clinical collaborators in Kelowna, Canada. The system has received investigational testing authorization by Health Canada for use in scanning patients post-lumpectomy as part of a feasibility study.

Relative to prior efforts to improve the workflow of PBSI, the developed system is, to our knowledge, the first to provide 3D image guidance in a common coordinate system with the delivered needles. An intraoperative coordinate system was first introduced to PBSI with the template and fiducial needle approach of Pignol et al. in place of a free hand approach [1]. While the use of a gridded template introduced an intraoperative coordinate system to the procedure, unlike the presently developed system, intraoperative imaging was not registered to that coordinate system. The spatial relationship between intraoperative imaging and the needle template could only be approximated by fiducial needle visibility and visual inspection of the template and US probe. The introduction of a room-laser and skin tattoos by Batchelar et al. improved on the alignment procedure of Pignol et al. to make intraoperative set-up and needle template positioning more repeatable [2]. However, the use of external tattoos relies on the shifts in external anatomy as a heuristic for movement of the internal anatomy, where-as the presently developed system offers the possibility for internal anatomy to be localized directly. Lastly, prior work by Ravi et al. developing a gamma camera system offered the potential for intraoperative localization of implanted seeds in 3D [3, 4]. The use of a gamma camera intraoperatively with PBSI has the advantage of imaging seeds with better contrast than can be achieved using US due to the radioactivity present in the seeds and absent elsewhere. Additionally, while the presently described 3D US system guides needle placement, implant quality is determined by the seed positions. Any additional displacements resulting from the process of seed dropping is not reduced by the 3D US system and it remains to be seen if seeds in breast tissue can be accurately localized using the system. Conversely, the developed gamma camera system was able to locate seeds in a phantom with a median error of 1 mm [4]. However, unlike the gamma camera system, our 3D US approach can provide prospective guidance in the delivery of needles to the breast rather than being limited to assessment of seeds already implanted. Additionally, the gamma camera is unable to visualize anatomy, and detection of misplaced seeds using the gamma camera system would require fusing the images it produces with an anatomical imaging modality such as ultrasound [4]. In this respect, the presented 3D US guidance system has the distinct advantage of offering a clear value-add to the PBSI procedure as-is, irrespective



of any further technical developments or incorporation of other technology, where-as the clinical utility of a gamma camera that is not anatomically aligned is less clear. The potential advantages offered by the use of a gamma camera may be realized by combining it with our 3D US system, however clinical translation of our system is warranted regardless of whether or not the gamma camera system is incorporated.

In addition to placing the present work in the context of previous developments in streamlining PBSI, an interpretation of the system's performance with respect to alternative strategies that could have been adopted is warranted. Electromagnetic (EM) tracking has been previously used for brachytherapy guidance [5–8], as discussed in Section 2.4.3 and has the advantage of not requiring line-of-sight. However, the observed point measurement error of  $0.43 \pm 0.19$  mm in the tracking arm was similar to or better than reported errors for EM tracking; 0.25–1.19 mm and 0.26–7.59 mm in undistorted and distorted environments, respectively [9]. While EM tracking offers the potential to track needles directly, this approach is complicated by the use of pre-loaded needles, with the seeds to be deposited occupying the usual placement position of EM sensors. As a result, as discussed in Section 2.2.1, using EM approaches to track needles directly without altering the clinical workflow would require sensors placed distal to the needle tip and on every needle, reducing accuracy and drastically increasing the number of sensors required. Conversely, using an EM approach to track one or both of the needle template or US transducer would be potentially feasible, subject to modification of the surrounding equipment to mitigate electromagnetic distortion, such as material selection in the needle template, template support and patient bed, and the use of a tracked-freehand approach to 3D US rather than a mechatronic approach. However, the added cost and complexity of an EM system and the requirement of specialized equipment that mitigates EM distortion are both at odds with the goal of making PBSI easier for clinicians to adopt.

Rather than EM tracking, intraoperative MRI guidance could also have been explored, having been previously used to guide gynecological [10, 11] and prostate [12] brachytherapy. However, the spread of these approaches has been limited by access to MRI and the costs of imaging [13], potentially making the use of MRI an impediment to adoption rather than an advantage.

Lastly with respect to alternative guidance approaches is the use of optical tracking, arguably the de-facto standard for medical tool tracking [14]. As discussed in Section 2.4.3, manufacturer reported values for optical tracking point error of 0.25–0.35 mm [15] are marginally better than the presently reported values of  $0.43 \pm 0.19$  mm. Additionally, while optical tracking requires line-of-sight to the tool being tracked, the 3D US scanner and needle template remain fixed throughout the majority of the procedure, making it

possible for the line-of-sight requirement to be satisfied only intermittently under the assumption that the scanner and template remain stationary when tracking is occluded. The use of optical tracking has the additional advantage of providing continuous rather than intermittent template tracking, which may be advantageous when adjusting the template position at the beginning of the procedure. Given these potential advantages of optical tracking, the selection and development of a mechanical tracking approach represents a design choice that emphasises simplicity of design and workflow integration. Introduction of an optical tracking system adds additional equipment to the operating room, both a camera and a floor or ceiling mount to support it, and the necessary reflective markers for optical tracking add additional bulk to the scanner and needle template. Conversely, when not in use, the tracking arm described in this thesis folds against the 3D US scanner, occupying a space of only  $8\text{ cm} \times 9\text{ cm} \times 6\text{ cm}$ . For comparison, the smaller of the two optical tracking systems offered by NDI Medical (Polaris Vicra) is approximately  $9\text{ cm} \times 9\text{ cm} \times 27\text{ cm}$  in size [15]. Additionally, modifications to the template to allow for mechanical tracking are limited to unobtrusive and sterilisable divots around the outer edge rather than potentially bulky, single-use extensions. The complications of intermittent rather than continuous tracking is thought to be surmountable by improvements in the ability to accurately implement changes to the needle template position using simple mechanical actuators (e.g. translation stages) incorporated in the needle template support, discussed further below. Furthermore, the mechanical approach is hypothesized to be less expensive than an optical or EM tracking approach. While the cost of a commercially developed tracking arm is difficult to estimate accurately, material costs at the prototype phase are in the hundreds of Canadian dollars. In comparison, both optical and EM tracking systems typically cost tens of thousands of dollars. The ability to implement controlled, mechanically actuated adjustments would allow for template position changes to be made accurately and precisely, mitigating the need for continuous feedback. The resulting system is thought to be better suited for smooth integration into the operating room, a key consideration for a project aimed primarily at facilitating adoption.

### 3.3 Limitations

The largest limitation of the presented work is that much of the utility of the developed system rests on the underlying presumption that its use will make PBSI easier for clinicians to learn and repeatably deliver. As was described in Chapter 1, the ultimate goal of developing the presented system is to facilitate the adoption of PBSI by simplifying and streamlining the procedure through the use of an intraoperative guidance

system. The presented investigation explores only the calibration and accuracy of the guidance system, and while accuracy is a necessary condition for the system’s intended impact, it is not a sufficient condition. While the application of image guidance tools in other areas of brachytherapy, particularly permanent seed prostate implants, and input from the PBSI team in Kelowna, Canada provide support for the presumed impact of the system, the effect of its use in the clinic remains to be seen. Validating the expected impact of the developed guidance system on the clinical workflow and operator dependence of PBSI will be a key focus of future work, discussed further below.

With respect to the system itself, the guidance offered by the developed system centres primarily on the guidance of needles to their intended location, but the dosimetric quality of the implant is determined by the position of the implanted seeds. The introduction of any additional displacements between the “modelled” seed position, as described in the phantom procedure of Chapter 2, and the final implanted locations of the seeds are not expected to be reduced by using the developed system. Additionally, post-implant migration of the seeds has been observed and also contributes to implant quality [16], but is unlikely to be affected by the system’s use. Lastly, while the proof-of-concept phantom procedure used a rigid, surface based registration to align the pre-operative plan with intraoperative imaging, seroma deformations and differences in appearance between CT and 3D US would make this approach inadequate for patient procedures. As a result, the presently used process of using skin tattoos and other external markers for intraoperative patient setup would likely still be required to supplement the guidance provided by 3D US imaging until future work integrating (semi-) automatic segmentation in 3D US and non-rigid registration with CT, discussed further below, can be developed and incorporated.

## 3.4 Future Work

A number of additional areas of research remain to be explored in the application of this device, including further refining the device’s hardware and software as well as work related to its clinical translation.

### 3.4.1 Device Refinements

#### 3.4.1.1 Hardware Refinements

The work described in Chapter 2 identified the measurements made by the template tracking arm and its registration to the 3D US scanner as a dominant source of residual guidance error. To this end, future work in refining the physical construction of the tracking arm and its method of registration to the 3D US scanner is warranted for future iterations of the device. With respect to the tracking arm, it was observed during testing

that the tracking arm was susceptible to small amounts of bending in the lengths of the arm during use. For instance, with the scanner and arm held in fixed positions, a modest amount of force on the most distal joint of the arm (e.g. pushing on the joint with my pinky finger) could result in a change in the measured arm position of up to 1.4 mm. This error is large enough to potentially explain the discrepancy observed in Chapter 2 between validation of point measurement error (mean 0.43 mm) and the point-wise error observed during template localization (mean 1.56 mm). A susceptibility to deformation would also present an obstacle to the robustness of the system's performance in a practical scenario. To lessen the tracking arm's susceptibility to bending under force, future work could consider using stiffer materials than the 3D printed nylon used currently or the use of machined components rather than 3D printed ones. Alternatively, size or shape of the lengths could also be considered to increase the moment of inertia of the beam in axes most susceptible to load, such as an I-beam shape in the two most distal joints oriented parallel with the axis of the joint between them.

Additionally, as was alluded to in Section 2.4.7, the ability of the device's template tracking to guide template positioning is limited by the user's ability to implement desired changes. While the configuration of the template support used during the phantom procedure made fine rotational adjustments challenging, future work in refining the template support used intraoperatively could mitigate these challenges during patient procedures. The incorporation of calibrated translation and/or rotation stages in the needle template support would allow a simple and reliable mechanism for adjusting the needle template based on measurements made using the template tracking arm. The geometry of the stages, including the axes of translation and centres of rotation with respect to the template, could be incorporated into the device's accompanying software so that the adjustments necessary to move the template to a given position and orientation could be calculated automatically and displayed for the user to implement. In this way, a closed loop could be more accurately created between measurements and adjustments of the template position, expediting needle template setup and enhancing the value added to the procedure through use of the system's template tracking.

Furthermore, during registration of the 3D US image to the geometry of the scanner, a shift in the image consistent with mechanical backlash was observed. This backlash causes 3D images to show a small region at one extent of the volume in which 2D US frames have been repeated, consistent with measured encoder motion in the 'dead space' of the gears when the 2D US transducer has not yet moved. While the effects of the backlash on image position are accounted for in the registration process, the consistency in the amount of backlash in the gears over time remains to be seen, possibly requiring more frequent

recalibration. Additionally, the backlash phenomenon may also be contributed to by backlash resulting from physical bending in the links between the motor and transducer, particularly in the 3D printed plastic components customized to the transducer model that link it to the rest of the drive-train. Backlash due to deformation may vary with the contact pressure applied between the scanner and the skin, particularly if the TPX™ plate bends enough to make contact with the US transducer, which would alter the position of the 3D image with respect to the scanner, leading to targeting error. For these reasons, consistency of the relationship between the 3D image and the probe volume over time and as a function of contact pressure should be explored. It may also be advantageous to move the position of the encoder further down the drive train to be closer to the transducer in order to minimize the effect of backlash in the first place.

In addition to improving the accuracy of the system, practical considerations of the device's use in a sterile environment should also be considered in future work. Sterility at the imaging surface will most likely be accomplished by 'bagging' the device with a sterile cover. Conversely, sterility at the interface of the tracking arm and needle template may be accomplished by either a 'bagging' strategy or by using a 'cheater plate' that mounts to the needle template via the existing gridded template holes. The plate would have the fiducial divots used for registration around its outer edges, allowing the tracking arm to 'cheat' by measuring the position of a sterilisable plate as a proxy for the template itself. As a result of the non-sterile pre-setup technique developed by Batchelar et al. [2], the devised solution should accommodate the use of the device both before and after the surrounding skin is sterilized, such as by allowing a sterile covering to be donned during the procedure.

#### 3.4.1.2 Software Refinements

With respect to the device's software and user interaction, future work should focus on features that aid in the interpretation of the data generated by the guidance system, including segmentation and registration algorithms. As was alluded to in Section 2.4.7, the use of a rigid registration between planning CT and intraoperative 3D US seroma contours would be inadequate for patient cases. As was discussed in Section 1.3.3, the breast is a highly mobile and deformable organ and the seroma's appearance in CT and US is fundamentally different due to the underlying bases of image formation in each modality. Additionally, manual contouring of 3D US images during the procedure would be impractical. While use of the system in the current clinical workflow for needle template positioning would be valuable to clinicians, the utility of the system would be better leveraged by incorporation of segmentation and registration algorithms to streamline the workflow using internal landmarks rather than external ones. Future work in this area

would include the development of an automatic or semi-automatic seroma segmentation algorithm to be applied to intraoperative 3D US images. Intraoperative seroma segmentation would offer improved visualization of the surgical target with respect to the needle template as well as allow for quantitative feedback on the position of the needle template with respect to the seroma, such as quantifying the distance between the expected trajectory of the fiducial needle and the centroid of the seroma.

Additionally, coupling the seroma segmentation algorithm with a non-rigid registration to the pre-operative plan would allow for intraoperative visualization of the 3D treatment plan and intraoperative estimates of dosimetry. Given the modality dependence of the seroma's size and shape, one possible strategy for achieving this non-rigid registration would be to use a multi-step approach. The pre-operative CT used for creation of the treatment plan would be non-rigidly registered to a pre-operative 3D US image which is in turn registered to the intra-operative 3D US image using a non-rigid, boundary based approach such as thin plate spline registration. By treating the registration as a multi-step process, state of the art registration techniques may be used to tackle the challenging problem of non-rigid, CT to 3D US breast registration with minimal concern for computational complexity, simplifying the remainder of the registration task which must be performed in a time-sensitive context. The addition of a 3D US scan during treatment planning would be consistent with previous literature suggesting its value [17].

In addition to software tools assisting with plan registration and needle template alignment, the incorporation of needle segmentation algorithms could be of additional assistance in guiding needle insertion once the template is aligned. With previously developed algorithms for segmentation of multiple needles from a 3D US volume [18] available and work within the lab on real-time segmentation of a needle in a 2D US image ongoing, future work in this area would require only adaptation and validation of techniques developed for other applications.

### 3.4.2 Clinical Translation

In addition to future work refining the device's capabilities, clinically oriented future work is also necessary to move the device towards guiding patient procedures. As was mentioned above, the device has already been given investigational testing authorization by Health Canada for imaging of the breast. Irrespective of any further development or validation, the device is ready to be put to use in a usability study, capturing images of patients post-lumpectomy during the planning stages of PBSI or other breast radiotherapy. Future work in this area will allow for early feedback from end users on

device usability, user interface and feature requests. Additionally, images generated from usability testing will provide data to develop and test the proposed segmentation and registration algorithms described above.

Furthermore, to evaluate the hypothesis that the developed system will improve accuracy and operator dependence of the procedure, future work should evaluate the delivery of a mock-PBSI procedure in a phantom using both the presently described system and the current clinical techniques and compare the resulting procedure time and seed placement accuracy. Evaluation in a phantom allows for comparisons to be made in delivering the same plan to the same anatomy, a level of control which would not be possible in patient populations. These phantom procedures would likely follow a similar workflow to the phantom procedure described in Section 2.2.2.7, with the following modifications. First, the use of a higher fidelity phantom that allows for more accurate modelling of the mobile and deformable nature of the breast. Movement and non-rigid deformation of the internal target is a key challenge of the procedure and should be accounted for in a comparison study. Second, the phantom procedure should be conducted by an operator more representative of the skill set of a radiation oncologist who might adopt the procedure, such as a radiation oncologist who has not previously performed a PBSI procedure or a radiation oncology resident. Employment of a user untrained in percutaneous interventions would unfairly favor the guided procedure by inaccurately representing the clinical judgement available during the 2D US guided approach. Lastly, the phantom study should employ the deposition of (non-radioactive) seeds into the phantom. The use of seeds was avoided in the reported phantom procedure because of the potential for unrepresentative errors to be introduced due to the limited skill set of a non-clinically trained user. Furthermore, it would not have been possible to differentiate between error due to seed-dropping and error due to the guidance system. Employing a more representative user and comparing the results to a control intervention in which seed-drop error is also present would avoid those concerns, making a higher fidelity phantom procedure practical.

Lastly, assuming favourable findings from the phantom comparison study, future work should include a pilot study in which the device is used to guide PBSI intraoperatively. To reduce the total number of patients that need to be enrolled in such a study before a conclusion may be made, a timeseries design could be used, in which metrics such as procedure time and seed implantation error for patients treated at a given centre are compared before and after the adoption of the guidance system during the procedure.

# References

- [1] JP Pignol, B Keller, E Rakovitch, et al. A breast permanent implant (BPI) for partial breast irradiation using  $^{103}\text{Pd}$  stranded seeds: A comparison of a ‘free hand’ versus a ‘fiducial needle’ technique. *Radiotherapy and Oncology*, 72:S57, September 2004.
- [2] Deidre Batchelar, Michelle Hiltz, Tracey Rose, et al. Simulation and Intraoperative Checks for Improved Standardization and Reproducibility of Partial Breast Seed Implant Technique. In *Brachytherapy*, volume 13, page S84, March 2014.
- [3] Ananth Ravi, Curtis B Caldwell, Brian M Keller, Alla Reznik, and Jean-Philippe Pignol. Online gamma-camera imaging of  $^{103}\text{Pd}$  seeds (OGIPS) for permanent breast seed implantation. *Physics in Medicine and Biology*, 52(19):5921–32, October 2007.
- [4] Ananth Ravi, Curtis B Caldwell, and Jean-Philippe Pignol. Experimental evaluation of an online gamma-camera imaging of permanent seed implantation (OGIPSI) prototype for partial breast irradiation. *Medical Physics*, 35(6):2485–92, June 2008.
- [5] H. Brastianos, T. Vaughan, M. Westerland, et al. Electromagnetic Tracking for Catheter Insertion Guidance for High-Dose-Rate Breast Brachytherapy: A Phantom Experiment. *International Journal of Radiation Oncology\*Biological\*Physics*, 96(2):E643, October 2016.
- [6] Markus Kellermeier, Jens Herbolzheimer, Stephan Kreppner, et al. Electromagnetic tracking (EMT) technology for improved treatment quality assurance in interstitial brachytherapy. *Journal of Applied Clinical Medical Physics*, 18(1):211–222, 2017.
- [7] Eric Poulin, Emmanuel Racine, Dirk Binnekamp, and Luc Beaulieu. Fast, automatic, and accurate catheter reconstruction in HDR brachytherapy using an electromagnetic 3D tracking system. *Medical Physics*, 42(3):1227–1232, February 2015.



- [8] Jun Zhou, Leonid Zamdborg, and Evelyn Sebastian. Review of advanced catheter technologies in radiation oncology brachytherapy procedures. *Cancer Management and Research*, 7:199, July 2015.
- [9] Alfred M. Franz, Tamas Haidegger, Wolfgang Birkfellner, et al. Electromagnetic Tracking in Medicine - A Review of Technology, Validation, and Applications. *IEEE Transactions on Medical Imaging*, 33(8):1702–1725, August 2014.
- [10] Tina Kapur, Jan Egger, Antonio Damato, Ehud J. Schmidt, and Akila N. Viswanathan. 3-T MR-guided brachytherapy for gynecologic malignancies. *Magnetic Resonance Imaging*, 30(9):1279–1290, November 2012.
- [11] Akila N. Viswanathan, Jackie Szymonifka, Clare M. Tempny-Afdhal, Desmond A. O’Farrell, and Robert A. Cormack. A prospective trial of real-time magnetic resonance-guided catheter placement in interstitial gynecologic brachytherapy. *Brachytherapy*, 12(3):240–247, May 2013.
- [12] Cynthia Ménard, Robert C Susil, Peter Choyke, et al. MRI-guided HDR prostate brachytherapy in standard 1.5T scanner. *International Journal of Radiation Oncology\*Biology\*Physics*, 59(5):1414–1423, August 2004.
- [13] Kari Tanderup, Akila N. Viswanathan, Christian Kirisits, and Steven J. Frank. Magnetic Resonance Image Guided Brachytherapy. *Seminars in Radiation Oncology*, 24(3):181–191, July 2014.
- [14] Wolfgang Birkfellner, Johann Hummel, Emmanuel Wilson, and Kevin Cleary. Tracking Devices. In *Image-Guided Interventions*, pages 23–44. Springer US, Boston, MA, 2008.
- [15] NDI Medical. NDI Medical - Polaris Specifications. <https://www.ndigital.com/medical/products/polaris-family/#specifications>. Accessed 2017-08-09.
- [16] Brian M Keller, Ananth Ravi, Raxa Sankrecha, and Jean-Philippe Pignol. Permanent breast seed implant dosimetry quality assurance. *International Journal of Radiation Oncology\*Biology\*Physics*, 83(1):84–92, May 2012.
- [17] Daniel Morton, Deidre Batchelar, Michelle Hilts, Tanya Berrang, and Juanita Crook. Incorporating three-dimensional ultrasound into permanent breast seed implant brachytherapy treatment planning. *Brachytherapy*, 16(1):167–173, January 2017.

- [18] William Thomas Hrinivich, Douglas A. Hoover, Kathleen Surry, et al. Simultaneous automatic segmentation of multiple needles using 3D ultrasound for high-dose-rate prostate brachytherapy. *Medical Physics*, 44(4):1234–1245, April 2017.

## Appendix A: Letter to the Editor

The contents of this appendix have previously been published as a letter to the editor: Michael J, Crook J, Morton D, Batchelar D, Hilts M, Fenster A. Reply to: Who Should Bear the Cost of Convenience? A Cost-effectiveness Analysis Comparing External Beam and Brachytherapy Radiotherapy Techniques for Early Stage Breast Cancer. *Clin Oncol.* 2017;29(6):392-393. doi:10.1016/j.clon.2017.03.003. Permission to reproduce the article was granted by Elsevier and is provided in Appendix D.

We read with interest, Who Should Bear the Cost of Convenience? A Cost-effectiveness Analysis Comparing External Beam and Brachytherapy Radiotherapy Techniques for Early Stage Breast Cancer [1], and seek to comment on the effect of patient travel distance on total procedure cost.

The authors modelled patient travel cost using the Canada Revenue Agency (CRA) travel allowance and a one-way travel distance of 38 km. The reported sensitivity analysis considered variations of  $\pm 50\%$  (19–57 km) and found treatment cost ranking remained unchanged. However, patient travel distance can greatly exceed 57 km. For instance, at the Centre for the Southern Interior (CSI) in Kelowna, Canada, patients are drawn from up to 375 km away.

While the maximum distance investigated did not change treatment cost rankings, is there a threshold distance that would? The travel cost model's linear nature and reported sensitivity analyses allow the reader to infer a threshold of approximately 94 km. Above this threshold, the model appears to predict total costs of PBSI to be lower than WBI.

At the CSI, two of the four regions served lie entirely outside of this 94 km threshold, representing 25% of patients, while both of the other regions extend partially outside of it. In total, an estimated 45% of CSI breast cancer patients reside >94 km away.

With respect to the travel cost model, the CRA travel allowance is given "in addition to salary or wages" [2], suggesting it does not account for the value of patients' time during travel. Additionally, no consideration is made for patients requiring overnight lodging. Both of these considerations suggest the true threshold distance is lower.

While this paper is already a timely and valuable contribution, the consideration of greater travel distances has important implications for centres serving large geographical areas. We invite the authors to comment on the threshold distance described using original data.

### Explanatory Note - Calculations

The calculation of travel costs in “Who Should Bear the Cost of Convenience?”, are described as follows:

To estimate travel costs, an average one-way travel distance of 38 km was calculated based on the travel distance for patients undergoing cancer treatment reported by three previous studies [23-25]. This was multiplied by the Canada Revenue Agency travel allowance for 2013 (0.54 \$/km) [26] and summed over all appointments for each technique.

From this description, it can be inferred that travel cost as calculated for a given treatment method can be described as:

$$\text{Travel Cost} = \text{One Way Travel Distance} \times 2 \times \text{Travel Allowance per km} \times \text{Number of Appointments}$$

The above equation implies that travel cost is proportional to travel distance, further implying that each added kilometer to one-way travel distance increases the total cost of the procedure by a constant amount. The added cost of each kilometer of travel distance can be inferred from results of the sensitivity analysis according to the equation,

$$\text{Cost per km Travel Distance} = \frac{\text{Total Treatment Cost} \times \% \text{ Cost Change in Sensitivity Analysis}}{\text{Distance Change in Sensitivity Analysis}}$$

Applied to each of WBI and PBSI, this equation yields a cost per km for each procedure of,

	Total Treatment Cost (Base Case)	% Cost Change in Sensitivity Analysis	Distance Change in Sensitivity Analysis (km)	Cost per km
WBI	\$ 6,200.00	18%	19	\$58.74
PBSI	\$ 8,700.00	3%	19	\$13.74
Diff.	\$ (2,500.00)	-	-	\$45.00

From the above, the travel distance at which the two procedures have equal total cost (critical distance) may be calculated as follows,

$$\text{Critical Distance} = \text{Base Case Distance} + \frac{\text{Total Cost Difference}}{\text{Difference in Cost per km}} = 93.6 \text{ km}$$

## References

- [1] M. McGuffin, T. Merino, B. Keller, and J.-P. Pignol, “Who Should Bear the Cost of Convenience? A Cost-effectiveness Analysis Comparing External Beam and Brachytherapy Radiotherapy Techniques for Early Stage Breast Cancer,” *Clinical Oncology*, vol. 29, pp. e57–e63, Mar. 2017.
- [2] Canada Revenue Agency, “Automobile and motor vehicle allowances.” <http://www.cra-arc.gc.ca/tx/bsnss/tpcs/pyrll/bnfts/tmbl/llwnc/menu-eng.html>, 2017.

## Appendix B: 94km Map - Methods

The map of travel distance thresholds around Canadian radiation therapy centres described in Chapter 1 was created by:

1. Identifying the locations of Canadian radiation therapy centres,
2. Identifying areas within 93.6 km travel distance from one or more centres,
3. Cropping the identified areas to include only regions in Canada, and
4. Estimating the proportion of the Canadian population outside the identified areas using NASA's Gridded Population of the World, Version 4.

Canadian radiation oncology centres were identified using lists of cancer centres published by the Canadian Association of Radiation Oncology<sup>1</sup> and the Canadian Organization of Medical Physicists.<sup>2</sup> These lists were supplemented with additional information from Alberta Health Services.<sup>3</sup> GPS coordinates of the manually identified cancer centres were identified using a custom map in Google My Maps and exported as a KML file. A complete list of the centres identified is included below.

To identify the areas within 93.6 km of one or more of the identified cancer centres, custom MATLAB functions were created using MATLAB 2016a (MathWorks, Natick, USA) to parse the GPS locations of the centres from the exported KML file. 93.6 km travel-distance isolines were sequentially requested around each location using the MATLAB 'webread' function and a trial version of the HERE application programming interface (API).<sup>4</sup> The HERE API is a third party service that interfaces with the Google Maps API and returns requests in JSON format. The returned JSON files contained GPS coordinates defining the travel-distance isoline for each location which was, in turn, written to a KML file as separate, possibly overlapping, polygons. The KML file containing the polygons was then loaded into the open-source geographic information system (GIS) software QGIS<sup>5</sup> which was used to merge ('dissolve') the overlapping contours into non-overlapping ones.

---

<sup>1</sup><http://www.caro-acro.ca/patients/canadian-radiation-oncology-centres/>

<sup>2</sup><http://www.comp-ocpm.ca/english/career-education/career-resources/canadian-cancer-centres.html>

<sup>3</sup><http://www.albertahealthservices.ca/info/service.aspx?id=1025904>

<sup>4</sup><https://developer.here.com/>

<sup>5</sup><http://www.qgis.org/en/site/>

Once merged, an outline of the Canadian border was downloaded from the Database of Global Administrative Areas (GADM)<sup>6</sup> and imported into QGIS. Merged isolines were cropped to the Canadian border using the ‘clip’ tool and re-saved as a KML file that was uploaded to Google My Maps. The result, including names and locations of the cancer centres identified and the merged and cropped isolines, are available here: <http://bit.ly/94kmMap>

Lastly, the proportion of the Canadian population outside of the identified regions was calculated by summing published data of population by area across Canada and across the regions within the 93.6 km isolines. Population data were taken from the United States National Aeronautics and Space Administration (NASA) Gridded Population of the World, Version 4.<sup>7</sup> The downloaded population data parcel the geography of the world into a grid with a resolution of 30 arc-seconds (approximately 1 km at the equator) and contain an estimate of the population within each cell of that grid. Population data was cropped to the Canadian border, as defined by the GADM data mentioned previously, using QGIS and the total population within determined. The above process was then repeated using the merged and cropped 93.6 km isolines rather than the Canadian border. The proportion of the Canadian population inside the isolines was calculated as the ratio of the two population estimates and the proportion outside the isolines taken as its complement.

#### Identified Canadian Radiation Oncology Centres

- BC Cancer Agency - Abbotsford Centre, Abbotsford, British Columbia
- BC Cancer Agency - Centre for the North, Prince George, British Columbia
- BC Cancer Agency - Centre for the Southern Interior, Kelowna, British Columbia
- BC Cancer Agency - Fraser Valley, Surrey, British Columbia
- BC Cancer Agency - Vancouver Centre, Vancouver, British Columbia
- BC Cancer Agency - Vancouver Island Centre, Victoria, British Columbia
- Cross Cancer Institute, Edmonton, Alberta
- Tom Baker Cancer Centre, Calgary, Alberta

---

<sup>6</sup><http://www.gadm.org/country>

<sup>7</sup><http://sedac.ciesin.columbia.edu/data/collection/gpw-v4>

- Central Alberta Cancer Centre, Red Deer, Alberta
- Jack Ady Cancer Centre, Lethbridge, Alberta
- Allan Blair Cancer Centre, Regina, Saskatchewan
- Saskatoon Cancer Clinic, Saskatoon, Saskatchewan
- Cancer Care Manitoba, Winnipeg, Manitoba
- Cancer Care Manitoba (Brandon), Brandon, Manitoba
- Windsor Regional Cancer Program, Windsor, Ontario
- London Regional Cancer Program, London, Ontario
- Grand River Regional Cancer Centre, Kitchener, Ontario
- Juravinski Cancer Centre, Hamilton, Ontario
- Carlo Fidani Peel Regional Cancer Centre, Mississauga, Ontario
- Odette Cancer Centre, Toronto, Ontario
- Princess Margaret Cancer Centre, Toronto, Ontario
- Stronach Regional Cancer Centre, Newmarket, Ontario
- R.S. McLaughlin Durham Regional Cancer Centre, Oshawa, Ontario
- Cancer Centre of Southeastern Ontario, Kingston, Ontario
- The Ottawa Hospital Cancer Centre, Ottawa, Ontario
- Simcoe Muskoka Regional Cancer Centre, Barrie, Ontario
- North East Cancer Centre, Sudbury, Ontario
- North West Regional Cancer Care, Thunder Bay, Ontario
- McGill University Health Centre, Montreal, Quebec
- Jewish General Hospital, Montreal, Quebec
- Hôpital Maisonneuve-Rosemont, Montreal, Quebec
- CHUM Hôpital Notre-Dame, Montreal, Quebec



- Hôpital Charles Lemoyne, Greenfield Park, Quebec
- CSSL - Hôpital de Laval, Laval, Quebec
- CSSSRN - Rimouski, Rimouski, Quebec
- CHRTR - Trois-Rivières, Trois-Rivières, Quebec
- CHUQ - Hôtel-Dieu de Québec, Quebec City, Quebec
- CSSSG - Centre Hospitalier de Gatineau, Gatineau, Quebec
- CHUS - Centre Hospitalier Unviersitaire de Sherbrooke, Sherbrooke, Quebec
- CSSS - Complexe Hospitalier de la Sagamie, Chicoutimi, Quebec
- Dr. Léon-Richard Oncology Centre, Moncton, New Brunswick
- Saint John Regional Hospital, Saint John, New Brunswick
- Nova Scotia Cancer Centre, Halifax, Nova Scotia
- Cape Breton Cancer Centre, Sydney, Nova Scotia
- Dr. H. Bliss Murphy Cancer Clinic, St. John's, Newfoundland and Labrador
- PEI Cancer Treatment Centre, Charlottetown, Prince Edward Island

# Appendix C: Ethics Approval

**Date:** September 29, 2016

**Principal Investigator:** Dr. Aaron Fenster

**Department & Institution:** Schulich School of Medicine and Dentistry\Medical Biophysics,Robarts Research Institute

**Review Type:** Delegated

**HSREB File Number:** 106995

**Study Title:** Feasibility of Using a 3D Ultrasound Imaging System for High Resolution Breast Imaging

**Sponsor:** Ontario Research fund

**HSREB Renewal Due Date & HSREB Expiry Date:**

Renewal Due -2017/09/30

Expiry Date -2017/10/01

The Western University Health Science Research Ethics Board (HSREB) has reviewed the Continuing Ethics Review (CER) Form and is re-issuing approval for the above noted study.

The Western University HSREB operates in compliance with the Tri-Council Policy Statement Ethical Conduct for Research Involving Humans (TCPS2), the International Conference on Harmonization of Technical Requirements for Registration of Pharmaceuticals for Human Use Guideline for Good Clinical Practice (ICH E6 R1), the Ontario Freedom of Information and Protection of Privacy Act (FIPPA, 1990), the Ontario Personal Health Information Protection Act (PHIPA, 2004), Part 4 of the Natural Health Product Regulations, Health Canada Medical Device Regulations and Part C, Division 5, of the Food and Drug Regulations of Health Canada.

Members of the HSREB who are named as Investigators in research studies do not participate in discussions related to, nor vote on such studies when they are presented to the REB.

The HSREB is registered with the U.S. Department of Health & Human Services under the IRB registration number IRB 00000940.

# Appendix D: Permission for Reproduction of Scientific Articles

Publisher's policy on personal use of articles<sup>1</sup> indicating permission for inclusion of published letter to the editor in this thesis.

---

 SEARCH  CART

---

## Personal use

Authors can use their articles, in full or in part, for a wide range of scholarly, non-commercial purposes as outlined below:

- Use by an author in the author's classroom teaching (including distribution of copies, paper or electronic)
- Distribution of copies (including through e-mail) to known research colleagues for their personal use (but not for Commercial Use)
- Inclusion in a thesis or dissertation (provided that this is not to be published commercially)
- Use in a subsequent compilation of the author's works
- Extending the Article to book-length form
- Preparation of other derivative works (but not for Commercial Use)
- Otherwise using or re-using portions or excerpts in other works

These rights apply for all Elsevier authors who publish their article as either a subscription article or an open access article. In all cases we require that all Elsevier authors always include a full acknowledgement and, if appropriate, a link to the final published version hosted on Science Direct.

---

<sup>1</sup>from: <https://www.elsevier.com/about/our-business/policies/copyright/personal-use>

# Curriculum Vitae

## Justin Michael

---

### EDUCATION

**MESC CANDIDATE: BIOMEDICAL ENGINEERING** | THE UNIVERSITY OF WESTERN ONTARIO

Sep 2015 – Nov 2017 | London, ON

**BENG: BIOMEDICAL ENGINEERING** | UNIVERSITY OF GUELPH

Sep 2010 – Apr 2015 | Guelph, ON

### RESEARCH EXPERIENCE

**GRADUATE RESEARCH ASSISTANT** | ROBARTS RESEARCH INSTITUTE

Sep 2015 – Present | London, ON

**SUMMER RESEARCH STUDENT** | ROBARTS RESEARCH INSTITUTE

Jun 2015 – Aug 2015 | London, ON

**HUMAN FACTORS STUDENT ANALYST** | UNIVERSITY HEALTH NETWORK

May 2012 – Aug 2012 | Toronto, ON

**UNDERGRADUATE RESEARCH ASSISTANT** | UNIVERSITY OF GUELPH

May 2011 – Jul 2011 | Guelph, ON

### PROFESSIONAL EXPERIENCE

**BIOMEDICAL ENGINEERING ASSOCIATE** | BAYLIS MEDICAL COMPANY

May 2014 – Dec 2014 | Mississauga, ON

**BIOMEDICAL ENGINEERING ASSISTANT** | BAYLIS MEDICAL COMPANY

May 2013 – Aug 2013 | Mississauga, ON

**MECHANICAL ENGINEERING CO-OP STUDENT** | PUBLIC HEALTH AGENCY OF CANADA

Jan 2013 – Apr 2013 | Ottawa, ON

## TEACHING EXPERIENCE

**GRADUATE TA - ADVANCED IMAGE PROCESSING & ANALYSIS** | THE UNIVERSITY OF WESTERN ONTARIO  
Jan 2017 – Apr 2017 | London, ON

**GRADUATE TA - CONTROL SYSTEMS** | THE UNIVERSITY OF WESTERN ONTARIO  
Sep 2016 – Dec 2016 | London, ON

**GRADUATE TA - CIRCUITS & SYSTEMS** | THE UNIVERSITY OF WESTERN ONTARIO  
Jan 2016 – Apr 2016 | London, ON

**GRADUATE TA - CONTROL SYSTEMS** | THE UNIVERSITY OF WESTERN ONTARIO  
Sep 2015 – Dec 2015 | London, ON

## AWARDS & HONOURS

2017	NSERC Postgraduate Scholars - Doctoral	\$63,000	National award - merit based (awarded, not held)
2017	Queen Elizabeth II Graduate Scholarship in Science and Technology (Doctoral)	\$15,000	Provincial award - merit based (awarded, not held)
2017	Proteus Innovation Competition	\$7,500	1st place in business plan competition (team of 4)
2016	Ontario Women's Health Scholars Award	\$26,000	Provincial award - merit based
2016	Translational Breast Cancer Research Unit Studentship	\$17,000	Institutional award - merit based (awarded, not held)
2016	NSERC Canada Graduate Scholarships - Master's	\$17,500	National award - merit based (awarded, not held)
2016	Queen Elizabeth II Graduate Scholarship in Science and Technology (Master's)	\$15,000	Provincial award - merit based (awarded, not held)
2015	Western Graduate Research Scholarship	\$14,200	Research based
2015	Gordon F Morton Award	-	Academics, athletics and extra-curricular activities
2014	NSERC Industrial Undergraduate Student Research Award	\$4,500	Industrial research & development (Baylis Medical)

2014	Association of Professional Engineers of Ontario Scholarship	\$1,000	Academic excellence and demonstrated leadership
2013	Haessler Family Engineering Scholarship	\$5,000	Commitment to the engineering profession
2012	Education at Work Ontario - University Coop Student of the Year	\$500	University & employer nominated
2012	University of Guelph Coop Student of the Year, Science and Engineering	\$500	Employer nominated
2011	College of Physical and Engineering Sciences Dean's Scholarship	\$1,000	1 <sup>st</sup> year grades in top 13 of ~1,500
2010	University of Guelph Entrance Scholarship	\$3,000	Entrance average
2010	Waterloo-Wellington Science & Engineering Fair Entrance Scholarship	\$1,000	Performance at regional science fair

## PUBLICATIONS

### **PUBLISHED (2)**

Michael, J; Crook, J; Morton, D; Batchelar, D; Hilts, M; Fenster, A. (2017) "Reply to: Who Should Bear the Cost of Convenience? A Cost-effectiveness Analysis Comparing External Beam and Brachytherapy Radiotherapy Techniques for Early Stage Breast Cancer." *Clinical Oncology*, 29, 392-393. doi: 10.1016/j.clon.2017.03.003

Michael, J; Morton, D; Batchelar, D; Hilts, M; Fenster, A. (2017) "Intraoperative 3D ultrasound guidance system for permanent breast seed implantation." *Proceedings of SPIE Medical Imaging 2017*, 101351B. doi: 10.1117/12.2254461

### **SUBMITTED (2)**

Michael, J; Morton, D; Batchelar, D; Hilts, M; Crook, J; Fenster, A. (2017) "Development of a 3D Ultrasound Guidance System for Permanent Breast Seed Implantation." Manuscript submitted for publication.

Fenster, A; Rodgers, J; Michael, J; Gillies, D. (2017) "3D Ultrasound Guided Interventions." In: *Biomechanics of Soft Tissues: Principles and Applications*. Publisher: CRC Press/Taylor & Francis Group, LLC. Al-Mayah A. (ed.). Manuscript submitted for publication.

## PRESENTATIONS

### ORAL PRESENTATIONS

#### SPIE MEDICAL IMAGING (SUBMITTED) - HOUSTON, TX

Michael, J; Rodgers, J; Morton, D; Batchelar, D; Hilts, M; Fenster, A (Feb 2018)

3D ultrasound guidance system for permanent breast seed implantation: integrated system performance and phantom procedure (20 minutes)

#### CANADIAN ORGANIZATION OF MEDICAL PHYSICISTS (COMP) ANNUAL SCIENTIFIC MEETING - OTTAWA, ON

Michael, J; Morton, D; Batchelar, D; Hilts, M; Crook, J; Fenster, A (Jul 2017)

3D Ultrasound Image Guidance for Permanent Seed Breast Brachytherapy: System Development and Benchtop Validation (10 minutes)

#### SPIE MEDICAL IMAGING - ORLANDO, FL

Michael, J; Morton, D; Batchelar, D; Hilts, M; Fenster, A (Feb 2017)

Intraoperative 3D Ultrasound Guidance System for Permanent Breast Seed Implantation (20 minutes)

#### BIOMEDICAL ENGINEERING SEMINAR SERIES - LONDON, ON

Michael, J; Batchelar, D; Fenster, A (Nov 2016)

Development of a Three-Dimensional Ultrasound Scanner and Needle Template Localizing Arm for Guidance of Permanent Seed Breast Brachytherapy (15 minutes)

#### INNOVATIONS IN RADIATION ENGINEERED THERAPY - TORONTO, ON

Michael, J; Batchelar, D; Fenster, A (Nov 2016)

Developing a 3D Ultrasound Guidance System for Permanent Breast Seed Implantation (15 minutes)

#### LONDON IMAGING DISCOVERY DAY - LONDON, ON

Michael, J; Batchelar, D; Fenster, A (Jun 2016)

Development of a Three Dimensional Ultrasound Scanner and Template Localizing Arm for Guidance of Permanent Seed Breast Brachytherapy (10 minutes)

#### BIOMEDICAL ENGINEERING RESEARCH DAY - LONDON, ON

Michael, J; Batchelar, D; Fenster, A (Apr 2016)

Development & Validation of a Three Dimensional Ultrasound System for Guidance of Permanent Breast Seed Implantation in the Treatment of Breast Cancer (15 minute talk & poster)

**BIOMEDICAL ENGINEERING SEMINAR SERIES - LONDON, ON**

Michael, J; Batchelar, D; Fenster, A (Feb 2016)

Three-Dimensional Ultrasound Guidance of Low Dose Rate Brachytherapy for Breast Cancer (15 minutes)

**POSTER PRESENTATIONS**

**CANADIAN ORGANIZATION OF MEDICAL PHYSICISTS (COMP) ANNUAL SCIENTIFIC MEETING - OTTAWA, ON**

Morton, D; Michael, J; Batchelar, D; Hilts, M; Fenster, A; Crook, J; (Jul 2017)

The Value of 3D Ultrasound in Permanent Breast Seed Implant Brachytherapy

**ROBARTS RESEARCH RETREAT - LONDON, ON**

Michael, J; Morton, D; Batchelar, D; Hilts, M; Crook, J; Fenster, A (Jun 2017)

3D Ultrasound Image Guidance for Permanent Breast Brachytherapy: System Development and Benchtop Validation

**ONCOLOGY RESEARCH AND EDUCATION DAY - LONDON, ON**

Michael, J; Morton, D; Batchelar, D; Hilts, M; Crook, J; Fenster, A (Jun 2017)

3D Ultrasound Image Guidance for Permanent Breast Brachytherapy: System Development and Benchtop Validation

**LONDON HEALTH RESEARCH DAY - LONDON, ON**

Michael, J; Morton, D; Batchelar, D; Hilts, M; Fenster, A (Mar 2017)

A Guidance System for Permanent Seed Radiotherapy of the Breast Using 3D Ultrasound and Mechatronic Template Tracking

**ONTARIO INSTITUTE OF CANCER RESEARCH (OICR) SCIENTIFIC MEETING - TORONTO, ON**

Michael, J; Morton, D; Batchelar, D; Hilts, M; Fenster, A (Mar 2017)

Developing Intraoperative Image Guidance of Permanent Seed Breast Brachytherapy

**ANNUAL MEETING OF THE IMAGING NETWORK OF ONTARIO - TORONTO, ON**

Michael, J; Morton, D; Batchelar, D; Hilts, M; Fenster, A (Mar 2017)

3D Ultrasound and Mechatronic Template Tracking for Guidance of Permanent Seed Breast Brachytherapy



**ONCOLOGY RESEARCH AND EDUCATION DAY - LONDON, ON**

Michael, J; Batchelar, D; Fenster, A (Jun 2016)

A Mechanical 3D Ultrasound System for Intraoperative Guidance of Breast Brachytherapy

**ROBARTS RESEARCH RETREAT - LONDON, ON**

Michael, J; Batchelar, D; Fenster, A (Jun 2016)

A Mechanical 3D Ultrasound System for Intraoperative Guidance of Breast Brachytherapy

**ANNUAL MEETING OF THE IMAGING NETWORK OF ONTARIO - TORONTO, ON**

Michael, J; Batchelar, D; Fenster, A (Mar 2016)

Development of a Three Dimensional Ultrasound System for Guidance of Permanent Breast Seed Implantation

**LONDON HEALTH RESEARCH DAY - LONDON, ON**

Michael, J; Batchelar, D; Fenster, A (Mar 2016)

Developing Three Dimensional Ultrasound Guidance of Permanent Seed Brachytherapy for Breast Cancer

COMMUNITY INVOLVEMENT

**CONFERENCE CO-CHAIR** | ROBARTS RESEARCH INSTITUTE

October 2016 - June 2017 | London, ON

**COMMITTEE MEMBER** | ROBARTS ASSOCIATION OF TRAINEES

October 2016 - July 2017 | London, ON

**SESSION VOLUNTEER - LET'S TALK CANCER** | CANADIAN CANCER SOCIETY'S RESEARCH INFORMATION OUTREACH TEAM

May 2016 & May 2017 | London, ON

**MASTER OF CEREMONIES** | UNIVERSITY OF GUELPH ENGINEERING SOCIETY PROFESSIONAL DEVELOPMENT CONFERENCE

Jan 2015 | Guelph, ON

**CONFERENCE CHAIR** | ENGINEERING STUDENT SOCIETIES' COUNCIL OF ONTARIO PRESIDENT'S MEETING

Dec 2013 - Sep 2014 | Guelph, ON

**VICE-PRESIDENT EXTERNAL AFFAIRS** | UNIVERSITY OF GUELPH ENGINEERING SOCIETY

Apr 2013 - Apr 2014 | Guelph, ON

**ACADEMIC COMMUNITY BUILDER** | UNIVERSITY OF GUELPH

Sep 2012 – Sep 2013 | Guelph, ON

**“BIG BUDDY” (ENGINEERING ORIENTATION VOLUNTEER)** | UNIVERSITY OF GUELPH

Sep 2012 – Sep 2013 | Guelph, ON

**DIRECTOR – ESSCO CONNECTS** | ESSCO

Jun 2012 – Jun 2013 | Guelph, ON

**VARSITY ATHLETE** | UNIVERSITY OF GUELPH VARSITY ROWING TEAM

Sep 2010 – Dec 2012 | Guelph, ON

**CLASS REPRESENTATIVE** | UNIVERSITY OF GUELPH ENGINEERING SOCIETY

Sep 2010 – Apr 2012 | Guelph, ON